Quantitative mapping of elastic properties in nickel and titanium base alloys at nanoscale using atomic force acoustic microscopy

By

Makkuva Kalyan Phani

(ENGG 02 2010 04018)

Indira Gandhi Centre for Atomic Research, Kalpakkam

A thesis submitted to the

Board of Studies in Engineering Sciences

In partial fulfilment of requirements
for the Degree of

DOCTOR OF PHILOSOPHY

of

HOMI BHABHA NATIONAL INSTITUTE

August, 2015

HOMI BHABHA NATIONAL INSTITUTE

Recommendations of the Viva Voce Committee

As members of the Viva Voce Committee, we certify that we have read the dissertation prepared by **Makkuva Kalyan Phani** entitled "**Quantitative mapping of elastic properties in nickel and titanium base alloys at nanoscale using atomic force acoustic microscopy**" and recommend that it may be accepted as fulfilling the thesis requirement for the award of Degree of Doctor of Philosophy.

Date: 05 May 2016

Chairman: **Prof. T. Jayakumar**

Date: 5/5/16

Guide/Convener: **Dr. Anish Kumar**

Date: 5/5/2016

Member 1: **Dr. B. Purnachandra Rao**

Date: 05/05/2016

Member 2: **Dr. A. K. Tyagi**

Date: 5/5

Examiner: **Prof. N.N. Kishore**

Final approval and acceptance of this dissertation is contingent upon the candidate's submission of the final copies of the dissertation to HBNI.

Date:

Place: Kalpakkam

CERTIFICATE

I hereby certify that I have read this thesis prepared under my direction and recommend that it may be accepted as fulfilling the thesis requirement.

Date: 5/5/16

Place: Kalpakkam

(ANISH KUMAR)

STATEMENT BY AUTHOR

This dissertation has been submitted in partial fulfilment of requirements for an advanced degree at Homi Bhabha National Institute (HBNI) and is deposited in the Library to be made available to borrowers under rules of the HBNI.

Brief quotations from this dissertation are allowable without special permission, provided that accurate acknowledgement of source is made. Requests for permission for extended quotation from or reproduction of this manuscript in whole or in part may be granted by the competent authority of HBNI when in his or her judgment the proposed use of the material is in the interests of scholarship. In all other instances, however, permission must be obtained from the author.

(M. KALYAN PHANI)

DECLARATION

I, hereby declare that the investigation presented in the thesis has been carried out by me. The work is original and has not been submitted earlier as a whole or in part for a degree / diploma at this or any other Institution / University.

(M. KALYAN PHANI)

`

List of Publications

Referred Journals (5)

1. **M. Kalyan Phani**, Anish Kumar and T. Jayakumar, "Elasticity mapping of delta precipitate in alloy 625 using atomic force acoustic microscopy with a new approach to eliminate the influence of tip condition", Philosophical Magazine Letters, **2014**, 94, 395 - 403.

2. **M. Kalyan Phani**, Anish Kumar, T. Jayakumar, Walter Arnold and Konrad Samwer, "Mapping of elasticity and damping in an α + β titanium alloy using atomic force acoustic microscopy", Beilstein Journal of Nanotechnology, **2015**, 6, 767–776.

3. **M. Kalyan Phani**, Anish Kumar, W. Arnold, and K. Samwer, "Elastic stiffness and damping measurements in titanium alloys using atomic force acoustic microscopy", Journal of Alloys and Compounds, **2016**, 676, 397-406.

4. **M. Kalyan Phani**, Anish Kumar and Vani Shankar, " Elasticity mapping of precipitates in nickel base superalloys using atomic force acoustic microscopy", Journal of Material Science **(Under review)**

5. Anish Kumar, **M. Kalyan Phani**, M. Büchsenschütz-Göbeler, W. Arnold, and K. Samwer, "Damping measurements using atomic force acoustic microscopy" **(Under preparation)**

International Conferences (3)

1. **M. Kalyan Phani**, Anish Kumar, T. Jayakumar, M. Büchsenschütz-Göbeler, Y. Luo,Walter Arnold and Konrad Samwer, "Mapping of elasticity and damping in an α + β titanium alloy using atomic force acoustic microscopy", presented at **5th International workshop on Advanced Scanning Probe Microscopy Techniques (ASXMT)** held at Karlsruhe Institute of Technology, Karlsruhe, **Germany**, February **2014**.

2. **M. Kalyan Phani** and Anish Kumar, "Elasticity mapping of precipitates present in CM247A aeronautical grade superalloy using atomic force acoustic microscopy", presented at **2nd International Conference on Advances in Steel, Power and Construction Technology**" held at OP Jindal University, Raigarh, **India**, March **2016**.

3. **M. Kalyan Phani,** Anish Kumar, W. Arnold, Konrad Samwer, 'Elastic stiffness and damping measurements in metals using atomic force acoustic microscopy", IEEE International Ultrasonics Symposium to be held at VINCI Convention Center, Tours, **France**, September **2016** (Communicated)

National Conferences (2)

1. **M. Kalyan Phani**, Anish Kumar and T. Jayakumar, "Elasticity mapping of sub-micron size precipitates in Inconel 625 using Atomic Force Acoustic Microscopy" presented at **50th National Metallurgists Day – Annual Technical Meet (NMD-ATM)** held at Jamshedpur, India, November **2012**.

2. Anish Kumar, **M Kalyan Phani**, S. Sosamma, B.P.C. Rao and T. Jayakumar, "Multi-scale microstructural characterization through acoustic measurements", presented at **Acoustics** held at New Delhi, India, November **2013**.

"If you want to find the secrets of the universe, think in terms of energy, frequency and vibration…"

-Nikola Tesla

Dedicated

To

My Family

$$\left\{\begin{array}{c} \boldsymbol{M.Lalitha\ Devi\ (Mom)} \\ \boldsymbol{M.Kailasa\ Rao\ (Dad)} \\ \boldsymbol{M.L.N.Sri\ Harsha\ (Brother)} \end{array}\right\}$$

`

Acknowledgements

First, I want to thank, the great almighty God, for giving me this life with such great accomplishments. I would owe to him for the rest of my lives.

I would like to express my deep sense of gratitude to my research supervisor and mentor Dr. Anish Kumar, Head, Ultrasonic Measurements Section, Non-Destructive Evaluation Division (NDED), Metallurgy and Materials Group (MMG) , Indira Gandhi Centre for Atomic Research (IGCAR) for his consistent guidance, patience, encouragement and support that led to the successful completion of this thesis work.

I express my sincere gratitude to Dr. T. Jayakumar, former Director, MMG, IGCAR and Chairman of my doctoral committee, for his inspiration, encouragement and most importantly providing direction during the course of thesis work. I thank eminent members of the doctoral committee Dr. B.P.C. Rao and Dr. A. K. Tyagi for their regular appraisal, kind advice and suggestions to improve the quality of this work. I would like to extend my heartfelt thanks to the former directors of IGCAR, Dr. Baldev Raj, Shri S. C. Chetal and Dr. P. R. Vasudeva Rao and the present Director Dr. S. A. V. Satyamurthy for permitting me to pursue research in this reputed centre. I am grateful to Dr. M. Saibaba for the wonderful hospitality during my stay at kalpakkam.

I would like to take opportunity to thank Prof. Dr. Walter Arnold for all the kind help and suggestions provided to me at IGCAR and also during my stay at Physikalisches Institut-I, Georg-August-Universität, Göttingen, Germany. I would also like to thank to all the colleagues at the university, Prof. Dr. J. A. Turner (now at University of Nebraska-Lincoln, U.S.A), Mr. M. Büchsenschütz-Göbeler and Prof. Dr. Konrad Samwer for their kind hospitality, valuable suggestions and fruitful discussions during my stay at Göttingen, Germany.

I would like to express my whole-hearted thanks to Dr. K. V. Rajkumar, Dr. G. K. Sharma, Shri Mahadevan, Dr. S. Thirunavkararasu, Smt. Sosamma and Smt. Sasi for their encouragement. Thanks to my fellow colleagues, Shri G. V. K. Kishore, Shri A. Viswanath, Shri R. Manoj Kumar, Shri M. M. Narayanan, Shri A. Ravigopal, Shri G. M. S. K. Chaitanya, Shri Ponseenivsan and Shri J. Abuthahir for their constant support and encouragement. Sincere thanks to Shri P. Sukumar for helping me during sample preparation. Special thanks to Smt. Vani Shankar for the SEM and EBSD measurements and also fruitful discussions.

I would like to thank my friends, Dr. S. Anbumozhi, Shri K. Benadict Rakesh, Shri G. Prasanna, Shri K. B. R. R. Hari, Shri K. Samba Siva Rao, Shri V. Arjun, Shri Anil Kumar Soni and Dr. Shuaib Ahmed, for all the wonderful fun time and mental support during my stay at Kalpakkam. I would also thank other friends and juniors in IGCAR and JRF enclave for making my stay memorable.

Finally, this work would not have been possible but for the love, sacrifice, patience and support of my beloved parents. My deepest sincere thanks to my lovable brother, Mr. M. L. N. Sri Harsha for helping and encouraging me throughout.

(M. KALYAN PHANI)

`

TABLE OF CONTENTS

ABSTRACT

Atomic force acoustic microscopy (AFAM) was used for mapping the elastic modulus of various phases/precipitates present in two main classes of multiphase structural alloys viz. nickel and titanium alloys, at nanoscale. The microstructure of the multiphase alloys were characterized by X-ray diffraction (XRD), scanning electron microscopy (SEM), electron back scatter diffraction (EBSD) and Atomic force microscopy (AFM) studies. Specific software were developed to acquire and analyze the data obtained by AFAM system.

In nickel base superalloys, a polycrystalline superalloy, alloy 625 and a directionally solidified superalloy, CM 247A were taken for study. A new methodology was developed to circumvent the problem of change in tip radius by implementing simultaneous acquisition of two contact resonance frequencies and by using matrix as a reference. Cantilever dynamics model neglecting damping was used to derive the contact stiffness (k^*) and indentation modulus (M). Experimental M values of γ′, δ and carbides present in the two nickel base superalloys were reported for the first time.

Simultaneous mapping of stiffness and damping was carried out in two types of titanium base alloys. Ti-6Al-4V, an α+β titanium alloy and Ti-10V-4.5Fe-1.5Al, a β titanium alloy were taken for study. Specimens of titanium alloys were subjected to heat treatment at different temperatures. Cantilever dynamics model considering damping was used to derive the M and damping (E''/E'). The experimental M and E''/E' values of α, β and α' phases present in the two titanium alloys were reported for the first time.

Effect of heat treatment temperature and duration on the elastic and damping properties was studied. The elastic and damping properties at nanoscale are compared with those for bulk samples by ultrasonic measurements. The study demonstrated that the nanoscale elastic properties measured using AFAM can also be used for obtaining the average elastic properties of the bulk samples with an accuracy of ~5 %. The systematic error in the elastic property measurements using single reference has also been brought out.

Attempts were made to understand the effect of crystallographic orientation on AFAM measurements. It was demonstrated that, due to the close packed orientation relationships of precipitates with the matrix, the modulus of a precipitate measured by the methodology described in the present thesis was not affected to a large extent by the orientation of individual grain in which the measurement was made. The study also clearly demonstrates that, AFAM can be used to disclose relative elastic property of materials with high spatial resolutions, even for materials with a slight difference in elastic properties (~4 %).

LIST OF FIGURES

LIST OF TABLES

NOMENCLATURE

SYMBOLS

A	Area
a_c	Contact radius
a_n	Real part
B	Bulk modulus
b_n	Imaginary part
C_c	Material constant
c_p	Ratio normal and lateral contact stiffness
d	Tip-sample distance
E	Elastic modulus
E'	Storage modulus
E''	Loss modulus
E^*	Reduced elastic modulus
$E_{S,\,Tip}$	Young's modulus of sample or tip
f	Frequency
F_{ad}	Adhesion force
F_c	Applied Force
f_{cR}	Contact resonance frequency
f_{ff}	Free resonance frequency
F_{ts}	Tip sample force
G	Shear modulus
h	Height of the tip
H	Hamaker constant
H_c	Coercivity
I	Moment of inertia
k^*	Contact stiffness
k^*_{lat}	Lateral contact stiffness
k_c	Spring constant
k_i	Imaginary part of contact stiffness
k_n	Wave number

k_nL	Dimensionless wavenumber
k_r	Real part of contact stiffness
L	Length
L_1/L	Tip position
$M_{iso,\ aniso}$	Isotropic or anisotropic indentation modulus
$M_{S,\ Tip}$	Sample or tip indentation modulus
nc	Nanocrystalline
P	Applied load
P_{ts}	Potential energy between tip and sample
Q	Quality factor
$Q^{-1}{}_{loc}$	Local contact damping
R	Radius of curvature
T_m	Melting point
U	Interatomic potential
U_{bias}	Bias voltage
U_{cpd}	Contact potential difference
V_L	Longitudinal wave velocity
V_r	Rayleigh wave velocity
V_T	Transverse wave velocity
y_0	Vibration amplitude
z	distance between the plane connecting the centers of surface atoms and center of the closet tip atom
Z	Acoustic Impedance
Z_{ts}	Distance between sample surface and rest position cantilever
γ	Interactive damping
δ_c	Cantilever deflection
δ_s	Sample deformation
ε	Interaction strength
η_{air}	Air damping
η_n	Normalized damping constant
θ	Cantilever angle
λ_n	Normalized contact stiffness

v	Poisson's ratio
$v_{s,tip}$	Poisson's ratio of sample or tip
ρ	Density
σ	Distance between the two particles at equilibrium
ω	Angular frequency

UNITS

Å	Angstroms
eV	Electron volt
GHz	Giga Hertz
GPa	Giga Pascal
K	Kelvin
kHz	Kilo Hertz
MHz	Mega Hertz
ms	milli second
mW	milli Watt
N/m	Newton per meter
nm	Nanometer
nN	Nano newton
Pa	Pascal
Wt	Weight
μm	Micrometer
μN	Micronewton

ABBREVIATIONS

AFAM	Atomic force acoustic microscopy
AFM	Atomic force microscopy
$BaTiO_3$	Barium titanate
BCC	Body centered cubic
BE	Band excitation
BR	Burger's relationship
BTT	Beta transus temperature
CAFM	Conductive AFM
CDM	Cantilever dynamics model
CFM	Chemical force microscopy

CFRP	Carbon fiber reinforced plastic
CMM	Contact mechanics model
COS	Carpick, Ogletree and Salmeron
CR	Contact resonance
CR-AFM	Contact-resonance AFM
CRF	Contact resonance frequency
CRS	Contact resonance spectra
DART	Dual AC resonance tracking
DMT	Derjaguin-Muller-Toporov
DS	Directional solidification
EBSD	Electron back scatter diffraction
EDX	Energy dispersive x-ray analysis
EFM	Electrostatic force microscopy
FD	Force-distance
FEG	Field emission gun
FEM	Finite element method
FMM	Force modulation microscopy
FSG	Fluorosilicate glass
GFRP	Glass fiber reinforced plastic
GGA	Generalized gradient approximation
HCP	Hexagonal closed packed
IC-AFM	Intermittent contact AFM
JKR	Johnson-Kendall-Roberts
KPFM	Kelvin probe force microscopy
LabVIEW	Laboratory Virtual Instrument Engineering Workbench
LAFM	Liquid-AFM
LCB	Low cost beta
LCR	Lorentz contact resonance
LDA	Liner density approximation
MExFM	Magnetic exchange force microscopy
MFM	Magnetic force microscopy
MRFM	Magnetic resonance force microscopy
NC-AFM	Non-contact AFM
NI	Nanoindentation

OM	Optical microscopy
OR	Orientation relationship
PDM	Phase detection microscopy
PFM	Piezo response force microscopy
PIC	Piezoelectric ceramic
PMMA	Polymethylmethacrylate
PP	Polypropylene
PS	Polystyrene
PTC	Lead calcium titanate
PZT	Lead-Zirconate-Titanate
RUM	Resonance ultrasound microscopy
SAFM	Scanning acoustic force microscopy
SAM	Scanning acoustic microscopy
SEM	Scanning electron microscopy
SP	Setpoint
SPM	Scanning probe microscopy
SVM	Scanning voltage microscopy / Nanopotentiometry
SX	Single crystal
TEM	Transmission electron microscopy
TMAFM	Tapping mode AFM
UAFM	Ultrasonic atomic force microscopy
UFM	Ultrasonic force microscopy
UPFM	Ultrasonic piezoelectric force microscopy
VB	Visual basic
XRD	X-ray diffraction

1 INTRODUCTION

1.1. BACKGROUND CONTEXT

Multiphase structural alloys are alloys with more than one microstructural constituents (phase/precipitate). They are designed to work in harsh environments like in high stress, high temperature and corrosive environments. During this, materials experience a lot of microstructural changes which may soften the alloy and finally lead to catastrophe. Mechanical properties of these alloys are governed by their microstructural constituents (individual phases/precipitates). With the knowledge of the properties of the individual phases/precipitates, one can study and understand, the stress distribution at a micro scale, the deformation behavior, the crack nucleation, dislocation activity and interaction with grain boundaries and the crack propagation and thus the response of the multiphase materials against external load/strain. This in-turn plays an important role in the development of materials with enhanced properties based on mechanistic understanding. Elastic strains arising from mismatch between the modulus of matrix and precipitates can also alter the deformation mechanism of a material. In the presence of a precipitate, the material can be considered as a composite of three components, i.e. matrix, matrix-precipitate interface and precipitate [1]. With variation in the strength of these precipitates/phases, the bulk property of the material can fluctuate. Precipitates can be detrimental or beneficial. Amount and size of the precipitates and phases are also important as they influence the mechanical properties. The principal aspect of this thesis is to experimentally measure the elastic properties of various phases/precipitates present in multiphase structural alloys using atomic force acoustic microscopy (AFAM).

The dissipation of absorbed elastic/mechanical energy into heat is characterized by the damping properties of the material. The vibration related problems can be eliminated by either increasing the stiffness of the structure or increasing the damping in the alloy. In metals and alloys, however, exhibiting simultaneously high damping capacity and good mechanical properties has been noted to be normally incompatible. Because the microscopic mechanisms responsible for internal friction (namely damping capacity) are dependent upon parameters that control mechanical strength [2]. Dual phase materials could be the only solution because it can be tailored to have one phase which takes care of the mechanical strength and other optimizes the damping property.

There are various ways to calculate the elastic properties of samples at different scales, as shown in Figure 1.1. Static methods like tension, bending and torsion testing and dynamic methods like resonance frequency methods have been used for measurement of elastic properties of bulk samples. Wave propagation methods like ultrasonic pulse echo techniques have also been successfully used to calculate the bulk elastic properties of the materials. None of the above techniques give direct measurements of the elastic properties of individual phases/precipitates in the matrix of multiphase structural alloys. Ultrasonic based methods involving ultra-high frequencies (GHz) [3] have acquired interest in calculating the elastic properties of materials with resolution limited to a few tens of micron. In a scanning acoustic microscopy (SAM), a transducer produces, transmits and receives short sound pulses of about a GHz frequency. Sound field is focused on the sample through the coupling medium (water/inert liquid). V(z)-Scans measure acoustic reflection intensities as a function of the lens position from the sample surface along the z-axis, using which the ultrasonic velocities on the surface of the material are calculated. However, SAM suffers from poor resolution (~20 microns) [4]. One potential technique which has proven itself successful in calculating the elastic properties locally at scales below microns is the nanoindentation method [5]. However, this technique suffers with the deep indentation created by the nano indenter which would leave the sample with a crater making the sample useless for further

studies. Further, the lateral resolutions of nanoindentation is usually limited to a few hundreds of nm. Resonance ultrasound microscopy (RUM), a contact resonance based technique was developed by Ogi et al. [6] to study the local stiffness and local internal friction in materials with improved lateral resolutions up to 200 nm [7]. RUM uses an isolated langasite oscillator to which a mono crystal diamond tip is attached at the very end. Longitudinal vibrations are excited and detected by a line antenna which is placed near the oscillator. Independent of surface roughness of the sample, the biasing force at the contact is kept constant so that the change in resonance frequency can be sensed due to the change in elastic property in the material. But until recently, there was no technique which could image mechanical properties of the individual phases/precipitates and provide quantitative distribution map of the mechanical property data for the individual microstructural constituents. Finally, the emergence of AFAM made it possible to probe the materials elastic properties to the scales previously not possible.

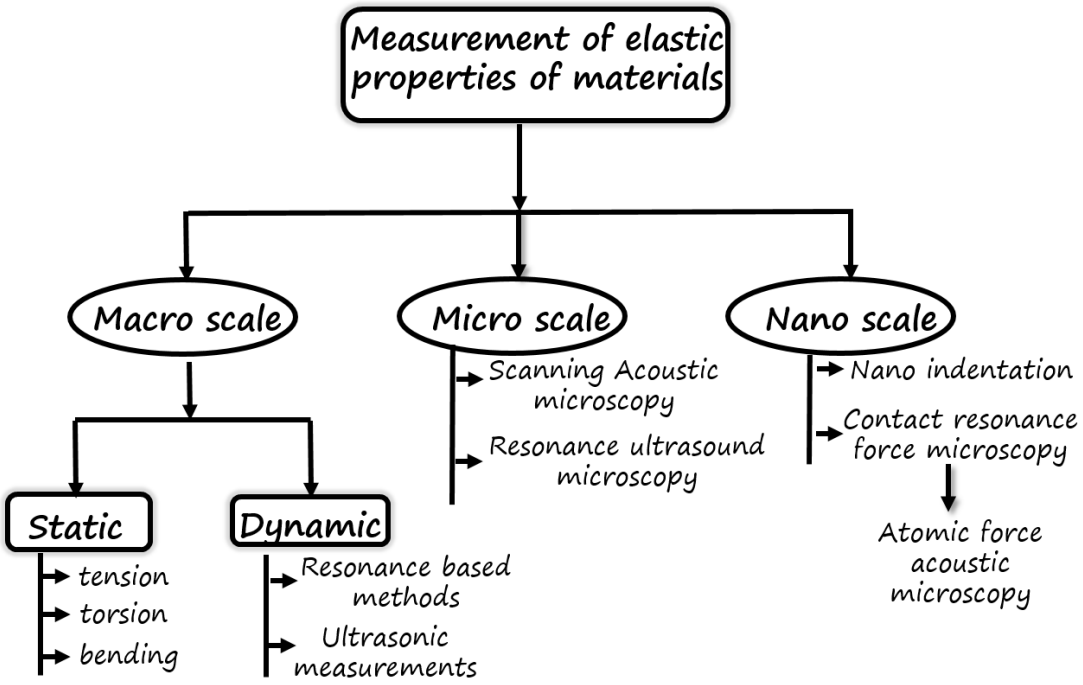

Figure 1.1: Measurement of elastic properties of materials at various dimensions

Many techniques like Optical microscopy (OM), Scanning electron microscopy (SEM) and Transmission electron microscopy (TEM) have proved their versatility for microstructural characterization of materials with good resolution limits.

AFAM being a surface probe technique is equally comparable with the available advanced microscopy techniques. Figure 1.2 shows the comparison between the AFAM technique and other microscopy techniques. AFAM has resolution limit as low as few tens of nm. This limit comes with the sharpness of the tip used. The sharper the tip, better the resolution of the obtained image.

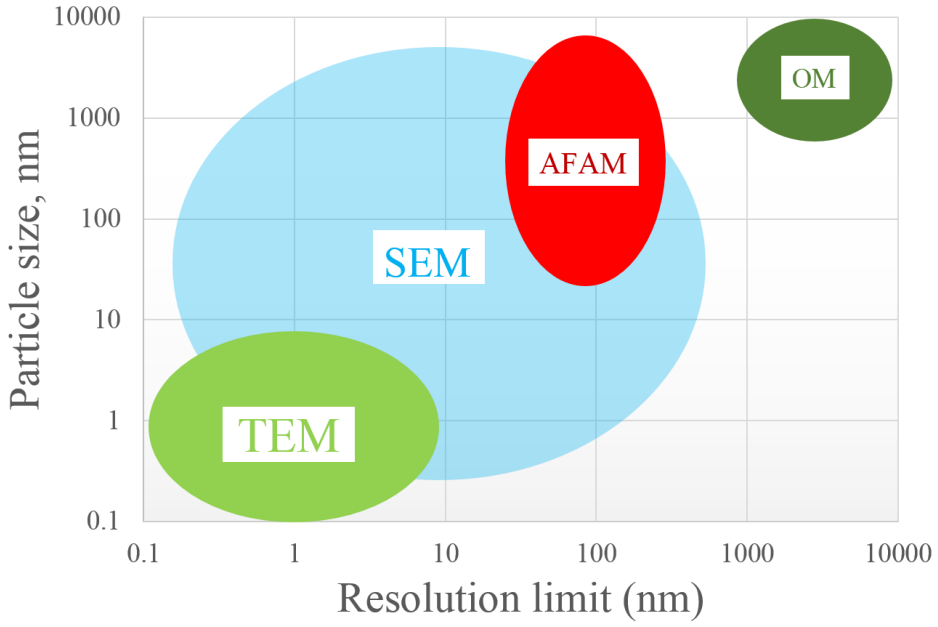

Figure 1.2: Comparison between different microscopy techniques

AFAM is one of the emerging techniques in the field of advanced scanning probe microscopy techniques. AFAM is a dynamic atomic force microscopy technique which come under the category of contact resonance atomic force microscopy (CR-AFM) techniques. In AFAM, a piezoelectric transducer is placed under a sample and longitudinal vibrations are guided through the sample. These vibrations from the sample surface are sensed by a cantilever, when in contact. A laser is dually focused on the end of the cantilever and on a 4-sectioned photo-diode. The

amplitude of this cantilever's vibrations at various excitation frequencies, i.e. contact resonance (CR) spectra, are detected by the AFM photodiode's signal by use of a lock-in-amplifier. The CR spectra obtained contains three kinds of information: shift in peak frequencies of the CR curves, decrease or increase in the amplitude and the width of the CR curves. Elastic property variations can be studied using resonance frequency shift [8] and damping variations using decrease or increase in amplitude and width (quality factor, Q) [9, 10]. The peak frequency in the CR spectrum, i.e. CR frequencies (CRFs) are converted to modulus values by using suitable cantilever dynamics model (CDM) and contact mechanics model (CMM) [8, 11, 12]. The CDM, explains the dynamic behavior of the cantilever and is used to calculate the contact stiffness by measuring contact resonances of any two modes. The CMM derives the reduced elastic modulus of the sample from the calculated contact stiffness, using the forces between the tip and the sample, and the contact radius [12]. In the past two decades, AFAM has been extensively used to study elastic properties in amorphous materials [13], polycrystalline materials [11, 14-16], single crystals [17], polymers [18], plants [19], clay minerals [20] and composites [21] . Extensive work has also been progressed well towards local damping measurements in polymers [9], polycrystalline materials, amorphous materials [22, 23] and nano-crystalline materials [22, 24] using AFAM by considering point mass [22, 24] and distributed mass [16, 23, 25] models to describe the cantilever motion.

Primary aim of this thesis work is to utilize AFAM for studying the elastic and damping properties of various phases in multiphase alloy systems. Attempts are made to understand the difference in the properties of precipitates present in the alloy subjected to heat treatment at different temperature and durations. The nanoscale elastic properties measured using AFAM can be used for obtaining the average elastic properties of the bulk samples with good accuracy. Correlation studies were carried out with the elastic properties of bulk specimens measured by ultrasonic velocity measurements and AFAM. The influence of relative modulus of the reference sample and

the sample to study on the error in the modulus measurement is discussed. The influence of grain orientation on AFAM measurements has also been explored.

3.2. STRUCTURE OF THE THESIS

Chapter 1 discusses the background context for the work carried out in this thesis. A brief explanation is given for the importance of knowledge of the modulus and damping of the individual precipitates/phases present in multiphase structural materials. Attempts to study the elastic properties of the materials at different scales with various methods and their limitations have been provided.

Chapter 2 deals with the literature review and provides insights on importance of knowledge of elastic properties at nanoscales. Elastic property measurements at various dimensions have been discussed. Various AFM techniques developed in studying the elastic properties in the past few years have been discussed. CR-AFM is the name given for techniques which rely on contact resonances. An introduction of these techniques has been provided. The physical principles of AFM and AFAM techniques are discussed in more detail. Literature review on the modulus and damping measurements performed by various groups using AFAM has been summarized. Metallurgy of the various materials studied in this thesis have also been discussed. Finally, motivation and objective of this thesis are deliberated.

Chapter 3 discusses the detailed experimental setup of AFAM used in the present study. Various softwares developed for acquisition and analysis of the contact resonance frequency data have been discoursed. Various cantilevers used for the study are provided. Sample preparation methods used in this thesis have also been discoursed.

Chapter 4 discusses the effect of various parameters (such as load, frequency, spring constant, angle, radius, CDM and cantilever tip) on AFAM measurements. With this, one can eliminate the erroneous values and offer much better quantitative values for the indentation modulus.

Chapter 5 discusses elasticity mapping of precipitates present in a polycrystalline nickel base superalloy and a directionally solidified nickel base superalloy. A new approach to circumvent the problem of tip wear during mapping of elastic property using AFAM has been discussed. The experimental values for the indentation modulus of various precipitates present in nickel-base superalloys are reported for the first time. It is demonstrated that, due to the close packed orientation relationships of precipitates with the matrix, the modulus of a precipitate measured by the methodology described in this study is not affected to a large extent by the orientation of individual grain in which the measurement is made.

Chapter 6 discusses simultaneous mapping of stiffness and damping properties of various phases present in an (α+β) and a β – titanium alloy using AFAM. The obtained elasticity and damping data for the individual phases was compared for the two alloys and also correlated with the those obtained using the ultrasonic velocity and attenuation measurements on bulk titanium alloy samples. The calculated values for the individual phases using AFAM for the bulk sample was in agreement with the ultrasonic velocity measurements on bulk samples and the variation in the values were found to be below 5% for most of the samples. The systematic error in the elastic property measurements using single reference has also been discussed. The effect of crystallographic orientation on the AFAM measurements has been discussed.

Chapter 7 summarizes the results obtained, conclusions drawn and the scope for future work.

2 LITERATURE REVIEW

2.1. INTRODUCTION

This chapter deals with the state of the art of measurement of elastic properties of materials and the importance of the knowledge of the elastic properties of individual phases/precipitates at the nanoscale. Measurement of elastic properties at various dimensions with various instruments have been discussed. Brief introduction of atomic force microscopy (AFM) and its advances in the last two decades have been presented. Introduction to AFAM, the theoretical aspects of AFAM and its emergence as an advanced scanning probe microscopy in the past two decades have been focused. The last section deals with the physical metallurgy of the materials studied in the thesis. Finally, motivation and objective of the thesis is presented.

2.2. ELASTIC PROPERTY MEASUREMENTS AT VARIOUS DIMENSIONS

Pure metals are very soft. They are often alloyed with other elements and subjected to suitable thermo-mechanical treatments to enhance their strengths for application as structural materials. Most of the structural alloys comprise of more than one phase. The size, coherence and distribution of the secondary phases govern the mechanical behavior of these multiphase alloys. The knowledge of elastic properties of the individual phases is important for studying their deformation behavior, crack nucleation and propagation, dislocation activity and interaction with grain boundaries and also helps in understanding the bulk elastic properties of multiphase materials.

Elastic properties of materials have been studied by various methods. Elastic properties can be measured nondestructively at macro, micro and nano scales with good accuracies. The following sub-sections give brief information about various techniques used for measuring elastic properties at macro, micro and nano dimensions.

2.2.1. Measurement of elastic properties at macro scale

Elastic properties can be measured by static or dynamic methods. Static methods are based on the measurement of the deformation induced in materials by application of a known force. Dynamic methods are based on studying the resonance behavior of the sample or measuring the ultrasonic wave velocities in the material [26]. Of all the methods, ultrasonics is considered as the most accurate method for measuring elastic properties of bulk materials, that too non-destructively [27]. Only the acoustic base methods have achieved reproducibility of better than 10^{-6} in measuring the bulk elastic properties [28]. Many studies are reported on measurement of elastic properties using ultrasonic measurements for evaluation of stiffness (ultrasonic velocities) and damping (ultrasonic absorption) in various materials [29]. Different elastic moduli can be determined from ultrasonic longitudinal and shear wave velocities, and the density of a material. The following equations are generally used for evaluation of elastic properties based on ultrasonic velocity measurements [29]:

$$G = \rho V_T^2 \tag{2.1}$$

$$B = \rho \left[V_L^2 - \frac{4}{3} V_T^2 \right] \tag{2.2}$$

$$E = \frac{3\rho V_T^2 \left[V_L^2 - \frac{4}{3} V_T^2 \right]}{\left(V_L^2 - V_T^2 \right)} \tag{2.3}$$

and $$\nu = \frac{V_L^2 - 2V_T^2}{2(V_L^2 - V_T^2)} \tag{2.4}$$

where, *G, B, E, ν, V_L* and *V_T* are shear modulus, bulk modulus, Young's modulus, Poisson's ratio, ultrasonic longitudinal wave velocity and ultrasonic shear wave velocity, respectively. These equations form the basis for microstructural characterization using ultrasonic velocity measurements. These are frequently used equations to determine the elastic properties at macro scale.

2.2.2. Measurement of elastic properties at micro scale

A near field technique called scanning acoustic microscopy (SAM) [3], which uses about a GHz frequency transducer can be used to study elastic properties at micron scales. The transducer produces, transmits and receives short sound pulses. Sound field is focused on the sample through the coupling medium (water/inert liquid). V(z)-scans measure acoustic reflection intensities as a function of the lens position from the sample surface along the z-axis. Intensity versus z-axis position results in V(z) curve (Figure 2.1), using which the ultrasonic velocities on the surface of the material are calculated employing equation (2.5). However, SAM suffers from poor resolution (~20 microns) [4].

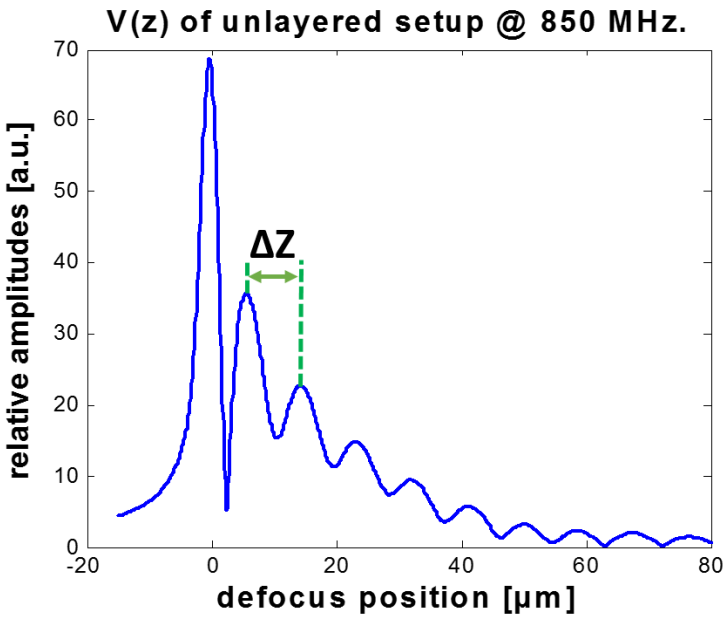

Figure 2.1: V(z) signature for Glass obtained by scanning acoustic microscopy (SAM)

$$V_r = \frac{V_0}{\sqrt{1-(1-\frac{V_0}{2f\Delta z})^2}} \tag{2.5}$$

Where, V_r = rayleigh wave velocity on the surface of the test material, V_0 = wave velocity in the coupling fluid, f = signal frequency and Δz – spacing between successive peaks or dips in the V(z) curve as shown in Figure 2.1..

Resonance ultrasound microscopy (RUM), a contact resonance based technique, was developed by Ogi et al. [6, 30] to study the local stiffness and local internal friction in materials with improved lateral resolutions up to 200 nm [7]. RUM uses an isolated langasite oscillator to which a mono crystal diamond tip is attached at the very end. Longitudinal vibrations are excited and detected by a line antenna which is placed near the oscillator. Independent of surface roughness of the sample, the biasing force at the contact is kept constant so that the change in resonance frequency can be sensed due to the change in elastic property in the material.

2.2.3. Measurement of elastic properties at nano scale

In the previous sections, the emergence of various techniques to study the elastic properties in a material with resolutions upto few microns have been presented. Scanning probe microscopies (SPMs) have changed the way we see materials. Scanning probe microscopy is a branch of microscopy that produces images using a physical probe that scans the sample. Atomic force microscopy (AFM) is a part of SPM which has emerged as the best tool for topographical studies upto atomic scales [31]. The lateral resolution of the AFM is governed by the tip radius which is of the order of a few nanometers to tens of nanometers. The very high lateral resolution available with AFM has led to the development of AFM based techniques for measurement of elastic properties at nanoscales. The AFM and their advanced techniques used to study elastic properties at nanoscale are discussed in the following sections.

2.3. ATOMIC FORCE MICROSCOPY

AFM is similar to scanning tunneling microscope (STM) except that the tunneling tip in STM is replaced by a force sensor [32]. AFM operates by measuring forces present between a probe and the sample. Though the lateral resolution of AFM is low (~30 nm) due to the convolution, the vertical resolution can be up to 0.1 nm and this resolution comes from the tip radius mentioned in previous sections of the thesis.

AFM measures the vertical and lateral deflections of the cantilever by using an optical lever. The optical lever operates by reflecting a laser beam off the cantilever. The reflected laser beam strikes a four-segment position sensitive photo-detector. The differences between the signals of the segments of photo-detector indicate the position of the laser spot on the detector and thus the angular deflections of the cantilever. Piezo-ceramics position the tip with high resolution. Piezo ceramics are a class of materials that expand or contract on the application of voltage gradient. Piezo-ceramics make it possible to create three-dimensional positioning devices of very high precision.

In contact mode, AFM uses feedback to regulate the force on the sample. The AFM not only measures the force on the sample but also regulates it, allowing acquisition of images at very low forces. The feedback loop consists of a tube scanner that controls the height of the tip, a cantilever and the optical lever, which measures the local height of the sample; and a feedback circuit that attempts to keep the cantilever deflection constant by adjusting the voltage applied to the scanner. A well-constructed feedback loop is essential to microscope performance.

There are two principal modes of operation of AFM: the static and the dynamic mode. In the static mode, the cantilever is scanned relative to the sample while in contact or in non-contact (e.g. several tens of nm above the surface). Attractive/repulsive tip-sample forces bend the

cantilever towards/away from the sample. According to Hooke's law, the magnitude of the tip-sample force is proportional to the cantilever’s deflection.

In the dynamic mode, the cantilever is oscillated at or near by its resonance frequency. Depending on the way of excitation, the cantilever is externally driven or self-oscillating. Any tip-sample interaction influences amplitude, phase or frequency of the cantilever. During oscillation, the tip may (*tapping*) or may not (*non-contact*) touch the surface at the lower turnaround point. It is not as straightforward as in the static mode to quantify the magnitude of the tip-sample interaction. In the case of long-range interactions, the frequency shift is proportional to the force gradient. Song et al. [33] have classified various static and dynamic modes in AFM, they are shown in Table 2.1.

Table 2.1: Various modes in AFM [33]

Static modes						
Mode	Cantilever deflection			Output	Detected surface properties	
Contact mode	Vertical bending			Normal deflection	Topography, adhesion	
Friction force microscopy	Vertical bending, torsion and lateral bending			Normal deflection and twist angle	Topography, friction	
Dynamic modes						
Mode	Schematics	Cantilever deflection	Excitation source	Driving frequency	Output	Detected surface properties
Tapping mode, non-contact AFM	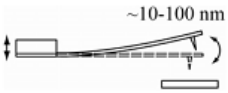	Vertical bending	Holder	Fundamental flexural resonance frequency	Normal deflection amplitude, phase and frequency shift	Topography and normal viscosity
Force modulation mode, atomic force acoustic microscopy mode		Vertical bending	Sample surface or holder	Fundamental and higher order flexural resonance frequency	Normal deflection amplitude and resonance frequency	Normal stiffne
Torsional resonance mode	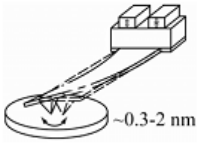	Torsion and lateral bending	Holder	Torsional resonance frequency	Torsional amplitude, phase and resonance frequency	Topography, lateral stiffness and viscosity
Lateral excitation mode	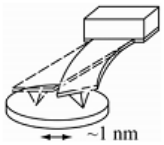	Torsion and lateral bending	Sample surface	In a wide range, from very low (~20 kHz) to very high (up to 3 MHz)	Torsional amplitude, phase and resonance frequency	Topography, friction, lateral stiffnes and viscosity
Combined normal and lateral excitation mode	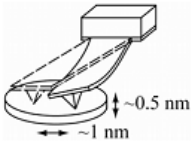	Vertical bending, torsion and lateral bending	Sample surface	In vertical direction higher than first flexural resonance frequency; in lateral direction much lower than torsional resonance frequency	Normal deflection amplitude and phase, torsional amplitude, phase and resonance frequency	Normal stiffne and lateral stiffness

Various methods in AFM:

Figure 2.2 shows various methods in AFM with which a handful of different properties in the material can be measured:

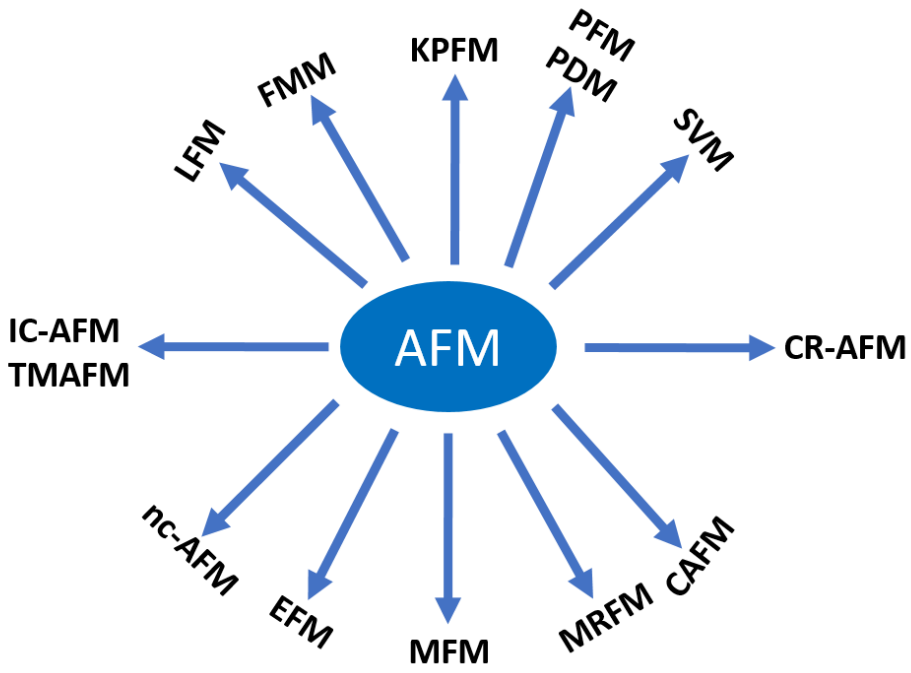

Figure 2.2: Various methods in AFM

Here are the full forms of the methods mentioned in the above figure:

1. PDM: Phase Detection Microscopy
2. PFM: Piezo response Force Microscopy
3. FMM: Force Modulation Microscopy
4. IC-AFM: Intermittent contact AFM
5. TMAFM: Tapping mode AFM
6. NC-AFM: Non-contact AFM
7. KPFM: Kelvin probe force microscopy
8. EFM: Electrostatic force microscopy
9. MFM: Magnetic force microscopy
10. MRFM: Magnetic resonance force microscopy
11. CR-AFM: Contact-resonance AFM
12. SVM: Scanning voltage microscopy / Nanopotentiometry

13. CAFM: Conductive AFM

Thus, having a vast application in all fields of science, AFM is achieving huge popularity.

2.3.1. Interatomic and intermolecular forces at the nanoscales

Intermolecular forces in case of AFM are from electromagnetic origin. The potential energy between the tip and the sample, P_{ts} causes z component of tip-sample force $F_{ts} = - \partial P_{ts}/\partial z$ and a tip sample spring constant very well known as the contact stiffness $k^* = - \partial F_{ts}/\partial z$. The tip sample interactions have contributions of both short and long range forces. Figure 2.3 shows the configuration of the tip and sample setup showing the various interaction forces with varied distance from the sample surface.

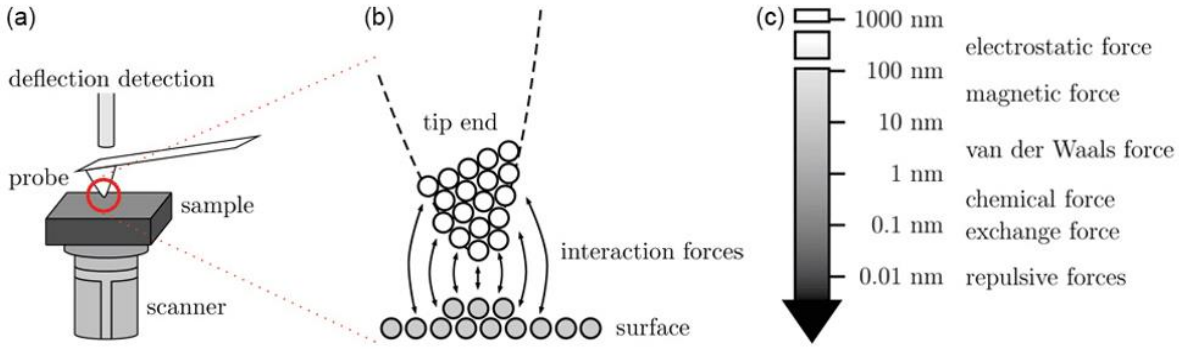

Figure 2.3: (a) Sketch of a macroscopically flat surface probed by a sharp tip. (b) At small separations the atomic structure of tip and sample becomes important and (c) various electromagnetic and interatomic forces as a function of distance of tip from the sample surface [34].

Interaction between the outermost atoms of the cantilever and surface atoms (both are considered to be neutral) can be approximated using attractive van der Waals forces. Well known Lennard Jones potential has an attractive term proportional to r^{-6} for large interatomic distance, i.e. the attractive side, which originates from the van der Waals interactions and a repulsive term proportional to r^{-12} for small r, where the repulsive forces are caused by the electron shells of atoms overlapping due to exchange and electrostatic interaction.

$$U(r) = 4\,\varepsilon\,[(\sigma/r)^{12} - (\sigma/r)^{6}], \quad (2.6)$$

where U, is the interatomic potential between two atoms or molecules, σ is the distance at which the two particles are at equilibrium, and ε is the strength of the interaction. The first term is responsible for the repulsion at short distance and the second term is responsible for the attraction at long distance. So, deeper the well depth (ε), stronger the interaction between two atoms or molecules.

The van der Waals interaction is caused by fluctuations in the electric dipole moment of atoms and their mutual polarization. For two atoms at distance z, the energy varies as $1/z^6$ [35].

For a spherical tip with radius R next to a flat surface (z is the distance between the plane connecting the centers of the surface atoms and center of the closet tip atom), the van der Waals potential is given by [36]:

$$V_{vdw} = -\frac{HR}{6z} \quad (2.7)$$

The van der Waals force for spherical tips is thus proportional to $1/z^2$, while the pyramidal and conical tips force law holds. The Hamaker constant, H, depends on the type of material (atomic polarizability and density) of the tip and sample and is usually of the order of 1 eV for most solids [36]. For a tip of radius R = 30 nm, the van der Waals force in vacuum at a distance of z = 0.5 nm is of the order of F_{vdW} = 2 nN. The van der Waals force can also be determined for more complex tip-sample geometries like a half-sphere at the end of a truncated cone. When obtaining AFM topography image, these van der Waals forces are sensed by an oscillating probe with oscillations < 1 nm which are usually excited at its fundamental frequency by a transducer when brought in close proximity to a sample surface. This mode is called the non-contact mode AFM. The resolution of this mode is defined by the tip sample separation which is just a few nm. Other forces acting at nanoscales are explained below in detail.

Interactions between charged ions, permanent dipoles etc. come under the category of electrostatic forces:

$$F_{el} = \frac{\partial C}{\partial z}(U_{bias} - U_{cpd})^2 \quad (2.8)$$

where, U_{bias} and U_{cpd} are the bias voltage and contact potential difference due to different work functions. AFM method using this type of force for sensing is the electrostatic force microscopy (EFM) which maps the contact potential.

There is another mode which senses the magnetic forces. It is called the magnetic force microscopy (MFM). Forces that act on magnetic dipoles located in a magnetic field are called magnetic forces. In MFM, the magnetic dipoles are usually contained in the ferromagnetic material on the tip of the cantilever and the magnetic sample. The force on the tip is given by the derivative of magnetostatic energy.

$$F_z(t) = -\mu \int M_{tip}(x', y', z') . \frac{\partial}{\partial z'} H_{sample}[(x', y', z') + t] dV' \quad (2.9)$$

Note that the *z*-derivative of the stray field is inside the integral expression. Thus, when the integration is performed along a long slab like tip, the integration along the z-axis will lead to an expression for the force, that is proportional to the stray field times the magnetic charge at the lower tip end (plus the stray field times the magnetic charge at the upper tip end – however for a long tip this part could be neglected). The magnetic force is proportional to the stray field. Other AFM methods utilizing chemical forces, solvation forces, and exchange forces are named as chemical force microscopy (CFM), liquid AFM (LAFM) and magnetic exchange force microscopy (MExFM), respectively.

2.3.1.1. Force-distance curves

The Lennard-Jones potential describes the potential energy of interaction between two non-bonding atoms or molecules based on their distance of separation. The potential equation accounts for the difference between attractive forces (dipole-dipole, dipole-induced dipole, and London interactions) and repulsive forces. AFM force-distance (FD) curves have become a fundamental tool in several fields of research such as surface science, materials engineering, biochemistry and biology [37]. FD curves help us to understand different types of interactions and the physics of the interactions. FD curves can be simply explained by the Lennard Jones potential curve, which is the nature of the obtained curve due to the interaction. The distance controlled during the measurement is not the actual tip-sample distance (d), but the distance (Z_{ts}) between sample surface and the rest position of the cantilever. These two distances differ because of cantilever deflection δ_c and of the sample deformation δ_s.

These quantities are related as follows:

$$d = Z_{ts} - (\delta_c + \delta_s) \tag{2.10}$$

Figure 2.4 shows the cantilever deflection during tip sample interaction and different zones in force distance curves. Towards the right of the curve in Figure 2.4 (b), in the attractive regime, force is negative which explains the inverse square law of forces. In case of AFM, this is the region where the AFM cantilever tip is brought from the point, where, d is equal to zero (chosen arbitrary) and reaches to the attractive regime due the adhesion forces. At certain distance to the sample surface, tip of the cantilever ‘snaps in’. During this case, the adhesion forces are much larger than the forces, due to cantilever. The reverse phenomenon will occur during the retraction called ‘snaps out', when tip pulls away.

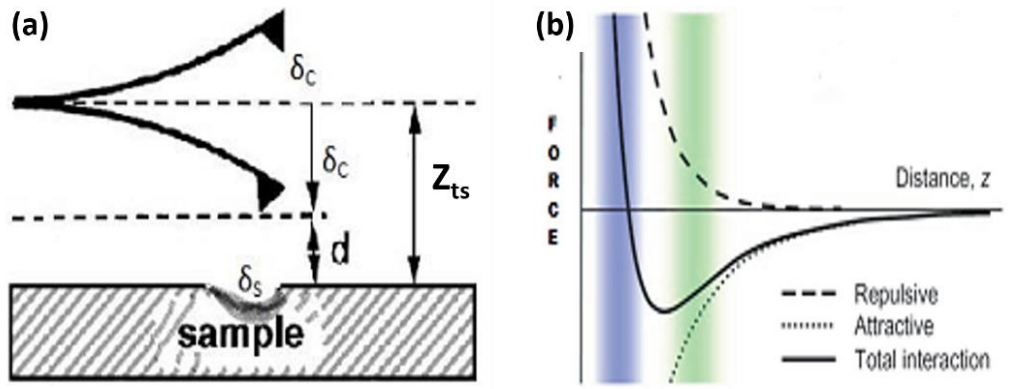

Figure 2.4: (a) Tip-sample interaction with the cantilever deflection and (b) the potential well (Lennard-Jones) diagram showing various zones in FD curves [38]

The force of adhesion may be due to different factors such as van der Waals force (caused due to polarization) and capillary force (due to ambient condition). The magnitude of these forces depends on the true contact area and nature of the attractive forces holding the surfaces together. The basic analysis of force measurement can be understood by application of different theories like Johnson-Kendall-Robert (JKR), Derjaguin-Muller-Toporov (DMT), Maugis, Carpick, Ogletree and Salmeron (COS) etc. [39] . If we go to the left side of the curve in Figure 2.5, we get the repulsive regime which explains about the elasticity and inelasticity of the sample for AFM measurement. We can calculate the force applied by the cantilever on to the surface by calculating the slope on the contact side. Hooke's law for springs states that,

$$F = - k_c * \delta_c \tag{2.11}$$

k_c, being the spring constant of cantilever and δ_c, the deflection of the cantilever. The negative sign tells that it is a restoring force. Spring constant of the cantilever can be calculated if the cantilever dimensions are known and is usually provided by the vendor.

A hysteretic behavior can also be seen in the FD curves which can be used to calculate the adhesion on the sample. This hysteretic behavior appears when the cantilever is retracted from the surface. The hysteresis occurs due to necking of the soft sample itself as described by the JKR interaction

model. Thus, JKR interaction is called the dissipative interaction, where there is a net loss of energy. Whereas, DMT type of interaction are called the conservative interaction as the force depends on the gap between the tip and the sample [38]. Various models have been proposed to study the behavior at contact. These models will be discussed in detail in the next section.

2.3.2. Contact models for tip sample interaction

Contact mechanics is the study of the deformation of solids that touch each other at one or more points. There are various models for description of the nano elastic contact with the surface. The particular choice of model to be used will be based on adhesive interactions, the tip shape and the applied load. Figure 2.5 shows the different contact mechanics models used to understand the tip sample interactions.

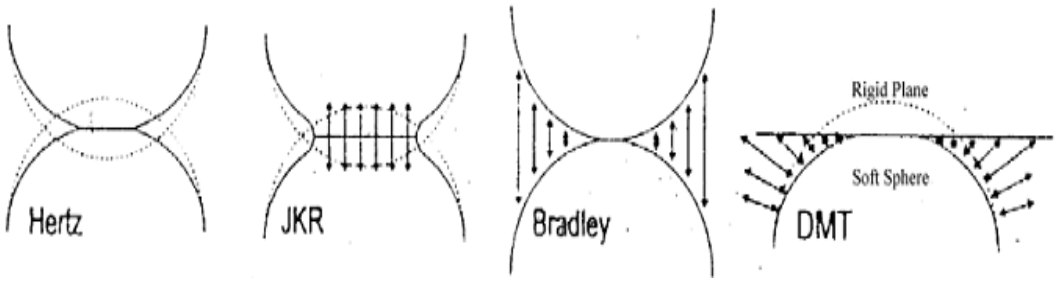

Figure 2.5: Various contact models at nano contact

Hertz theory (1880) for elastic deformation relates the circular contact area of a sphere with a plane (or more general between two spheres) to the elastic deformation properties of the materials. In the theory, any surface interactions such as near contact van der Waals interactions and contact adhesive interactions are neglected. Johnson et al. [40] have improved this Hertz theory by including the adhesion term, which is well known as JKR theory. A more involved is the DMT theory which also considers van der Waals interactions outside the elastic contact regime, which give rise to an additional load. The theory simplifies to Bradley's van der Waals model if the two surfaces are separated and significantly apart. In Bradley's model, any elastic material deformation

due to the effect of attractive interaction forces are neglected. The assumptions made in different contact mechanics models are summarized in Table 2.2.

Table 2.2: Assumption made for different Contact Mechanics Models [40]

Model	Assumptions
Hertz	fully elastic model, neglects adhesion
JKR	fully elastic model considering adhesion in the contact zone
Bradley	purely Van der Waals model with rigid spheres
DMT	fully elastic, adhesive and Van der Waals model

Hertz contact model:

The Hertz model deal with the contact between two surfaces at nanoscales. It is valid for isotropic elastic half spaces. For anisotropic materials, the shape of the contact area and the surface displacements in the contact area depend on the orientation of the crystal lattices and on the single-crystal elastic constants of the contacting bodies [15]. Theoretical examinations showed that the contact area is circular if there exists a three-or fourfold rotational symmetry axis perpendicular to the contacting surfaces, which holds, e.g., for (001) and (111) surfaces of cubic crystals. So, Hertz theory can still be applied for single crystals. But the difference is to use new constants M_s and M_{tip}, which would depend on the elastic single-crystal constants and on the orientation of the materials in the contact area. Contact between the two bodies occurs over many small areas, each of which constitutes a single asperity contact. It is necessary to relate the force acting on a single asperity to its deformation and contact area [41]. Contact between two continuous, non-conforming solids is initially a point or line. Under the action of a load the solids deform and a contact area is formed. Hertz contact stress theory allows for the prediction of the resulting contact area, contact pressure, compression of the bodies, and the induced stress in the bodies.

The effective radius of curvature is defined by the radii of curvature of the two solids as,

$$\frac{1}{R} = \frac{1}{R_1} + \frac{1}{R_2} \tag{2.12}$$

In a similar manner, the effective modulus of elasticity can also be defined by the modulus of elasticity and Poisson's ratio of the individual solids. Moduli (different authors use either *E* or *K* = $\frac{3}{4}$*E*) are computed as:

$$\frac{1}{E^*} = \frac{1-\vartheta_{tip}^2}{E_{Tip}} + \frac{1-\vartheta_s^2}{E_S} \tag{2.13}$$

or

$$\frac{1}{K} = \frac{4}{3}\left(\frac{1-\vartheta_{tip}^2}{E_{Tip}} + \frac{1-\vartheta_s^2}{E_S}\right) \tag{2.14}$$

E^* is the reduced modulus, E_{tip}, E_s, ϑ_{tip} and ϑ_s are the elastic modulus and Poisson's ratio of tip and the unknown sample.

If a sphere of radius *R*, is pressed against a flat surface with force F_c, then the adhesion force F_{ad}, the contact radius a_c, the contact radius at zero load a_0, the deformation δ of the indenter, and the resulting pressure *P*, under the indenter are defined as follows:

$$F_{ad} = 0, \tag{2.15}$$

$$a_c = \sqrt[3]{\frac{3RF_c}{4E^*}}, \tag{2.16}$$

$$\delta = \frac{a_c^2}{R} = \frac{3F_c}{4E^* a_c}, \tag{2.17}$$

$$P(x) = \frac{9E^*\sqrt{1-x^2}}{4\pi R} = \frac{3F\sqrt{1-x^2}}{2\pi a_c^2}, \tag{2.18}$$

$x = y/a_c$ where y is the distance from the center of the contact circle and E^* is the reduced modulus.

2.4. AFM BASED TECHNIQUES FOR QUANTITATIVE NANOMECHANICAL PROPERTY MEASUREMENTS

In the last three decades, AFM has proved itself to be the only reliable source for nano level imaging in air as well as in liquids. It has been explored for studying various properties such as conductivity, surface resistance, friction, modulus and damping. Many AFM based techniques have emerged for nanomechanical property measurements. They are listed below:

2.4.1. Multifrequency AFM methods

Multi frequency AFM techniques [42] are emerging techniques for measuring the nano mechanical properties in various materials. They rely on excitation/detection of several frequencies of the probe's oscillation. These frequencies are usually associated with either the higher harmonics of the oscillation or eigen mode of the micro cantilever. They provide high sensitivity and resolution and are designed for decoding the nonlinear regions of the tip surface interaction forces. Different multifrequency AFM methods for nanomechanical property measurements are described below:

- **Multi harmonics AFM imaging [43]**: The multi harmonic AFM imaging is the straight forward method where it just records and plots the higher harmonic components generated while acquiring a topography image. It has been demonstrated even in liquid environments. Combination of several harmonics have allowed the nano scale mapping of stiffness and viscoelastic dissipation in living cells.
- **AM-FM viscoelastic mapping [44]**: In AM-AFM, the probe is excited at a fixed frequency and the amplitude is held constant by the feedback loop while taking image. Wherein, for the FM-AFM, frequency shift is held constant by the feedback loop. By using the amplitude and phase data (AM-AFM) and using the frequency and quality factor data (FM-AFM), one can calculate the nano mechanical properties with good accuracy.

- **Bi modal AFM [45]** : Two driving forces are used to excite the micro cantilever. The excitation frequencies are tuned to match two of the flexural eigen modes of the cantilever, usually first and second eigen modes. First eigen mode output can be utilized to image the topography and the second eigen mode output (amplitude/phase) is used for measuring the changes in mechanical, magnetic and electrical properties of the surface.
- **Torsional harmonic AFM [46]**: Here, the torsional modes are utilized and torsional harmonic is used for generating a topography image of the sample surface and at the same time, the time varying forces are recorded. Specially designed cantilevers are used, where the tip is offset from the cantilever axis. Such design favors the existence of a torque around the axis of cantilever, which enhances the presence of large number of harmonics needed to have an accurate calculation of time varying forces and thus calculate mechanical properties such as young's modulus.
- **Microsecond force spectroscopy [47]**: By utilizing the torsional harmonic cantilevers (THC), one can acquire force curves with high speeds while obtaining the topography. In addition, owing to the microsecond duration of force loading, the mechanical properties derived from these waveforms will reflect molecular behavior at the microsecond timescale.

The multifrequency AFM based techniques have shown their potential in measuring elastic and viscoelastic properties in only soft materials.

2.4.2. Contact resonance based AFM methods

Contact resonance AFM (CR-AFM) techniques have been successfully developed and proved their ability to measure nanoscale mechanical properties with high spatial resolutions. CR- AFMs have been used to measure elastic modulus of materials ranging from a few MPa to

hundreds of GPa. These techniques have shown their capability in determining nanoscale mechanical properties in one dimensional, two dimensional and three dimensional structures.

Contact resonances can be triggered by using various methods:

- Dual AC Resonance Tracking (DART) [48]
- Band excitation (BE) [49, 50]
- Frequency sweep [15, 51]
- Phase-Locked Loop (PLL) frequency tracking [52]
- Fixed frequency [53]
- SPRITE: Excites two CRFs simultaneously [54]

Any of the above methods can be used for triggering the contact resonances. The above mentioned triggering methods vary with their response time and tracking parameter. Tracking amplitude, phase, frequency or Q factor can lead to better detection and faster analysis for the nanomechanical properties of the materials. A few widely used CR-AFM methods are briefly described below:

- **AFAM [53]**: The principal difference between AFAM and other forms of AFMs is the addition of a transducer at the bottom of the sample which induces longitudinal out-of-plane vibrations in the specimen. The vibrations are sensed by a probe while in contact with the sample. The amplitude of these probe's vibrations at various excitation frequencies are detected from the AFM photodiode signal by use of a lock-in-amplifier. The probe's response as a function of frequency can be acquired by sweeping a wide range of frequencies. The contact resonance spectra obtained are used to calculate the contact stiffness (k^*) and the local contact damping using suitable mechanical models for the tip-sample contact. This technique enables to image and measure local elasticity and damping of sample surfaces with a spatial resolution of the order of a few tens of nanometers.

- **Ultrasonic atomic force microscopy UAFM [55]**: It is similar to AFAM and varies only by vibrating the cantilever when in contact with the sample. Similar procedure is used for measuring elastic properties of the materials as in AFAM.
- **Lorentz contact resonance (LCR)** [56]: Lorentz Contact Resonance is based on the Lorentz force, the force on an electrical current in a magnetic field. An oscillating current passing through a specially designed probe (similar geometry as silicon cantilever but incorporated with resistive heater at the end of cantilever) interacts with a magnetic field that is focused near the probe. The interaction between the magnetic field and the electric field causes a perpendicular force in the cantilever resulting in an oscillating behavior of the cantilever. Driving the tip in this fashion, instead of with a piezoelectric crystal, has many advantages, including no moving parts in the drive system leading to clean cantilever resonance spectra with no parasitic peaks. This can be used to study temperature dependent variations in sample's mechanical properties.

2.4.3. Other AFM based techniques:

- **AFM Nanoindentation [57]:** This is similar to a nanoindentation testing. It makes crater and is time consuming as it is a point measurement. Suitable for soft materials only.
- **Friction force microscopy [58]**: It uses the lateral modes to determine the friction properties of the materials.
- **Force curves/mapping [37]**: Obtaining single or multiple force distance curves and analyzing these curves would help to determine the nanomechanical properties of materials. Suitable for soft materials only.
- **Loss tangent/phase imaging [59, 60]**: Loss tangent imaging is a recently introduced quantitative technique that recasts the interpretation of phase imaging into one term that includes both the dissipated and stored energy of the tip sample interaction. By

mapping the phase of the cantilever oscillation during the tapping mode scan, phase imaging goes beyond simple topographical mapping to detect variations in composition, adhesion, friction, viscoelasticity, and perhaps other properties.

The above mentioned techniques can be used to study the nanomechanical properties in a material with small, fast, and low noise cantilevers. This enables, measurements at noise levels and speeds previously impossible with high resolutions and can be used to study material modulus ranging from few Pa to few hundreds of GPa.

2.5. ATOMIC FORCE ACOUSTIC MICROSCOPY

After the invention of the AFM, near field microscopy was strongly promoted and various operation modes and related techniques emerged. The most promising technique for quantitative analysis are dynamic approaches in which the cantilever vibrates at or near its resonance frequencies [61]. These approaches are acoustic and ultrasonic with frequencies in the range of 100 kHz to 3 MHz. Since 1993, several microscopes combining AFM with ultrasonic imaging have been developed, e.g. ultrasonic force microscopy (UFM), scanning acoustic force microscopy (SAFM), AFAM and UAFM [62]. These techniques can be considered as special types of dynamic force microscopy or as near-field techniques from the point of view of ultrasonic imaging. The radius of the sensor tip in AFM, is in the range of a few nm to several 100 nm. The tip–sample contact radius, which is orders of magnitude smaller than the acoustic wavelength, defines the local resolution. The tip used in these experiments resembles the horn in impedance spectroscopy or of the contact oscillators in Fokker bond test where the tip-sample contact probes the local mechanical impedance [63].

A few typical applications and highlights of the AFAM technique are listed below:

- AFAM is a state-of-the-art AFM technique that can be used to map variations in surface elastic properties of soft as well as very hard samples where other techniques, such as phase imaging, force modulation and multifrequency techniques fail.
- AFAM enables to measure elastic properties of thin films, which cannot be measured with the use of other techniques.
- With AFAM, it is possible to obtain quantitative values of elastic modulus with high precision.
- It is possible to study the internal friction using AFAM
- The contrast of AFAM images is much sharper compared to those obtained in phase imaging or force modulation mode.
- It can be operated in air as well as in a liquid environment (in a droplet).
- It is a non-destructive technique.
- Possibility for studies on flaw characterization and detection of hidden structures

2.5.1. Experimental setup

Figure 2.6 shows the schematic of the experimental setup for AFAM and UAFM. In the AFAM setup, the sample is coupled to a piezoelectric transducer under it. Transducer emits longitudinal acoustic waves into the sample, which cause out-of-plane vibrations on the sample surface. The surface vibrations are transmitted into the cantilever via the sensor tip. However, in case of UAFM the cantilever is vibrated using the transducer placed on the cantilever holder. The cantilever vibrations are measured by a 4-sectioned photo-diode and evaluated by a lock-in amplifier. This setup can be used either to acquire cantilever vibration spectra or to take acoustic images. The latter are maps of cantilever amplitudes at a fixed excitation frequency near its resonance frequency. The contact-mode topography image is acquired simultaneously with the acoustic image.

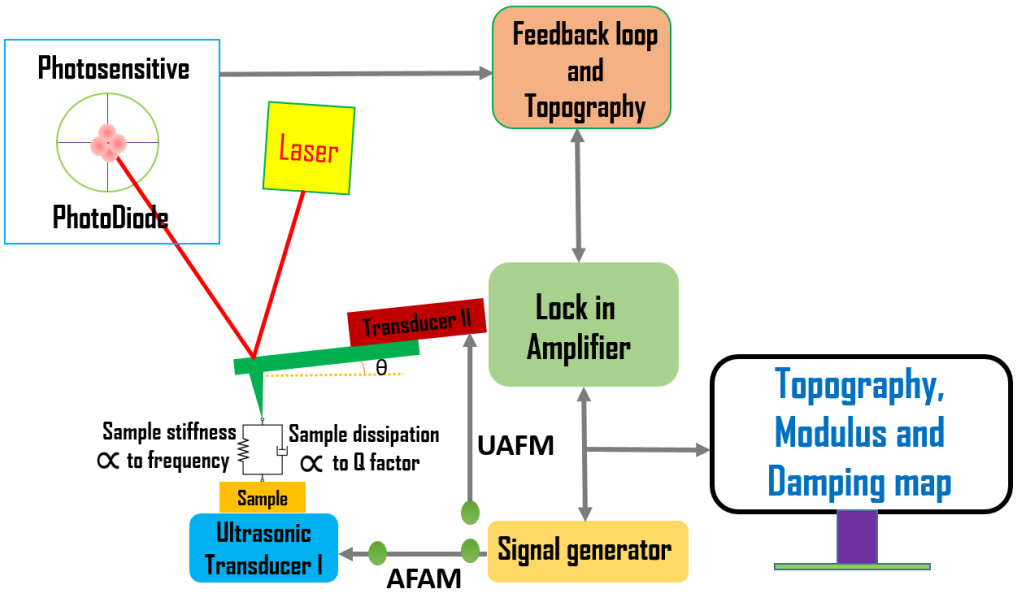

Figure 2.6: Schematic setup for AFAM and UAFM

2.5.2. Theory

By utilizing amplitudes and phase of the contact resonances, one can get the elastic properties of samples in qualitative way. But for quantitative analysis, detailed study on the CRFs are required. For the quantitative evaluation of the material physical properties from the CR spectra, two models are used:

1. Cantilever dynamics model and
2. Contact mechanics model

Cantilever dynamics model is used for deriving the k^* from the CRFs, whereas the contact mechanics model helps to derive the reduced modulus from the k^*. Details of these models are provided in the following sections.

2.5.2.1. Cantilever dynamics model deserting damping

Before going into the details of dynamics of cantilever, lets glance through the basics of cantilever beams. A cantilever is a beam anchored to one end and free at the other end, similar to a diving board at the swimming pool. Cantilever beams have a variety of loading options like end

moment, end load, uniform distribution, triangular distribution and intermediate load. Variations in the loading, defines the suitable mechanical models used for calculations such as point mass (end load) and cantilever dynamics model (uniform load). The flexural modes determine the elastic properties and the torsional modes can be utilized to measure the shear properties of materials [64].

Cantilever beams generally follow the Euler-Bernoulli beam principle i.e. the deflection of the beam can be studied using the curvature of the beam, K, which is the second derivative of the deflection and this curvature can be related to the bending moment, M and the flexural rigidity, EI.

$$K = \frac{\partial^2 y}{\partial x^2} \tag{2.19}$$

$$K = \frac{M}{EI},\ I = \frac{bh^3}{12} \tag{2.20}$$

E=Elastic Modulus, I=Area moment of inertia

The moment of inertia measures the beam's ability to resist bending. The larger the moment of inertia, the less the beam bends. Moment of inertia mainly depends on the geometry of the beam and the reference axis. The out of plane displacement, *y*, can be governed by the engineer's beam theory. It is a combination of the four sub- categories like [65]:

Kinematics -> Constitutive - > Resultants -> Equilibrium = Beam equation

$$\frac{\partial^2}{\partial x^2}\left[EI\frac{\partial^2 y}{\partial x^2}\right] = p \tag{2.21}$$

where, *p* is the load. If *E* and *I* do not vary with *x* along the beam, then the simplified equation is,

$$EI\left[\frac{\partial^4 y}{\partial x^4}\right] = p \tag{2.22}$$

When damping is neglected then the equation of motion for flexural vibrations will be:

$$EI\frac{\partial^4 y}{\partial x^4} + \rho A\frac{\partial^2 y}{\partial t^2} = 0 \tag{2.23}$$

Here, E is the Young's modulus, I, the area moment of inertia, ρ, the mass density and A is the area of cantilever. Figure 2.7 depicts the tip sample contact without considering damping.

$EI\frac{\partial^2 y}{\partial x^2}$ is the torsional moment and $EI\frac{\partial^3 y}{\partial x^3}$ is the shear force.

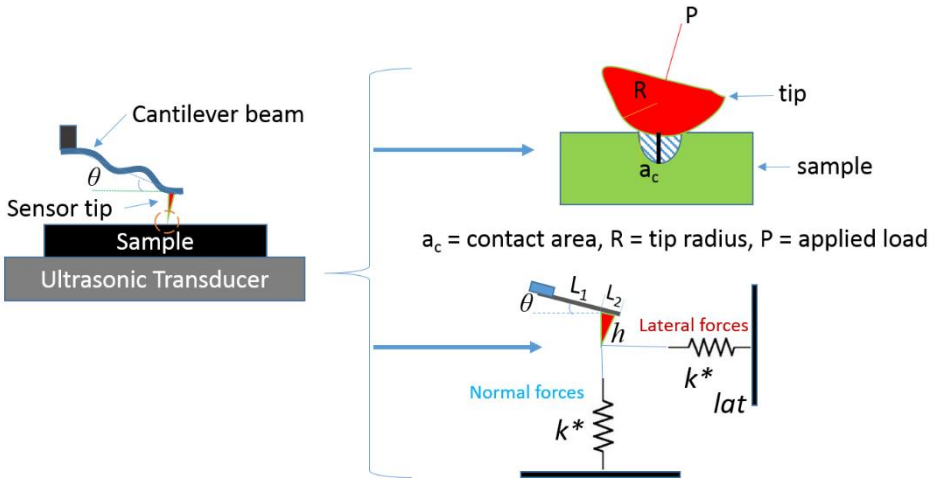

Figure 2.7: Schematic of the interaction of the tip with the sample neglecting damping

The general solution for this equation (2.23) is:

$$y(x,t) = (a_1 e^{kx} + a_2 e^{-kx} + a_3 e^{ikx} + a_4 e^{-ikx})\, e^{-i\omega t} \tag{2.24}$$

Where $k = \frac{2\pi}{\lambda}$ is the wave number, $\omega = 2\pi f$ is the angular frequency and a_i (i=1, 2, 3, 4) are the constants.

Calculating the derivatives of equation (2.24) and inserting them in equation (2.23), following dispersion relation is obtained:

$$EIk^4 - \rho A\omega^2 = 0 \tag{2.25}$$

The boundary conditions for the clamped free beam should fulfill the following conditions. At the clamped end (x=0), the deflection and slope must be zero:

$$y = 0, \quad \frac{\partial y}{\partial x} = 0 \tag{2.26}$$

At the free end of the beam (x=L), no moment or shear force can be present:

$$\frac{\partial^2 y}{\partial x^2} = 0, \ \frac{\partial^3 y}{\partial x^3} = 0 \tag{2.27}$$

Using the boundary conditions in equations (2.26) and (2.27) and properties of trigonometric functions one obtains the characteristic equation:

$$cosk_nL + coshk_nL = -1 \tag{2.28}$$

For which the solutions k_nL, n = 1, 2, 3…. give the wave numbers, k_n of an infinite set of flexural modes. Equation (2.29) can be used to calculate the resonant frequency f_n of the nth mode.

$$f_n = \frac{(k_n\mathrm{L})^2}{{c_c}^2} \tag{2.29}$$

$$c_c = L\sqrt{2\pi}\left(\sqrt[4]{\frac{\rho A}{EI}}\right) \tag{2.30}$$

$$\frac{f_n}{f_1} = \left(\frac{k_nL}{k_1L}\right)^2 \tag{2.31}$$

c_c is a constant dependent on the geometry of the cantilever and its mechanical properties. The values of the dimensionless wavenumber and corresponding frequency ratios of clamped – free cantilever for the first five modes calculated using equation (2.31) are given in Table 2.3. The deflection of the nth mode, $y_n(x)$, is given by:

$$y_n = y_0\left[(cosk_nx - coshk_nx) - \frac{cosk_nL+coshk_nL}{sink_nL+sinhk_nL}(sink_nx - sinhk_nx\right] \tag{2.32}$$

where, y_o is the vibration amplitude of the sample surface directly under the cantilever tip.

Table 2.3: Values for the dimensionless wavenumber (k_nL) and frequency ratio ($f_{n,free}/f_{1,free}$) of the clamped – free cantilever for first five modes [12]

n	$(k_nL)_{free}$	$f_{n,free}/f_{1,free}$
1	1.875	1.00
2	4.694	6.27
3	7.854	17.55
4	10.995	34.39
5	14.137	56.84

When the tip is in contact with the sample and when the long range force acts on the tip, then the tip-sample forces can be considered as a linear spring with a characteristic spring constant k^*, which is the negative derivative of the tip sample interaction force in the equilibrium position:

$$k^* = -\frac{\partial F(z)}{\partial (z)} \tag{2.33}$$

where, *Z* is the distance between tip and sample and *F(z)* is the tip sample interaction force at the equilibrium position. Boundary conditions remain the same at x=0 as for the clamped – free cantilever and change at the spring coupled end. Spring coupled end cannot transfer the moment anymore, but a deflection, *y*, generates a force – k^*y which must be added to the shear force:

$$EI\frac{\partial^3 y}{\partial x^3} - k^* y = 0 \tag{2.34}$$

The new boundary condition at the spring coupled end at x=L are

$$\frac{\partial^2 y}{\partial x^2} = 0, \frac{\partial^3 y}{\partial x^3} = \frac{k^*}{EI} y = \frac{3k^*}{k_c L^3} \tag{2.35}$$

Including these boundary conditions, a new characteristic equation for the spring coupled cantilever is obtained.

$$sinhk_nLcosk_nL - coshk_nLsink_nL = \frac{(k_nL)^3 k_c}{3k^*}(1 + cosk_nL + coshk_nL) \tag{2.36}$$

This equation (2.36) will reduce to equation (2.28) when $k^* = 0$ and this implies that the cantilever is attached to an infinitely soft spring at x = L. But when $k^* \rightarrow \infty$, then the cantilever at x = L is pinned to the surface and the cantilever becomes insensitive to the elastic properties of the surface. The resonance frequencies of the system will shift to higher values called CRFs due to the tip-sample interactions. Contact stiffness (k^*) can be calculated, if the resonance frequencies of the clamped spring coupled system are known [12]. A characteristic equation can be formed to calculate the contact stiffness from the contact resonance frequencies by considering two unknowns as shown below [16]:

$$\left\{\begin{array}{c} \frac{2}{3}\frac{K_c}{k^*}(k_nL_1)^4 A + (k_nL_1)^3 \frac{h^2}{{L_1}^2}\left[sin^2\theta + c_p cos^2\theta\right] \times [D_1 \times A_2 - D_2 \times C_1] + \\ 2(k_nL_1)^2 \frac{h}{L_1} sin\theta\, cos\theta\left(c_p - 1\right) \times [\sin(k_nL_1)\sinh(k_nL_1) \times A_2 + \sin(k_nL_2) \\ \sinh(k_nL_2) \times C_1] + k_nL_1[cos^2\theta + c_p sin^2\theta] \times [B_1 \times A_2 - B_2 \times C_1] + \\ c_p\left[3\frac{k^*}{K_c}\frac{h^2}{L_1^2} C_1 \times A_2\right] \end{array}\right\} = 0 \tag{2.37}$$

Where

$A=1+\cos(k_nL)\cosh(k_nL)$ $B = \sin(k_nL)\cosh(k_nL)-\sinh(k_nL)\cos(k_nL)$

$C = 1-\cos(k_nL)\cosh(k_nL)$ $D = \sin(k_nL)\cosh(k_nL)+\sinh(k_nL)\cos(k_nL)$

Subscripts 1,2 used here are for L_1 and L_2 and holds for all A, B, C, D for example:

$D_1= \sin(k_nL_1)\cosh(k_nL_1)+\sinh(k_nL_1)\cos(k_nL_1)$

$D_2 = \sin(k_nL_2)\cosh(k_nL_2)+\sinh(k_nL_2)\cos(k_nL_2)$

For the calculations reported for the study in this thesis, the values for the angle of inclination of the cantilever, θ = 12 deg. The parameter $c_p = k^*_{lat}/k^*$ describes the ratio of the normal and lateral contact stiffness. $c_p = 0.85$ is found to be a reasonable value as reported earlier [15], h is the height of the sensor tip from the sample surface, h = 10 microns. The effect of tip length is also not negligible for higher contact stiffness values (usually > 40) [66].

The CRFs are obtained numerically by finding the roots of the normalized wave number of the n^{th} flexural mode, k_nL of the characteristic equation and by using equation (2.29) to calculate the resonance frequencies. But an inverse problem arises, where first we get the CRFs and then calculate contact stiffness. To achieve this, the known wave numbers and the free and contact resonance frequencies of the clamped beam can be used. The k_nL depends on the length L of the cantilever and its free and contact resonance frequencies [8]:

(k_nL) = Wave number, (n = 1,2,….) $(k_nL)_{contact} = (k_nL)_{free}\sqrt{\frac{f_{contact}}{f_{free}}}$ (2.38)

$(k_nL_1)_{contact} = \frac{L_1}{L}(k_nL)_{free}\sqrt{\frac{f_{contact}}{f_{free}}}$, $(k_nL_2)_{contact} = \frac{L_2}{L}(k_nL)_{free}\sqrt{\frac{f_{contact}}{f_{free}}}$ (2.39)

The values of $(k_nL)_{free}$ are known, for example, the value of $(k_1L)_{free}$ = 1.8751 holds for the first bending resonance of a clamped-free beam [8]. If the frequencies of two modes are known, one can write two equations containing two unknown values L_1 and k^*.

$$\left\{\frac{k^*}{K_c}\right\}_{1,2} = \frac{vh^2}{6c_pL_1^2C_1\times A_2} \pm \sqrt{\left[\frac{vh^2}{6c_pL_1^2C_1\times A_2}\right]^2 - \frac{(k_nL_1)^4L_1^2A}{69h^2C_1\times A_2}} \tag{2.40}$$

$$v = \left\{\begin{array}{c}(k_nL_1)^3\frac{h^2}{{L_1}^2}\left[sin^2\theta + c_pcos^2\theta\right]\times[D_1\times A_2 - D_2\times C_1] + \\ 2(k_nL_1)^2\frac{h}{L_1}sin\theta\ cos\theta\left(c_p-1\right)\times[\sin(k_nL_1)\sinh(k_nL_1)\times A_2 + \sin(k_nL_2) \\ \sinh(k_nL_2)\times C_1] + k_nL_1[cos^2\theta + c_psin^2\theta]\times[B_1\times A_2 - B_2\times C_1]\end{array}\right\} \tag{2.41}$$

By plotting k^* as a function of the tip position (L_1/L) for the two modes, one obtains two curves. The cross-point of the two curves, yields the unique value of k^* of the system using both the modes. Hence, in AFAM studies, CRFs for two modes are experimentally measured to derive the contact stiffness.

Dispersion curves depicts the sensitivity of the mode for materials with varied stiffness. Dispersion curves are plotted against normalized contact stiffness (k^*/k_c) and normalized CRF (f_{CR}/f_{ff}). The slope of the dispersion curve for each mode exhibits the sensitivity of that mode for a particular range of the stiffness values. Large variation in the k^* and subsequently in indentation modulus can be perceived with small variations in the normalized CRF values. Slope of the various modes decides the ability of the higher order modes for measurement of indentation modulus with better sensitivity and resolution. Figure 2.8 shows the dispersion curves obtained for three different cases, with an assumption, i.e. the tip is at the cantilever end (A), away from the cantilever end (B) and away from the cantilever end with lateral and normal forces acting on it (C) as shown in Figure 2.8. The third case in the figure would be truly depicts the real experimental condition.

Even if the lateral contact stiffness is of same value of the normal contact stiffness, its influence on the cantilever vibration is smaller than the influence through normal stiffness due to the factor h^2/L^2 used in the characteristic equation (2.37) [12]. The lateral contact stiffness would slightly influence the frequency if the k^* is found to be less than spring constant (k_c). With increase in the k^*/k_c to higher values, the influence of lateral contact stiffness is significant [12]. Sensitivity of different modes can be calculated using these dispersion curves.

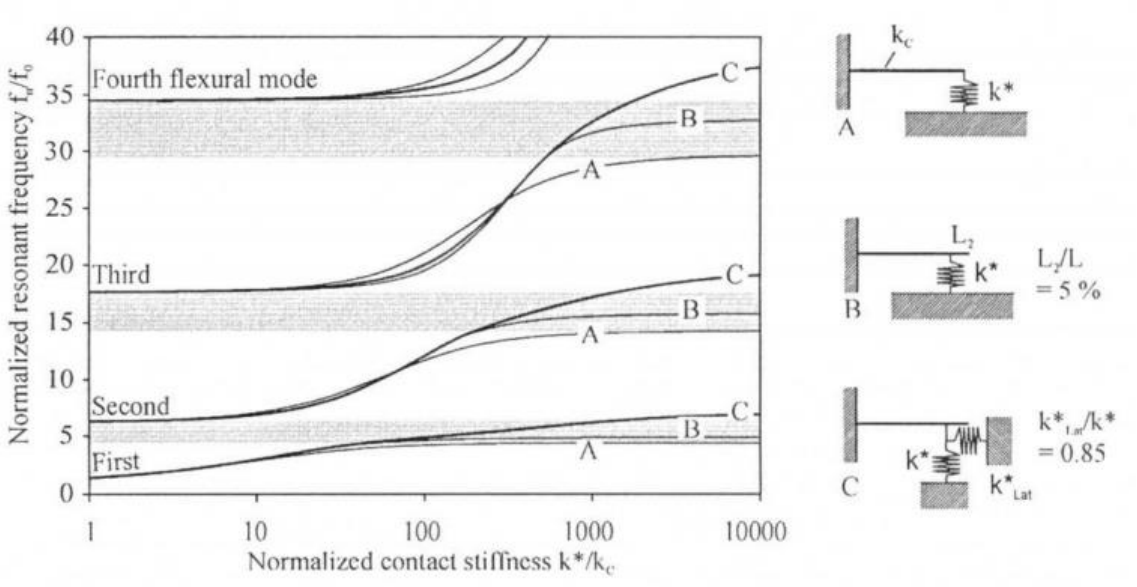

Figure 2.8: Dispersion curves obtained for three different conditions: (A) spring normal to the surface is fixed to the cantilever end, (B) normal spring is fixed slightly away from the cantilever end and (C) normal spring is away from the cantilever end with lateral and lateral tip sample force acting along with the normal forces [12]

A lot of work has been carried out to study the sensitivity of different modes and is found to have direct relationship with the contact stiffness [66-68]. The first mode is more sensitive, whereas, the higher modes become more sensitive, than the first mode for $k^*/k_c > 20$. Figure 2.9 shows the sensitivities of the first four modes for an AFM cantilever. Comparison of the modal sensitivity was made for sloped cantilever ($\theta = 15$ deg and $K_l = 0.9k^*$) and for a horizontal cantilever ($\theta = 0$ deg and $K_l=0$). Horizontal arrangement of cantilever is found to be more sensitive than the sloped one for smaller normal contact stiffness [66]. The effect of cantilever slope on the sensitivity of

flexural modes is significant and cannot be ignored [66]. Similar study was earlier carried out by Turner et al. [68] for a horizontal cantilever configuration. Concentrated mass cantilevers were also used to enhance the sensitivity in detecting the sample elasticity [69]. Flat tip with concentrated mass cantilever simplifies the nanoscopic elastic modulus evaluation with errors estimated to be <1 % [69].

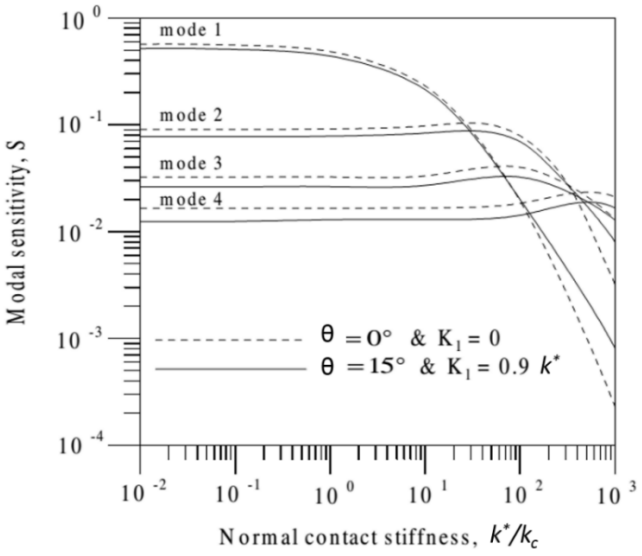

Figure 2.9: Sensitivity of first four flexural modes for a horizontal and sloped cantilever [66]

Marinello et al. [70] have studied in detail the effect of critical factors in AFAM such as cantilever geometry, force constant, resonance frequency and scan settings (speed and sample vibration frequency). Different probes, even of the same type and from the same batch, exhibit large variations in geometrical and mechanical properties. The variabilities in different cantilever parameters affecting the measurements for a given cantilever and different cantilevers are listed in Table 2.4. Table 2.4 describes the effect of various paramters on AFAM measurements for a given cantilever and different cantilevers. The (-) sign in the table indicates the term has no effect and remains constant. (+) and (++) signs indicate the corresponding parameter has small and large impacts, respectively.

Table 2.4: Variability effect of parameters with same and different probes [70]

Parameter	Variability	
	For a given cantilever	Between cantilevers
Length, *L*	-	++
Tip height, *h*	+	+
Incidence angle θ	+	+
Tip radius	++	++
Resonance frequency	-	++
Cantilever stiffness	-	++

2.5.2.2. Cantilever dynamics model considering damping

When considering the damping, the cantilever dynamics model can be modified with addition of a dashpot, representing damping. Hence, the equation of motion with inclusion of damping term now becomes:

$$EI\frac{\partial^4 y}{\partial x^4} + \eta_{air}\rho A\frac{\partial y}{\partial t} + \rho A\frac{\partial^2 y}{\partial t^2} = 0 \tag{2.42}$$

where, η_{air} is the damping in cantilever and dissipation caused by air.

Not only local contact stiffness and indentation modulus, but also local contact damping might be caused by various physical mechanisms [71]. Many studies have been carried out macroscopically on ultrasonic attenuation and internal friction on bulk samples, but very few studies have been carried out on damping measurements at the micron and nanoscales. AFAM allows us to study and understand the local damping occurring at the tip sample interaction volume. Figure 2.10 shows the tip sample configuration when considering damping.

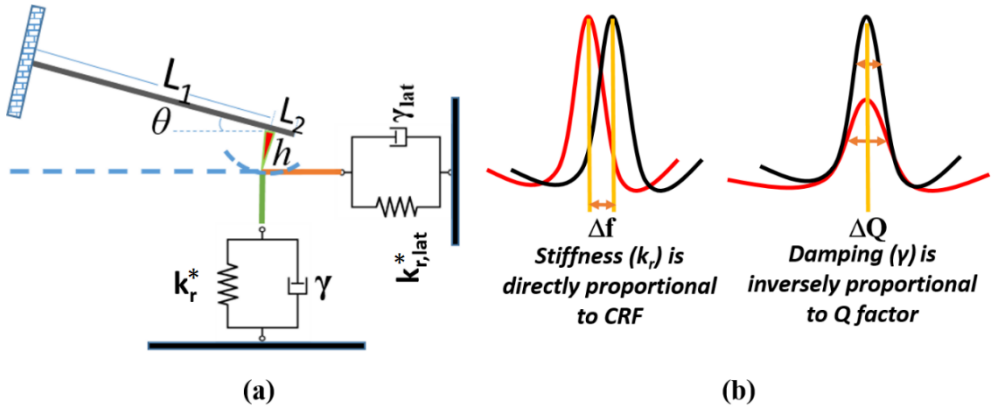

Figure 2.10: (a) Schematic of the tip-sample interaction with inclusion of damping term and (b) effect of sample stiffness and damping on contact-resonance spectra

In order to study the damping properties of the materials, we need to find the contributions for damping at the tip sample interaction volume. In the earlier AFAM studies reported before 2008, the damping at the contact was neglected. Yuya et al. [10] and Killgore et al. [9] have used models to fit the resonance curves, which have been employed for the calculation of damping in this thesis. By knowing the Q factor of the CR curves, the damping characteristics at the tip sample contact can be determined. By employing Euler-Bernoulli equation with the simple Kelvin-Voigt model, one can study the damping characteristics at the contact. The Q_{free} and $Q_{contact}$ can be determined by fitting the curves of the free resonance and the contact resonance, respectively using suitable fitting models. The damping values at nanoscales at every pixel of the map can be calculated using the Q_{free} and $Q_{contact}$.

Due to the local damping in the contact zone, the k^* becomes a complex quantity, $k^* = k_r + i\, k_i$, k_r is the real part of the contact stiffness and k_i is the imaginary part of the contact stiffness. In case of viscous damping in the contact zone, $k_i = \omega\gamma$, where ω is the angular frequency and γ is the interactive damping. Neither k_r nor k_i can be measured directly. Local damping Q_{loc}^{-1} is given by the ratio of the imaginary part of the contact stiffness to the real part.

So, it is convenient to introduce a complex quantity (λ_n +i η_n) in the characteristic equation [16]:

$$\lambda_n = \frac{k_r}{k_c} \text{ and } \eta_n = \gamma\sqrt{\frac{L_1^2}{9EI\rho A}} \tag{2.43}$$

where, λ_n is the normalized contact stiffness and η_n is the normalized damping constant. The parameter γ stands for the interaction damping in the contact zone, generally represented by a dashpot parallel to a spring.

When damping is taken into account, the wave-vector k_n describing the cantilever's motion becomes complex with a_n, its real part and b_n, its imaginary part. The imaginary part is caused by the damping of the tip-sample configuration, i.e. the damping in the contact-zone, and the damping of the cantilever motion in air. The cantilever resonance-frequencies determine the real part a_n, and the imaginary part b_n, is determined by the width of the contact-resonance curves [9, 10]:

$$k_n = (a_n + ib_n)/L, \text{ where, } a_n = C_n\sqrt{\frac{f_{cont}}{f_{free}}},\ b_n = \frac{2\pi f_{cont} - \frac{2\pi f_{free}}{Q_{free}}Q_{cont}}{8\pi f_{cont}Q_{cont}} \tag{2.44}$$

Here, $n = 1, 2, \ldots\infty$ are the mode numbers e.g.: $C_1 = 1.875$ for the first free resonance. In equation (2.44), it is neglected that the cantilever's damping by its motion in air is not the same for the free cantilever and the cantilever in contact [25]. However, due to the relatively high contact damping E''/E', which we observe in our experiments, we neglect this effect. The values for a_n and b_n are obtained by fitting Lorentzians to the experimentally obtained resonance curves of the free and contact resonances.

The above set of equations can be solved in order to obtain the real and imaginary parts of the wave vectors and the contact stiffness using equation (2.37). The details are explained by Yuya et al. [10, 25] and Killgore et al. [9]. Using the values obtained for λ_n and η_n from the dispersion

equation, one gets the local damping $Q_{loc}^{-1} = E''/E'$ values of the specimen at nanoscale. The damping for the first mode can be derived from the equation [25]:

$$Q_{n,loc}^{-1} = \frac{\omega\gamma}{k_r} = \frac{\eta_n}{\lambda_n}\frac{L}{L_1}\frac{\omega_{c,n}\times(k_nL)^2}{\omega_{free,n}} \approx 3.516\frac{\eta_1}{\lambda_1}\frac{L}{L_1}\frac{\omega_{c,1}}{\omega_{free,1}} \quad (2.45)$$

Here, ω and ω_0 are the contact and the free angular resonance frequencies, respectively. The right side of equation (2.48) holds for the first mode of a cantilever.

Chang et al. [67] studied the effect of interactive damping on the sensitivity of flexural modes of rectangular cantilevers. Figure 2.11 shows the effect of damping on the normal flexural mode sensitivity as a function of normal contact stiffness (k^*/k_c). Flexural sensitivities of the first three modes apparently fall, when damping is taken into account. For lower stiffness, damping effect is more. As the k^*/k_c increases, damping effect decreases and sensitivity increases. As the value of k^*/k_c increases, the higher modes become more sensitive. Higher damping coefficients can affect the large range of k^*/k_c values.

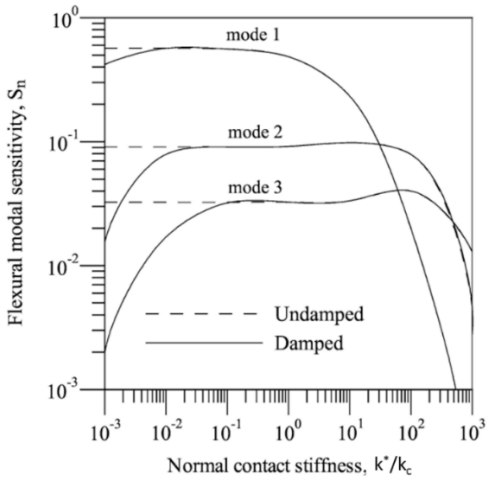

Figure 2.11: Flexural modal sensitivities as a function of normal contact stiffness. [67]

2.5.2.3. Contact mechanics model (CMM)

After calculating the normalized contact stiffness (k^*/k_c) values, using the cantilever dynamics model, the elastic properties of the sample can be calculated using a suitable CMM.

CMM providing a relation between k^* and the reduced modulus for the tip-sample contact. For metallic materials, Hertz contact model can be effectively used, as the adhesion forces are much smaller than the elasticity forces and hence adhesion can be neglected. The analysis procedure is similar to the nanoindentation methods. Figure 2.12 show the representation of Hertzian contact between a hemispherical and a flat sample.

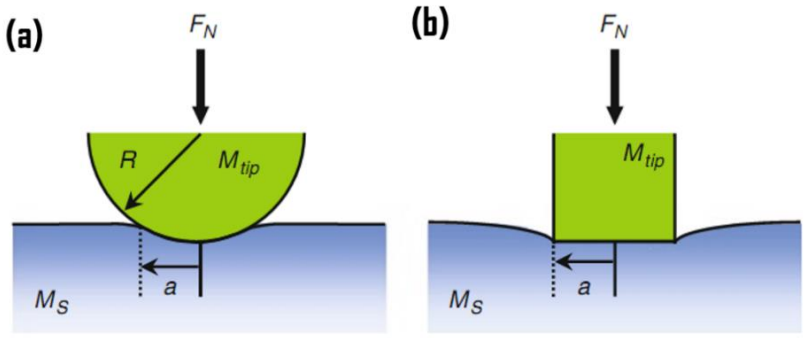

Figure 2.12: Contact mechanics schematics: (a) Hertzian contact between the hemispherical contact and flat sample and (b) flat punch contact between a flat tip and a flat sample [72].

In either case, the normal contact stiffness can be defined as:

$$k^* = 2aE^* \tag{2.46}$$

where E^* is the reduced modulus and a is the contact radius.

Substituting equation (2.16) in (2.49) we get:

$$k^* = \sqrt[3]{6RPE^{*2}} \tag{2.47}$$

Here, R is the radius of curvature of the cantilever tip and P is the load applied on the sample by the cantilever. There is one unknown, R, which can be eliminated using a reference method. Reference material can either be a single crystal with known orientations or an amorphous material.

$$\frac{k^*_{sample}}{k^*_{Reference}} = \left(\frac{E^*_{sample}}{E^*_{Reference}}\right)^{2/3} \tag{2.48}$$

In the above approach, the values of R and P are assumed to be the same during measurements on the sample and the reference. However, more often than not, this is not found to be true [27, 28]. Switching samples have often been shown to change the CRF of the cantilever when brought back

to the same sample, for both single crystals and amorphous samples [29]. AFAM being a contact-mode AFM technique, the tip condition often changes continuously/abruptly during scanning the sample. This is more often during scanning on metallic materials owing to the presence of scratches or second phase particles. To get rid of this, matrix of the polycrystalline materials can be used as a reference [15, 73] which will avoid measurement on a separate reference. E^* is the reduced system modulus between the tip and the sample:

$$\frac{1}{E^*} = \frac{1}{M_S} + \frac{1}{M_T} \tag{2.49}$$

M_S and M_T are the indentation modulus of sample and the tip, respectively. For elastically isotropic materials, the indentation or plane strain modulus, $M = \frac{E}{1-\vartheta^2}$, where E is Young's modulus and ϑ is Poisson's ratio. Then

$$\frac{1}{E^*} = \frac{1-\vartheta^2}{E_{Tip}} + \frac{1-\vartheta^2}{E_S} \tag{2.50}$$

Dual reference approach can also be used to obtain quantitative values with an accuracy of 3% [74]. This approach will not only eliminate tip geometry parameter but also the tip indentation modulus [8]. Detailed step wise procedure and description of data analysis using contact resonance spectroscopy can be found in Appendix 5A of [75].

2.5.3. Elastic property measurements using AFAM

AFAM has been extensively used for modulus measurements in soft materials like polymers [18], composites [21], biological cells [76], plants [19] and stiff materials like polycrystalline materials [11, 15].

In 1994, Rabe et al. [53] published the first article on AFAM where they reported that the construction of an AFM enables not only to obtain the topography of the sample but one can also simultaneously monitor the ultrasonic surface vibrations in the MHz range. Later, it has been

extended to GHz range to unravel the mysteries beyond the surface level [77]. In 1996, the same group studied the theory behind the AFAM and carried out experiments to prove their proposed flexural theory [78]. A flexural theory was proposed and found to be in good agreement. Figure 2.13 shows the normalized resonance frequencies of a spring coupled cantilever as a function of k^*/k_c and was compared with the point mass model. It is clear from the figure that the model shifts from clamped free to clamped-pinned as k^*/k_c increases. The point mass model fails, when $k^* > k_c$, as k_c become negligible compared to k^* and also it predicts too large frequency shifts, when $k^*/k_c > 1$. Local vibration amplitudes along a rectangular cantilever for the first three modes for different k^*/k_c values are shown in Figure 2.14. For very soft cantilevers, the amplitudes are found to be maximum at the end of the cantilever and increase compared to the clamped-free case. With increase in spring stiffness the slopes at the end of cantilever go through zero and change their sign. With further increase in k^*, the maximum of the amplitude is no longer at the cantilever end and decrease until they become zero similar to pinned case as shown in Figure 2.14 (d). The frequency shifts caused by the tip sample elasticity depends on the geometry of the cantilever beam. They also found that there is a significant increase in damping when the sensor tip comes close to the surface.

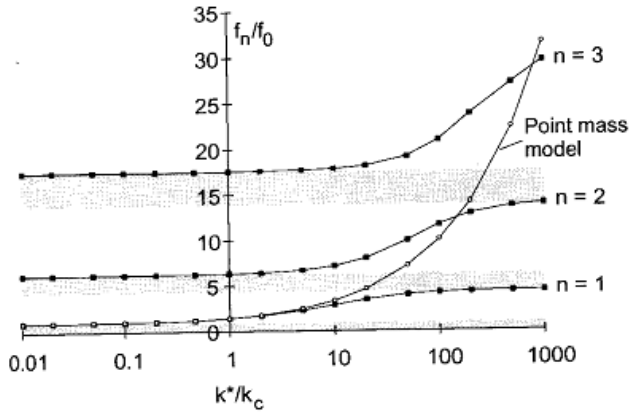

Figure 2.13: Dispersion curves shown for the first three modes compared with the point mass case (open circles) The grey areas indicate the frequency gaps [78].

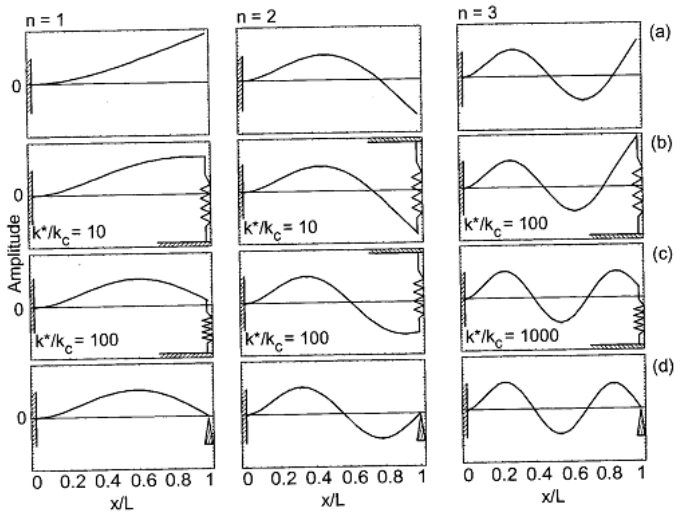

Figure 2.14: Local vibration amplitudes for the first three modes. Free vibration to pinned cases are depicted in a to d [78]

Later, Caprick et al. [79] have studied the lateral stiffness components using the friction force microscopy. Study discusses a fast and straight forward method to determine the shear strength of the tip sample contact independent of the contact mechanics models by measuring the lateral contact stiffness. They also quote that the radius values are not required for calculating total stiffness.

Kester et al. [80] have performed point measurements on RF sputtered thin films of magnetite and maghemite. The data was obtained using second mode and constant load. Irrespective of the same crystalline structure and grain size, maghemite was found to be softer than magnetite. The variation was because of the cation vacancies present in the maghemite.

In the subsequent year, Kester et al. [81] published extended work on the nanocrystalline ferrites with spinel structures. Young's modulus of these materials were plotted against the oxidation temperature. Measurements were carried out using first and third mode of stiff cantilevers, which can surmount adhesion forces acting at the contact and also allow active control of static force. By plotting k^* as a function of the tip position (L_1/L) for the two modes, one obtains two curves, the

cross-point of the two curves, yields the unique value of k^* of the system. Because the model used was a simplified one and neglected damping it showed only an approximation for the experimental situation. Hence, all the three modes did not meet at one particular point as shown in Figure 2.15. Single crystal silicon was used as a reference to obtain the values for the ferrites. Measurements corroborated the existence of chemical gradients from the surface layer to the interior of the films occurring during the oxidation process in gamma phase. This led to stress gradients which influenced the Young's modulus and the coercivity, H_c.

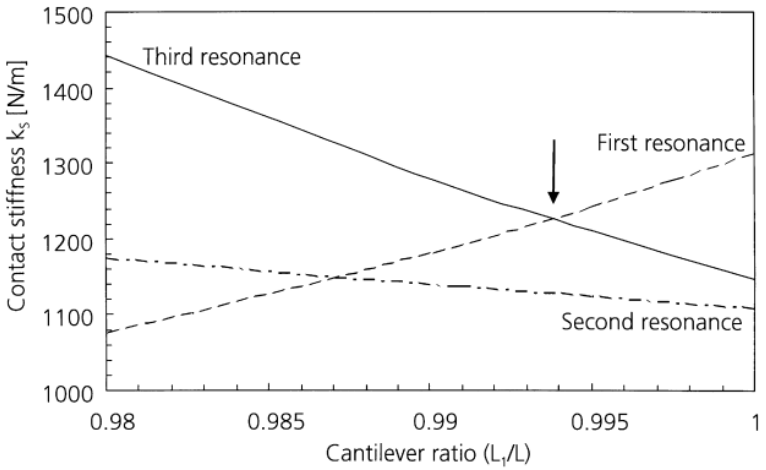

Figure 2.15: Influence of the tip position on the calculated contact stiffness [81]

Prasad et al. [20] have studied the elastic properties of soft materials. Clay minerals, which are integral part of many clay bearing formations, were investigated. Thin layers of kaolinite and dickite samples prepared by specific methods were taken for measurements. The obtained results were correlated with the standard samples (fused silica, mica and polystyrene). Figure 2.16 shows first and second CR spectra obtained on the known and unknown samples. The resonance spectra were found to be broader for low impedance materials, which was attributed to attenuation. Very low loads were utilized to perform the experiments and an error of about 40 % was seen in the measurements. The obtained error in the values were from the theories required to model the cantilever vibration mode and the tip sample interaction radius. It was reported that, the error may

be reduced if the elastic constants of the calibration sample were close to that of the sample for test.

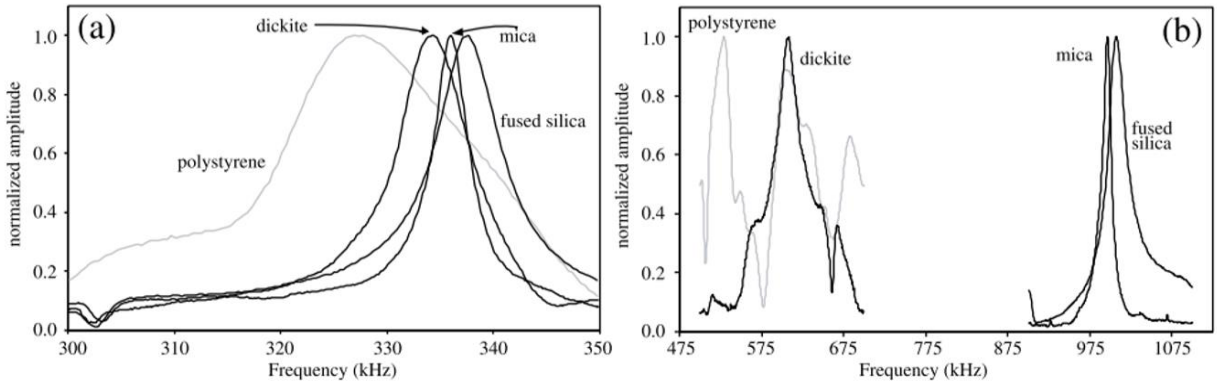

Figure 2.16: (a) First and (b) second contact resonance spectra obtained on polystyrene, dickite, mica and fused silica [20].

Rabe et al. [82] have demonstrated that the contact resonances in the ultrasonic frequency range can also be used to improve the image contrast in other dynamic techniques as, for example, in the so-called piezo-mode. It was possible to set the sample surface into vibration by supplying an alternating electric field between a conducting cantilever and a piezoelectric sample via the inverse piezoelectric effect. Thus making the excitation localized around the contact area formed by the sensor tip and the surface of the sample. The CRFs obtained through piezoelectric effect are found to be higher than the acoustic mode with the same static load and cantilever. This method was applied to see the substructures, domain structures along with the grains in piezo electric ceramics as shown in Figure 2.17. Both dynamic techniques are capable of imaging not only the different grains but also the substructures within the grains due to ferroelectric domains of different polarization.

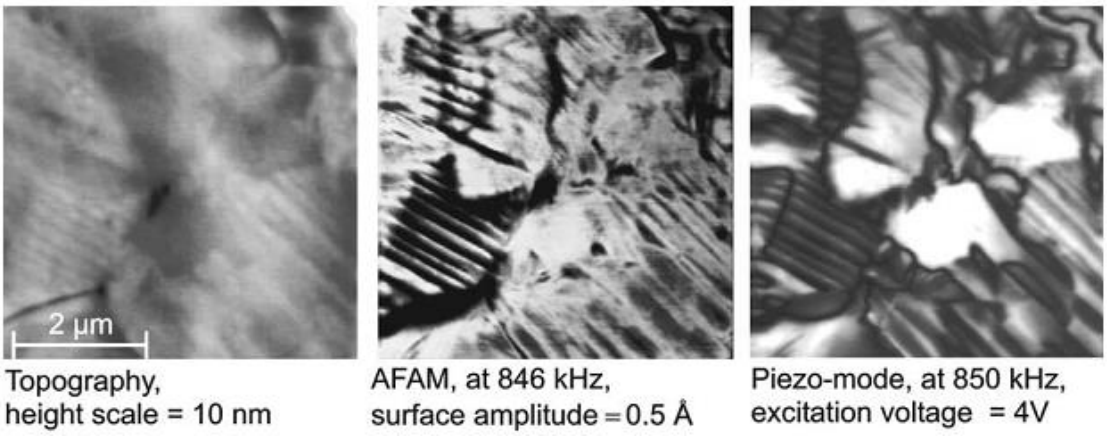

Figure 2.17: Topography, acoustic mode and piezo mode amplitude images of a PZT ceramic surface [82]

Rabe et al. [17] studied the elastic properties of single crystals that constituted PIC 151 ceramic and described a method which can be applied to multiphase materials. The study was carried out on two single crystals (Si (100) and Si (111)) and lead-zirconate titanate (PZT) ceramics by performing point measurements. Repeated measurements were performed on the two single crystals using similar cantilever for different static forces. Reproducible difference was seen even after the tip shape unstability. Si (111) exhibited higher stiffness than Si (100). Due to homogeneity in the single crystals, there was no change in the contact resonance frequency as a function of measurement location. But it was not the case for the piezoelectric ceramic (PIC). Amplitude (acoustic) images were obtained for the PIC and found that the lamellar patterns exhibiting areas with black and white stripes were apparent to be 90 deg domains in a ferroelectric material with tetragonal crystal lattice. The possible errors in the quantitative values obtained were attributed to the tip wear while scanning. An error of 20 % in the reduced modulus, E^* was observed when the elastic constants of the reference sample were close to those of the unknown sample.

In the same year, Rabe et al. [83] extended her work on the high resolution characterization of the piezoelectric ceramics like PZT ceramics (PIC 151) and Barium titanate ($BaTiO_3$) using AFAM and ultrasonic piezoelectric force microscopy (UPFM). The contrast mechanism of both techniques were discussed. They found that a silicon tip of (001) orientation and having rotational symmetry does not disturb the rotational symmetry of contact. The contrast of piezo mode images was found to be dominated by piezoelectric effect, which is much smaller than the influence of local tip sample contact stiffness. Similar type of work was continued on nanocrystalline piezoelectric ceramics by Kopycinska et al. [84]. The influence of the annealing conditions on lead calcium titanate (PTC) properties was studied. Study was carried out by both AFAM and Piezo mode. Combination of these two techniques would allow more clear interpretation of obtained images and identification of different phases in a material. Hurley et al. [85] have studied the elastic properties of Nb thin films. Two different cantilever geometries and two separate reference materials were used for the study. Data analysis was carried out by two methods: an analytical model based on conventional beam dynamics, and a finite element method that accommodated variable cantilever cross section and viscous damping. They have found that the rectangular cantilever are 2.5 times stiffer than the dagger shaped cantilevers. For cantilevers with non-uniform cross section, it was necessary to include the effect of viscoelastic damping in finite element method (FEM) analysis and they believed that FEM approach should be applied to cantilevers with distinctly non rectangular shapes.

Caron et al. [86] have used lateral bending modes to image shear stiffness and friction in 3Y-TZP stabilized zirconia sample. By proper insonification of ultrasonic shear waves into the sample which causes in-plane surface displacements, torsional resonances of the AFM cantilevers were excited, offering to study the shear and friction properties of the sample. A lateral mode is an in-plane flexural mode vibrating parallel to the width of the sample. The lateral cantilever modes exhibit vertical deflection amplitudes if the cantilever is asymmetric in thickness direction, e.g.,

by a trapezoidal cross section. The paper explains the importance of the in –plane deflection of standard cantilevers, which is not negligible.

Hurley et al. [87] studied the effect of humidity on the AFAM modulus measurements. For this, two materials were considered for the study: a thin film of flurosilicate glass (FSG) and a piece of pyrex 7740 borosilicate glass. Figure 2.18 shows the effect of relative humidity on the modulus of fluorosilicate measured using AFAM. Black filled circles in the image indicate values calculated using mechanical model excluding damping and boxes indicate values obtained after model with consideration of damping. Without considering damping, i.e. assuming elastic effects only, the contact stiffness were found to increase linearly with humidity. Extension of mechanical model including a damping term was proposed and the damping term was found to be proportional to the relative humidity. Contact stiffness values calculated using the extended model did not show any dependence on humidity. Hence, M values were similar regardless of the humidity level. It is found that, the environmental conditions may have effect on the AFAM measurements atleast for some materials (FSGs).

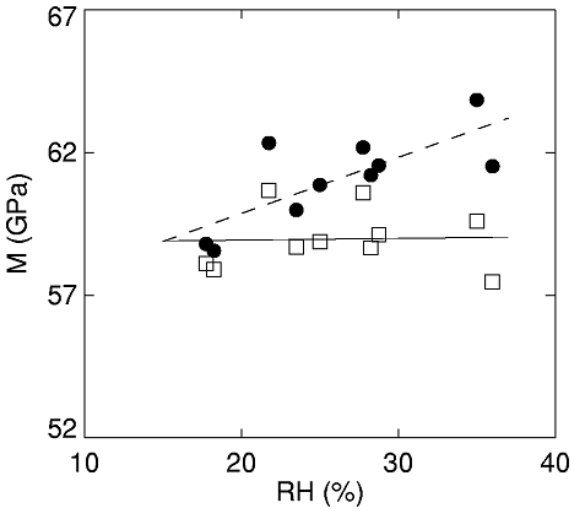

Figure 2.18: Effect of relative humidity on measurement of modulus of fluorosilicate glass by AFAM. Circles and boxes indicate the M values calculated by neglecting and considering the damping effects, respectively [87]

Hurley et al. [88] discussed in detail the design and use of electronics in tracking contact resonance frequencies. Authors explained a faster way of data acquisition (frequency tracking electronics) for quantitative imaging of nanoscale properties. The procedure was demonstrated on Nb film which was sputtered on top of a blanket film of silica (SiO_2). Various thin films like niobium, nickel, aluminum, hydrogenated silica on carbide (SIC:H) and fluorosilicate glass were studied by using AFAM and nanoindentation (NI) techniques. The results obtained were found to be similar in both the techniques. Figure 2.19 shows the CRF maps along with the derived k^* and M maps obtained on Nb/SiO_2. It is clear from the figure that Nb film shown higher 1^{st} and 2^{nd} contact resonance frequencies SiO_2. The first and second CRF maps were used to obtain the k^* map. The k^* map was converted to modulus values using a reference measurements on fused silica. Wear studies of the tip before and after the experiment were carried out using SEM. The tip damage is inevitable and R can change significantly. Slight tip wear across the scan can be seen in the Figure 2.19. Knowledge of R and how it changes would allow to have accurate measurements of elastic properties with AFAM and other contact AFM methods. Imaging with two contact resonance frequencies during the same scan would greatly reduce the effects and drift and wear effect. This is one of the major objectives of this thesis and it is dealt with more details in later chapters. The method suggested by Hurley et al. [88] was successfully demonstrated on glass-fiber polymer matrix composite by Kopycinska et al. [89]. Along with the flexural modes, the method was used on torsional modes as well. Contact stiffness maps provide the visualization of relative elastic property, but the elastic modulus maps were the ultimate goal. The first and second CRF maps, k^* map and modulus map obtained on glass-fiber polymer matrix composite are shown in Figure 2.20.

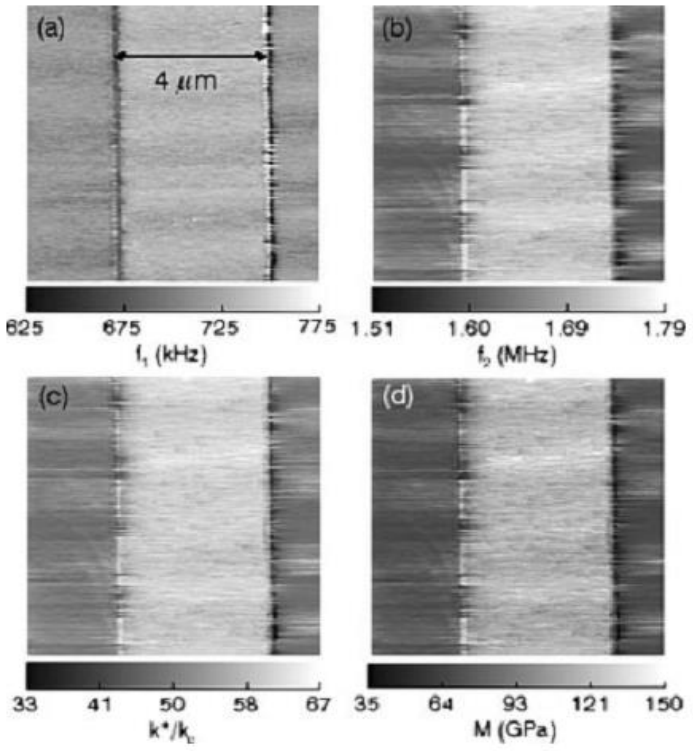

Figure 2.19: CRF maps of the (a) first and (b) second modes, (c) contact stiffness map and (d) indentation modulus (M) map of Nb/SiO_2 thin film sample [88]

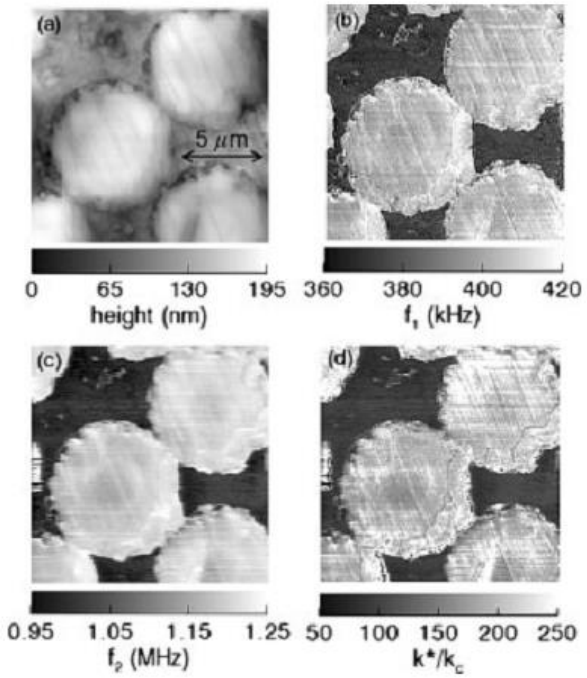

Figure 2.20: (a) Topography, (b) and (c) CRF maps and (d) contact stiffness map of glass fiber polymer matrix composite [89]

Kassavetis et al. [90] have studied the surface morphology and mechanical properties of hydrogenated amorphous carbon thin films, a-C:H deposited on Si (001) substrates by RF reactive magnetron sputtering. Study was performed by using both AFAM and NI. The elastic modulus of the film (E_f) calculated using the two techniques were compared. Effect of surface bias voltage was observed on roughness, hardness and elastic modulus of the deposited film. Figure 2.21 depicts the effect of surface bias on the elastic modulus and hardness. Special fitting procedures were implied to separate the mechanical properties of the films from the substrate influence. The film grown at bias voltage V_b = -40 V was used as a reference sample. They found that the values appeared to be higher in case of AFAM as compared to NI. This was attributed to the difference in force in the two techniques (μN in case of NI and nN in case of AFAM). Figure 2.22 shows the results obtained by the two techniques. AFAM results show higher modulus values as compared to the NI.

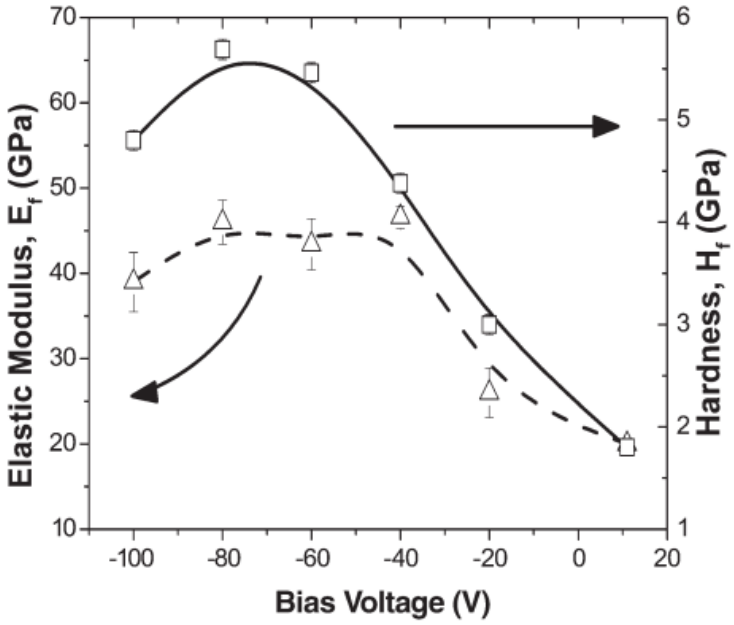

Figure 2.21: Effect of surface bias on elastic modulus and hardness [90]

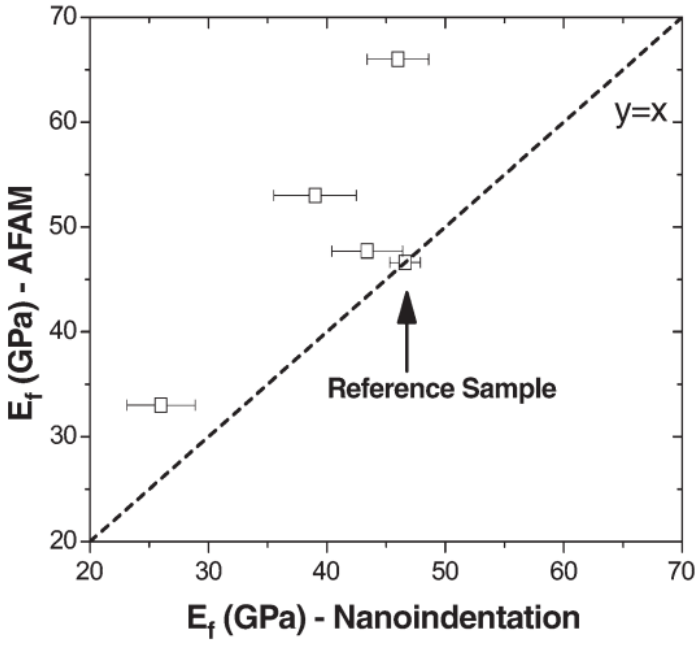

Figure 2.22: Elastic modulus of the a-C:H measured using the AFAM and NI [90]

Kumar et al. [15] have determined for the first time the isotropic indentation modulus of precipitates in polycrystalline materials by using matrix as a reference. Using matrix as a reference, helps in circumventing the practical difficulty of repeatedly switching between a sample and a reference during measurement of indentation modulus using AFAM. In the case of polycrystalline materials, it is important to understand the effect of crystallographic orientation of the grains on the indentation modulus measured using AFAM. The variation in the isotropic indentation modulus (M_{iso}) (calculated by using average Young's modulus and Poisson's ratio) of bulk polycrystalline samples with anisotropic indentation modulus (M_{aniso}) in individual planes are shown in Figure 2.23 for various metals and alloys with cubic crystal structure. The anisotropic indentation modulus is found to be minimum in orientation (100) followed by (110) and (111) orientations. The anisotropic indentation modulus in (110) orientation is found to be almost similar to the isotropic indentation modulus. Since, there is no much variation between the anisotropic and isotropic indentation modulus values, thus, it does not require the orientation of the grain and of the precipitates to be known and M_{iso} of the matrix can be used as a reference to find the M_{iso} of

the precipitate irrespective of the matrix orientation. The maximum variation in M_{aniso} in different planes for materials with high elastic anisotropies was found to be about 7% of M_{iso} (Figure 2.23 (b)). Further, based on the orientation relationship between the precipitate and the matrix, it was postulated that for most of the systems the error could be < 2%. The described methodology has been demonstrated for measurement of M_{iso} of $M_{23}C_6$ carbides in alloy 625 and a ferritic steel as is shown in Figures 2.23 (c) and (d).

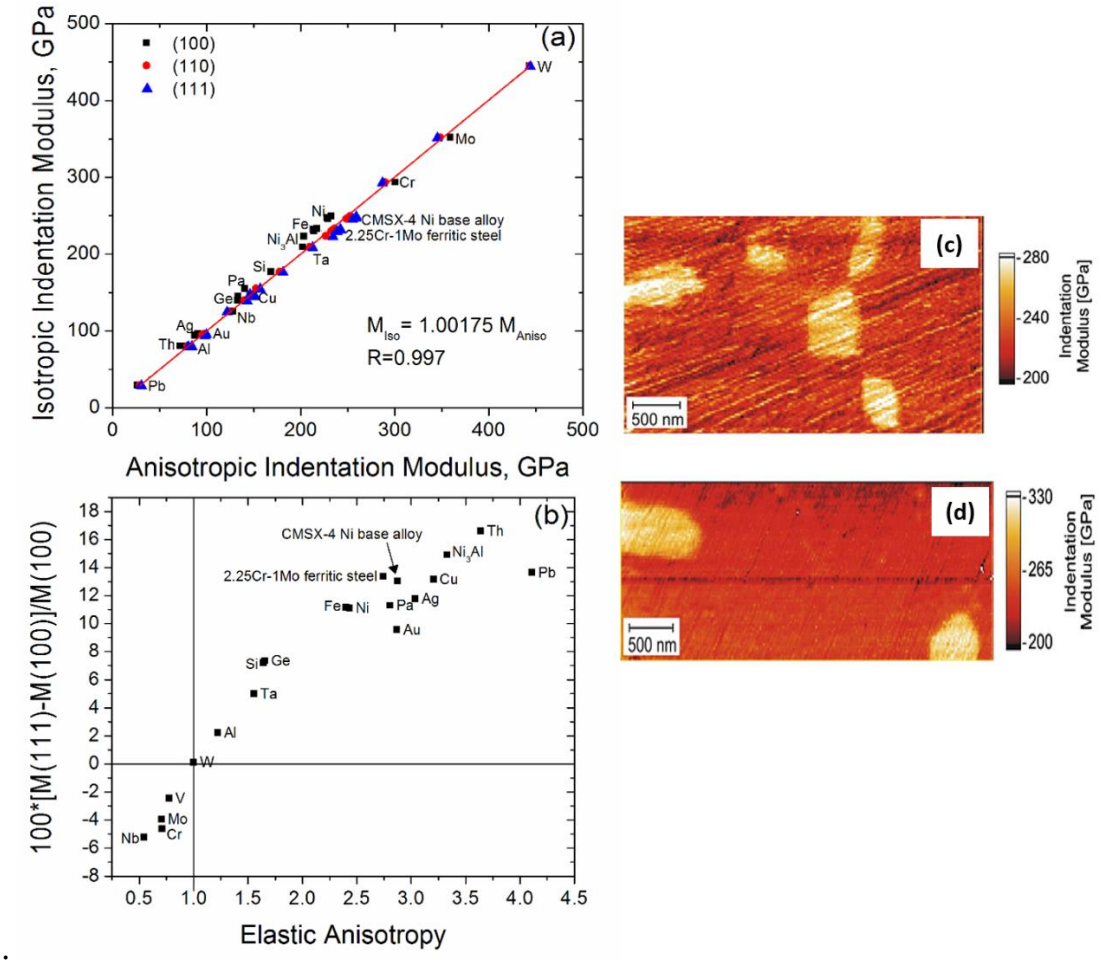

Figure 2.23: a) Correlation between isotropic and anisotropic indentation modulus, b) percentage variation in the difference in the extreme values of M_{ansio} with the elastic anisotropy of various materials of cubic geometry. Distribution of isotropic indentation modulus in (c) alloy 625 and (d) modified 9Cr-1Mo ferritic steel [15]

Elastic stiffness distribution studies were also carried out on an (α+β) titanium alloy – Ti-6Al-4V using AFAM [14]. They found that the minimum modulus was exhibited by β followed by α′ and α phases.

AFAM has also been used extensively to study ultra-thin films [91-93], polycrystalline and nanocrystalline nickel [94], nanobelts [95], diamond like carbons [96], epoxy-silica nanocomposites [97], tellurium nanowires [98], nanotubes [99], cement paste [100], nanoporous silica [101], metallic glass [13] and properties like Poisson's ratio [102] and adhesion [103]. Various parameters used in AFAM and their effect on calculation of local indentation modulus of materials has also been studied exclusively [70, 104]. FEM studies have been performed to understand the tip sample contact mechanics [105, 106]. Apart from these, AFAM has also proven promising in studying surface cracks [107] and subsurface defects [108, 109].

2.5.4. Simultaneous measurements of elastic and damping properties using AFAM

Mapping of damping at nanoscale was performed, for the first time by Yamanaka et al. [110] in 2001 using an improved UAFM. The maps were performed on carbon fibers and epoxy resin in a CFRP. No work was carried out in AFAM considering the mechanical model including damping until 2008. Later, Yuya et al. [10] implemented it in AFAM by modifying the cantilever dynamics model. After this, a lot of studies were carried out towards the mapping of damping. We will discuss in glimpse the application of this model on to various materials.

Yuya et al. [10] proposed a new quantitative method for measuring viscoelastic properties which is based on the AFAM approach originally developed for measurement of elastic properties of materials. He considered a cantilever to be parallel to the surface (0 deg) and included a dashpot parallel to the spring which allowed to determine viscoelastic properties with nanoscale resolution. By including a complex quantity in the characteristic equation, it allowed one to calculate the local

damping along with the local stiffness. The wave number in the characteristic equation was also considered as a complex quantity $\lambda_n L_1 = (a_n + ib_n)$. The characteristic equation can be solved and stiffness and damping can be measured once these a_n and b_n values are found. By using nonlinear least square fits of the amplitude spectra of the free vibration and cantilever in contact, one can obtain a_n and b_n values. To study the damping behavior, the damping due to beam should also be considered. It should be noted that, damping measured, when in contact is the combined effect of beam and the sample. By using measurements on a reference sample, the storage and loss modulus was obtained. The mass of the conical tip was neglected and the tip was assumed to be at the very far end ($L'=0$). The proposed method was demonstrated to study the loss and storage modulus of two polymers, Polystyrene (PS) and Polymethylmethacrylate (PMMA). The obtained values were cross checked with the literature values.

Caron et al. [24] have used the proposed method of Yuya et al. [10] to investigate the onset of plasticity in nanocrystalline (nc) nickel. Nanocrystalline materials exhibit physical and mechanical properties which are different from their polycrystalline counterparts and are attributed to their high grain boundary volume. Nucleation of dislocation was studied on nc-nickel with different grain sizes. The dynamic behavior was studied using AFAM. Both the tip and the material under study contribute to the reduced elastic and reduced anelastic properties. Point mass model was used and the cantilever was considered to be non-parallel to the surface. In spectroscopic mode, contact stiffness k^* and contact damping Q^{-1} vs load curves were obtained for various grain sizes of nc-nickel. They observed a decrease in contact stiffness and increase in contact damping with load which was attributed to the nucleation of the heterogeneous partial dislocation at grain boundaries and internal friction of the moving dislocation in the elastic oscillatory field of the AFM cantilever-tip. The contributions for the contact damping are internal friction due to anelastic dislocation movement in oscillatory field of tip or because of the energy

lost in generating the dislocation. The study would also help to understanding ultrasonic absorption in materials of complicated microstructures like steels and fatigues materials.

Caron et al. [22] also studied the contribution of friction to the contact damping in AFAM. Point measurements were performed on nc aluminum (nc-Al) and quartz glass. Contact resonance curves against increase in load were obtained and local stiffness and damping were determined. Contact damping was found to have a power dependence on load and they attributed it to micro-sliding of the sensor tip on the sample as described by Mindlin for macroscopic contacts [40]. An expression for finding the dissipated energy per cycle has been introduced. Friction coefficient was also determined from the dissipated energy per cycle in the contact area.

Gannepalli et al. [48] reported a technique called DART (Dual AC resonance tracking) that simultaneously quantifies the contact stiffness and dissipation of an AFM cantilever when in contact with the sample. Amplitude and phase at two different frequencies on either side of the contact resonance are recorded. From these two amplitudes and two phases, it allows to calculate four model parameters by modelling the tip sample contact as a driven damped harmonic oscillator. The four parameters are drive amplitude, drive phase, resonance frequency and quality factor by which one can study the nanomechanical local sample properties. Since the measurement is acquired at a particular frequency, the acquisition times are much lower.

After believing the fact that, the properties of the sample are convolved with the dynamics of the AFM cantilever beam, Yuya et al. [111] extended the study of the relation between the imaginary part of contact stiffness and the Q-value of the cantilever for the particular mode employed. This relation is not straight forward, in the case of viscous force transmitted to the cantilever viz. the dashpot representing the damping of the materials will lead to stiffening of contact with increasing the contact damping. So, there is an interdependence between the Q-value of the cantilever

measured, the k^* and also the local damping γ^* which will depend on the mode employed. The damping here can then be related to physical mechanism occurring at the contact [24]. The method was employed later by Killgore et al. [112] to study the local damping distribution or the loss modulus E'' in a polymer blend. The relative storage and loss modulus maps of the Polystyrene-Polypropylene blend is shown in Figure 2.24. More details of the equations used are provided by Maev [71].

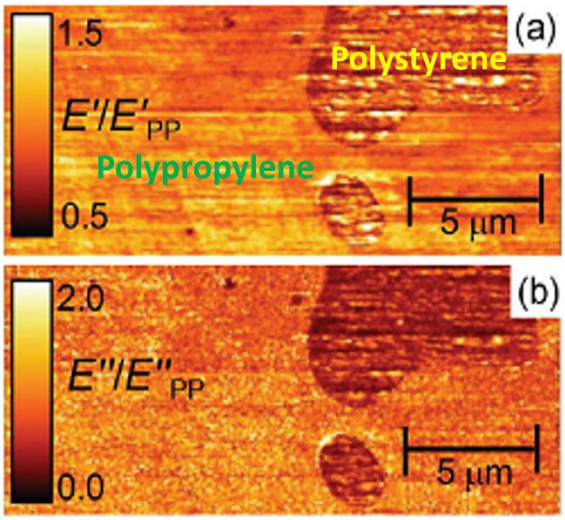

Figure 2.24: Viscoelastic mapping of relative modulus (a) E'_{PS}/E'_{PP} and (b) E''_{PS}/E''_{PP} using DART contact scanning approach [112]

Killgore et al. [113] extended his work on studying the frequency response and its Q factor for nanomechanical measurements. He introduced a hybrid technique (pulsed contact resonance) for improved quantitative nanomechanical measurements. This method uses a multifrequency technique to calculate the CRF and its Q factor during the repulsive contact segment of the pulsed contact cycle. Unlike the CRFM measurements, where a complete resonance spectra is acquired, the cantilever is driven in fixed or variable frequencies which actually reduces the acquisition times. This method was demonstrated on an experimental sample which consisted of epoxy and silicon. Cantilever deflection, vibration amplitude and phases were acquired by cycling the position of the z-piezo. This technique is readily applicable to peak force tapping and add benefits

for piezo response force spectroscopy, where contact resonance methods are used to increase sensitivity to piezo displacements and provide dissipation information.

Stan et al. [114] mapped the contact stiffness and damping with nano scale resolution in copper inter-connects and low k dielectric materials. This was achieved by utilizing the method of resonance tracking in UAFM mode suggested by Kobayakshi et al. [115]. CRFs and their amplitudes were recorded. It was found that the CRFs are fully dependent on elastic modulus, but the amplitude of the resonance depends on both the elastic modulus and contact damping. Damping showed a depth dependence and decays with increase in depth.

Luo et al. [116] studied the nanoscale elastic properties of twinned martensite films of NiMnGa alloys using AFAM. Modulus maps were obtained to demonstrate variations in local moduli due to the mobility of twin boundaries (TBs) and /or the crystallographic anisotropy of twin variants. Correlation between the k^* and Q^{-1} was observed, relating it to the TB movement to be dissipative accompanied by viscoelastic behavior. Martensitic multivariants which led to the observation of multiresonance spectra, likely concerning invisible 90 deg-twinned nanotwins. Static load-dependence measurements were carried out and a critical stress defined as the start of softening in the contact zone due to the TB motion was also determined.

Stan et al. [117] analyzed in detail the resonance frequency, amplitude, and phase of the first two eigen modes of two contact resonance AFM (CR-AFM) configurations, namely a setup with sample stage excitation (AFAM) and one with cantilever base excitation (UAFM). It was found that AFAM phase is very sensitive to both contact stiffness and damping. So, for phase control detection applications, UAFM would be preferred.

Wagner et al. [25] studied the local internal friction in metallic glasses. They introduced a modified CDM which was not based on point mass but on distributed mass with damped flexural modes. They studied the local contact damping (Q^{-1}_{loc}) of amorphous PdCuSi metallic glass and its crystalline counterpart as a function of position of the tip on the surface. They introduced a complex wave vector which accounted for damping and this complex wave vector was related to complex contact stiffness via dispersion curve. They also studied the resonance curve as a function of distance from the surface to study the dependence of width of the resonance curve on the tip-sample distance. They found no dependence on the width of resonance curve for the stiff cantilevers, but found ~15% effect with the softer ones. Damping due to internal friction of the cantilever can be neglected as it was found to be very small.

2.5.5. Influence of tip wear and its influence on AFAM measurements

Stiffness-load curves obtained in quantitative AFAM measurements depend on the tip properties also, in addition to the elastic properties of the sample [118]. Tip wear and its corresponding change in geometry is a major impediment for quantifying AFAM [119]. So, there is a need to understand the process of tip wear and its influence on the AFAM measurements. During AFAM measurements on a given sample, contact stiffness increases with increase in tip radius. Changes in the tip radius can been monitored through the measurement of the contact resonances frequencies.

Kopycinska et al. [118] studied the influence of tip wear by including models which considers adhesion forces, F_{ad}, acting within the contact area. In AFAM measurements, adhesion forces are generally less than 10% for the smallest applied static load i.e. 300 - 500 nN), and are therefore neglected. The authors calculated k^* using Hertz, DMT and JKR models for a set of AFAM parameters. They found an increase in k^* with inclusion in adhesion forces compared to the value obtained from Hertzian model for loads < 150 nN. For F_c>3 F_{ad}, k^*_{DMT} was always greater than

k^*_H by < 10 % and decreased rapidly to < 2% greater with increasing F_c. This indicates that for measurements on metallic materials with stiff cantilevers, where $F_c \geq 1000$ nN (used in the present study), Hertz model can be efficiently used.

Recently, Killgore et. al [120] measured the tip wear in real time (i.e. during scanning). By measuring the changes in the contact resonance frequencies and relating them to changes in contact radius, tip changes can be observed in real time during scanning. Here, they used a dual AC resonance tracking (DART) technique as it provides high frequency resolutions for small driven amplitudes. By tracking the changes in f_n^c during scanning, one can find the changes in a. Continuous measurement of tip wear was then demonstrated for stiff and compliance cantilevers. Figures 2.25 and 2.26 show in-situ and ex-situ measurements obtained using stiff and compliance materials. In Figure 2.25, data were acquired by tracking the first contact eigen mode frequency. Data were acquired for the new tip and with application of load to wear the tip. Panels (b–e) are SEM images of the new tip (b) and also used tips (c-e). Change in contact radius with scanned distance for a compliance cantilever observed by tracking its fourth contact eigen mode frequency is shown in Figure 2.26. Regions I through V designate specific tip shape and tip-wear behavior. The inset shows a magnified view of region I. Δ TR is the calculated difference in contact radius between the trace and retrace scan directions. α indicates a rapid change in a, attributed to tip breakage.

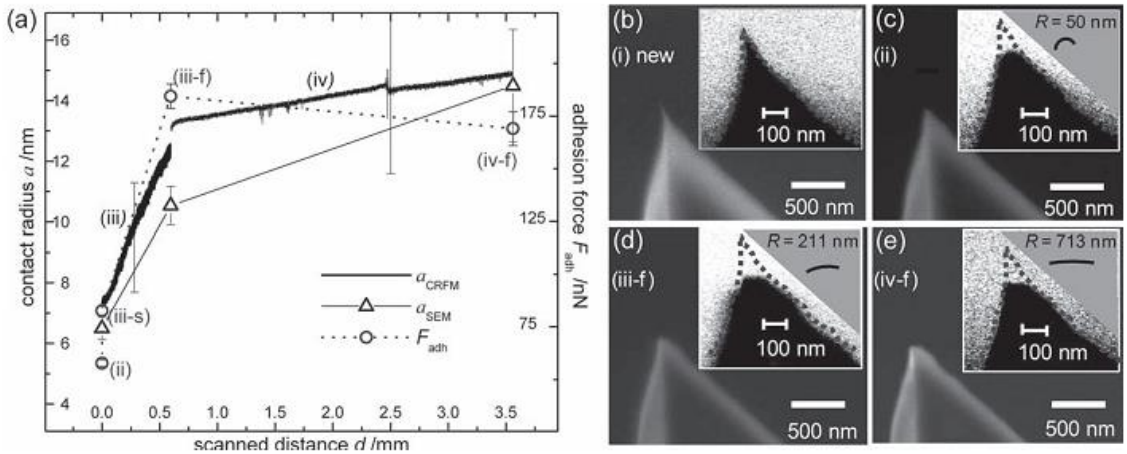

Figure 2.25: Combined in-situ and ex-situ tip wear data acquired for a stiff rectangular Si cantilever (k_c = 48 N/m) on a Si <100 >substrate [120]

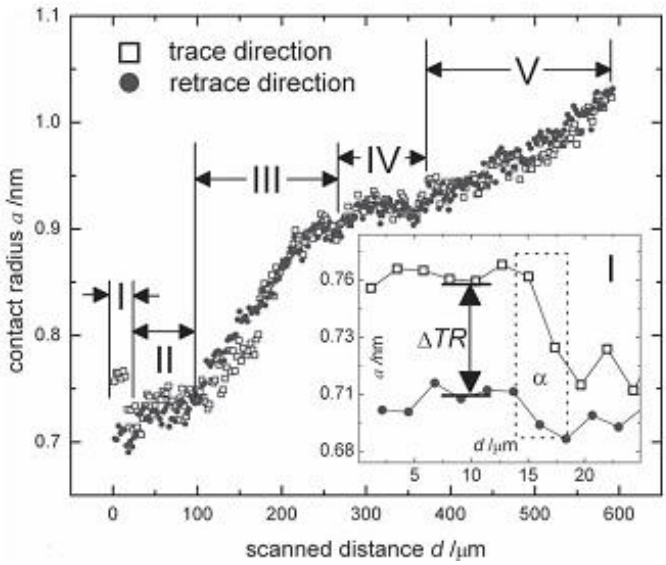

Figure 2.26: Contact radius, *a* versus scanned distance *d* obtained using a compliance cantilever (k_c = 0.11 N/m) [120]

In AFAM measurements, the tip condition often changes continuously/abruptly during scanning. By measuring the CRFs and relating those to contact radius would help in live monitoring of the tip while scanning. Ex-situ measurements using SEM can be eliminated. However, accurate measurement of the tip radius would reduce the error and help in acquiring precise quantitative nanomechanical property values for various materials.

2.6. METALLURGY OF THE MATERIALS STUDIED IN THIS THESIS

Elastic properties of two main classes of multiphase structural alloys viz. nickel and titanium base alloys are studied in the thesis. The physical metallurgy of the alloys are discussed in brief in the following sections.

2.6.1. Nickel base superalloys

Rapid advancement in technology throws a keen interest in material development with good strength and life span. Materials with super properties have to be developed. Super properties include good creep, fatigue, oxidation and corrosion resistance and retaining strengths at high temperatures. Superalloys, as a class, constitute the currently reigning aristocrats of the metallurgical world. Although, there are a number of other materials which can be used at high temperatures such as ceramics and refractory metal alloys. Superalloys are ahead in terms of the combination of high temperature, mechanical properties and environmental resistance. Refractory metals which can retain their strength at high temperatures are poor oxidants. There are many types of superalloys, among them nickel based superalloys find wide spread applications in critical components and environments. They can retain their high strengths at high temperatures during service. They have service temperatures often higher than 0.7 T_m (i.e. around 1255 K) where, T_m is the absolute melting point.

Two types of nickel base superalloys are widely used, polycrystalline superalloys and directionally solidified superalloys. Polycrystalline superalloys have applications from intermediate temperatures to high temperatures, whereas, directionally solidified superalloys are meant for high temperature applications, where creep is of utmost concern. A polycrystalline superalloy, alloy 625 and a directionally solidified super alloy, CM 247A are studied in the present thesis. The physical metallurgy of these two alloys are discussed in the following sections.

Alloy 625

Alloy 625 is a very well-known alloy in the nickel base superalloy category. It has a history dated back to 1950s [121]. The plan of developing an alloy for service in critical steam applications has evolved a material that is today used in wide range of applications and even became a seed for the development of the successful age-hardened alloy ever developed, the alloy 718 [121]. It has wide spread applications in various industries and environments. Eiselstein et al. [121] have studied the effect of various alloying elements on the properties of the alloy and also described its derivatives. The microstructural development at various heat treatments have been well established and well-studied. Chemical composition of the alloy 625 used in the present study is mentioned in Table 2.5:

Table 2.5: Chemical composition (in Wt %) of Alloy 625 [29]

Element	Ni	Cr	Fe	Nb	Mo	Mn+Si	Ti	Co	Al	C
Wt (%)	Bal.	21.73	3.92	3.90	8.82	0.29	0.23	0.08	0.17	0.05

Alloy 625 exhibits properties like high strength at elevated temperatures, excellent fabricability, resistance to creep deformation, oxidation, corrosion resistance and hydrogen attack on prolonged exposures in aggressive environments. The alloy was developed to be used in its solution annealed condition. On prolonged aging heat treatment at temperatures around 823 K to 1023 K, precipitation of intermetallic phases and carbides takes place. In most of the nickel base superalloys, γ' is the strengthening phase whereas in alloy 625, γ'' ($Ni_3(Nb, Mo, Al)$) is the major contributor for strengthening. Under prolonged aging, the metastable γ'' phase converts to δ (needle shape) precipitate which has an orthorhombic (DO_a) structure [122]. Aging at high temperatures leads to precipitation of δ phase directly from the supersaturated solid solution [29]. Sundararaman et al. [122] studied the morphology and the distribution of precipitates in two nickel base superalloys (IN718 and IN625) and also studied the crystallographic orientation relationship between the γ and the δ phases. The orientation relationship is expected as

$\{111\}_\gamma \| (010)_\delta; \langle 1\bar{1}0\rangle_\gamma \| [100]_\delta$ [122]. From this relationship, it is implied that a δ precipitate could form with its (010) plane along any one of the four {111} planes of the γ matrix and that the vector $[100]_\delta$ could be aligned along any one of the three $\langle 1\bar{1}0\rangle_\gamma$ vectors. So, over-all twelve possible orientation variants of δ precipitates would, therefore be anticipated. Carbides form at higher temperatures (1033 K to 1253 K). Extensive studies were also carried out on microstructural evolution and its effects on the mechanical properties of alloy 625 [123, 124]. Figure 2.27 shows the precipitation of various intermetallics and carbide phases marked in a TTT diagram of alloy 625.

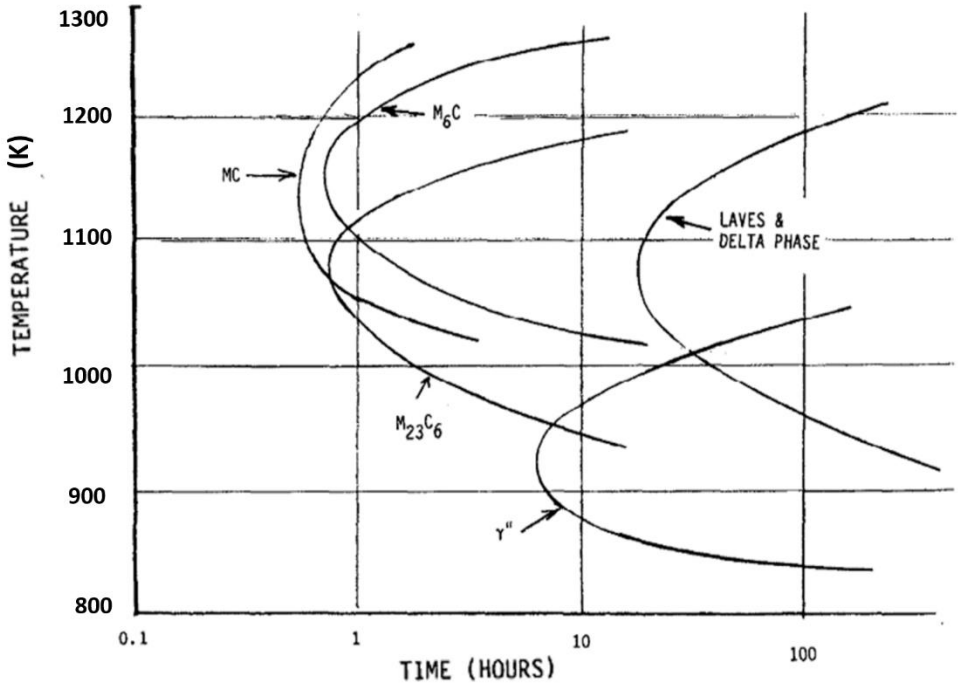

Figure 2.27: Time, temperature and transformation (TTT) diagram of alloy 625 showing the various intermetallics and carbides present at different temperatures [125]

Alloy 625 is used as cracker tubes in the ammonia cracker unit at heavy water plants [126]. Cracking of ammonia to synthesize gas takes place at a temperature of 873 K in presence of a catalyst. The cracker tubes are designed for a life of 1,00,000 hours. Alloy was exposed to 873 K for a prolonged period during service which led to formation of various precipitates leading to

reduction in ductility and toughness. A detailed study has been performed to characterize the precipitates present in the service exposed alloy and to understand their influence on the mechanical properties of the alloy [126]. The influence of post service heat treatments on microstructural modifications and mechanical properties were also studied [126-128]. Giving a re-solutionizing treatment at 1323 K to the service exposed alloy dissolves all the precipitates and regains the lost ductility. Heat treatment at intermediate temperatures (923 K – 1123 K) dissolved different intermetallic precipitates formed during service to different extent.

Ultrasonic velocity measurements were carried out on both service exposed alloy and the alloy with post service heat treatments [29]. Besides microstructural variations, not much quantitative data is available on the mechanical properties of the individual phases present in alloy 625. Recently, for the first time ever, AFAM was successfully exploited to quantitatively map the indentation modulus of the $M_{23}C_6$ type carbides in an alloy 625 service exposed to 60,000 h at 873 K and post service heat treated at 1123 K to dissolve the intermetallic precipitates, without dissolving the grain boundary carbides precipitated during the service exposure [15].

CM 247A

Nickel base superalloys used in modern gas turbines are continuously being developed to increase thrust, operating efficiency and durability. For many years, nickel base superalloys have been used in gas turbines as blades at high temperature because of their excellent high temperature mechanical properties [129]. Single crystal (SX) superalloys and casting technology offer a combination of attractive properties for advanced gas turbine engine components. The alloys are designed to produce superior properties for a challenging combination of requirements: high temperature creep-strength, fatigue resistance, oxidation resistance, coating performance and retention of performance in thin-walled configurations [130]. To have improved thermal fatigue capability, rupture life and ductility, directional structures are ahead of equiaxed structures [131].

Directional solidification (DS) leads to enhancement in the mechanical properties while in service, as they achieve the property by suppressing the transverse grain boundaries which are usually weaker portions [131]. In DS processing, columnar grains are formed parallel to the growth axis. In nickel base superalloys, the natural growth direction is along the <100> crystallographic direction. This morphology is accomplished by pouring liquid metal into a mold that contains a water-cooled bottom plate. Solidification first occurs at the bottom plate, after which the mold is slowly withdrawn from the furnace, allowing the metal inside to directionally solidify from bottom to top.

The exceptional properties of DS and SX alloys are due to [132]:

- The alignment or elimination of any weak grain boundaries oriented transverse to the eventual loading direction.
- The low modulus associated with the <100> directions enhances thermo-mechanical fatigue resistance in areas of constrained thermal expansion—particularly turbine vanes. In general, the lack of transverse grain boundaries coupled with the low modulus can result in 3-5 times improvement in rupture life.

CM 247A is an aeronautical grade advanced nickel base superalloy. It is equivalent to CM 247 LC and is developed by M/s MIDHANI in remelt stock form with R&D inputs from DMRL, Hyderabad [133]. Composition of the CM 247A alloy used in the present study is given in Table 2.6 [129]. It is developed for high temperature applications such as turbine blades and automotive turbocharger motors. Alloying elements, have different tasks such as increasing the volume fraction of precipitates by entering into the γ′ phase (Al, Ta, Ti) or increasing the carbides (W, Cr, Mo) or increasing the high temperature stability of precipitates (Co). This alloy was developed to have a combination of high mechanical strength and corrosion resistance.

Table 2.6: Chemical composition (in Wt %) of CM 247A [129]

Element	Ni	Cr	Co	C	Mo	Ta	Ti	W	Al	Hf	B	Zr
Wt (%)	Bal.	8.2	9.30	0.074	0.505	3.185	0.81	9.5	5.6	1.51	0.015	0.014

The microstructure of CM 247A consists of γ′ phase distributed in a γ matrix with some carbides. Cuboidal γ′ phase provides good strength and helps to retain strengths at high temperatures. This γ′ phase is an ordered phase and have $L1_2$ crystal structure and is oriented in (100). It generally has 50-50 % of γ and γ′. The hardening due to γ′ phase is influenced by various factors, such as fault energy, coherency strains, volume fractions and particle size. Extremely small γ′ precipitates always occur as spheres. For a given volume of precipitate, a sphere has 1.24 less surface area than a cube, and thus is the preferred shape to minimize surface energy. With a coherent particle, however, the interfacial energy can be minimized by forming cubes and allowing the crystallographic planes of the cubic matrix and precipitate to remain continuous. Thus, as the γ′ grows, the morphology can change from spheres to cubes or plates depending on the value of the matrix/precipitate lattice mismatch. For larger mismatch values, the critical particle size where the change from spheres to cubes (or plates) occurs is reduced [132].

2.6.2. Titanium alloys

Titanium alloys are known for their wide range of applications from spectacle industries to aerospace industries due to their excellent specific strength, modulus, low density, ductility and better intermediate temperature strength [134, 135]. Moreover, due to their excellent corrosion resistance and compatibility with human organs, titanium alloys are also widely used for human implants [136]. Titanium and its alloys exhibit a unique combination of mechanical and physical properties and corrosion resistance which have made them desirable for critical, demanding aerospace, industrial, chemical and energy industry service. They possess high strengths with low density compared to alloy steels. Its corrosion resistance is comparable to platinum. Titanium alloys exhibit a low modulus of elasticity which is roughly half that of steels and nickel alloys. An

important characteristic of titanium- base materials is the reversible transformation of the crystal structure from α (hexagonal close-packed) structure to β (body-centered cubic) structure when the temperatures exceeds β-transus temperature (i.e. 1155.5 K). In titanium, there is a high temperature BCC phase, and a low temperature HCP phase, and the local transformation from α to β or β to α generally is governed by the Burgers relationship (BR) [137, 138]:

$\{101\}_\beta \| (0001)_\alpha$ and $<\bar{1}11>_\beta \| [11\bar{2}0]_\alpha$

Thus, a single parent β can transform into 12 possible orientations of α. This BR closely obeyed for both martensitic as well as the conventional nucleation and growth based phase transformations. The allotropic behavior, which depends on the type and amount of alloy contents, allows complex variations in microstructure and more diverse strengthening opportunities than those of other nonferrous alloys such as copper or aluminum. A detailed description of the properties of titanium alloys can be found in [137, 139].

Titanium alloys are divided into two categories: corrosion resistant (mostly single phase alloys) and structural alloys. There are three structural types of titanium alloys:

a. α

b. $(\alpha + \beta)$ and

c. β

Among these, α and near α alloys exhibits superior corrosion resistance but have limited lower temperature strength, whereas $(\alpha + \beta)$ type alloys possess good strength because of the dual phase. β alloys possess lower elastic modulus amongst all other types (upto 14 GPa) and very good corrosion resistance [140]. The present study in this thesis is carried out on an $(\alpha + \beta)$ titanium and a β titanium alloys.

2.6.2.1. (α + β) Ti alloys

All $(\alpha + \beta)$ titanium alloys can be given heat treatment to obtain a combination of properties. Alloying elements generally stabilize one or the other of these phases. The α phase is

stabilized by aluminum, gallium, germanium, boron, carbon, oxygen and nitrogen, while the β phase is stabilized by molybdenum, vanadium, tantalum, niobium, iron and hydrogen. The α phase can also be strengthened by the addition of tin or zirconium. These metals are normally classified as neutral additions as they have appreciable solubility in both α and β phases and as their addition does not show any influence on the transformation temperature. The addition of controlled amounts of β-stabilizing alloying elements causes some β phase to persist below the β- transus temperature, down to room temperature resulting in a two-phase system. Even small amounts of β stabilizers will stabilize the β phase at room temperature. The solution treatment temperature plays a very important role in deciding the volume fractions of α and β phases and the alloying elements in them. Kumar et al.[141] have introduced a new method using ultrasonic velocity measurements to identify β- transus temperature in (α + β) and β titanium alloys. The mechanical properties of the (α + β) titanium alloys are controlled by the thermomechanical processing history. The deformation temperature, cooling rate and aging times/temperatures defines the overall size, chemistry, morphology and volume fraction of the α and β phases. (α + β) titanium alloys selected for study in the present thesis is Ti-6Al-4V. Phase diagram of (α+β) titanium alloy is shown in Figure 2.28 pointing the β- transus temperature of Ti-6Al-4V.

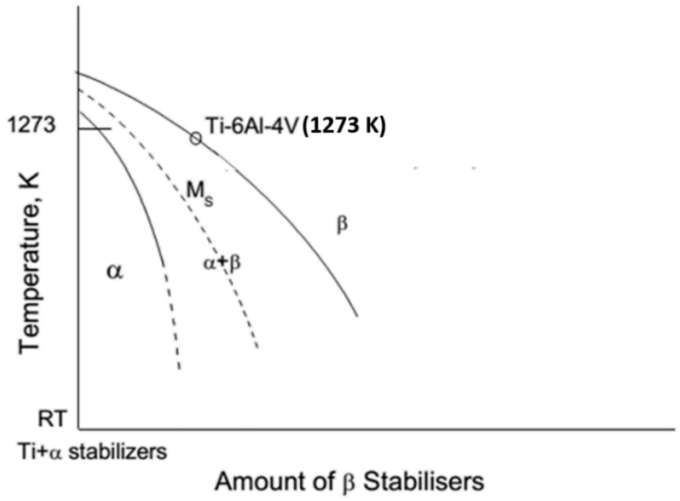

Figure 2.28: Influence of β-stabilizing elements on α and β solidus lines of an (α+β) titanium alloy [29]

Ti-6Al-4V

Ti-6Al4V is one of the most widely used (α + β) titanium alloy. It possesses good machinability and excellent mechanical properties making it reliable for extreme harsh environments. Ti-6Al-4V has the best weldability of all the (α + β) titanium alloys. It is because of two factors: first the α' formed in Ti-6Al-4V is not that hard and brittle as that exhibited by more heavily β stabilized alloys (viz. Ti-6Al-6V-2Sn). Second, it possess low hardenability while cooling from solution heat treatment temperatures. This allows formation of high proportions of α plus retained β phases during cooling [142]. Various studies are reported on microstructural evolution in Ti-6Al-4V [143] and their effect on the mechanical properties [144]. Kumar et al. [29] studied the variation of elastic modulus, shear modulus and Poisson's ratio with heat treatment temperature using ultrasonic measurements on bulk Ti-6Al-4V alloy samples. Figure 2.29 shows the plot showing the variation in elastic modulus, shear modulus and Poisson's ratio as a function of heat treatment temperature. Recently, Kumar et al. [14] has mapped for the first time the elastic properties of the individual phases in a Ti-6Al-4V alloy heat treated at a particular temperature using AFAM in which CDM deserting damping was used.

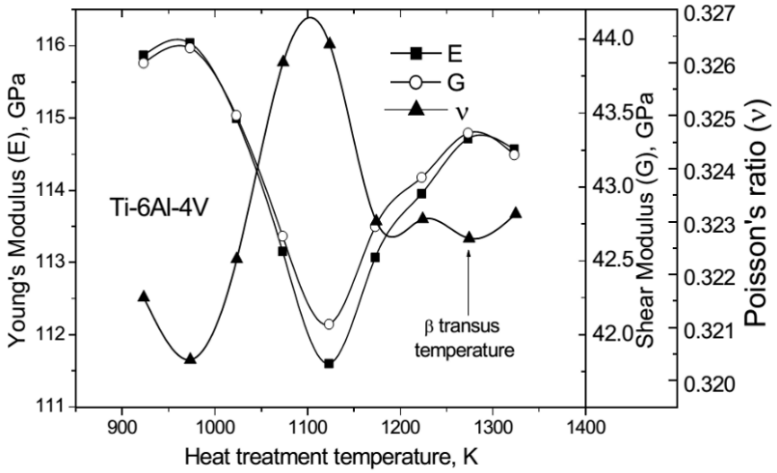

Figure 2.29: Variations in Young's modulus, shear modulus and Poisson's ratio with heat treatment temperature for Ti-6Al-4V [29]

2.6.2.2. β – Ti alloys

β-titanium alloys offer many attractive advantages in terms of processing (formability), good corrosion resistance and mechanical properties such as good combination of strength, toughness and fatigue resistance. Because of high formability characteristics of *β*-titanium alloys, they find various applications in frames for spectacles, orthopedic implants, automotive parts, high strength forgings, casting, springs, fasteners and in landing gears. In *β*-titanium alloys, the controlled amount of the *β* stabilizers are added to the titanium alloys to suppress the martensitic transformation and to retain the BCC *β*-phase at room temperature upon quenching from temperature above the BTT. There are two types of *β*- stabilizers: *β*- isomorphous (Mo, V, Ta and Nb) and β- eutectoid (Cr, Mn, Fe, Si, Co, Ni and Cu). [145] It is reported that the molybdenum equivalent value (the strength of an alloying element in stabilizing the *β*-phase relative to that of the Mo) greater than about 10 % stabilizes the *β*-phase at room temperature upon quenching [146].

The metastable *β*-titanium alloys can be subjected to thermo-mechanical treatments to enhance mechanical properties of the alloys. As the *β*-titanium alloys are heat treatable, the heat treatment temperature and time plays a vital role in deciding the microstructure and mechanical properties of the alloy. When the *β*-titanium alloys are heat treated at a temperature below the BTT, a certain amount of β-phase transforms into *α*-phase depending on the temperature and the hold time duration. The lower the temperature and longer the hold time, the more amount of *β*-phase will transform into α-phase. Hence, by suitably varying the heat treatment temperature and time, it is possible to obtain a good combination of strength, toughness and fatigue resistance in *β*-titanium alloys. Unlike other alloys, the elastic properties of titanium alloys may change as much as 25-30% depending upon the microstructure [146]. In this thesis, study is carried out on Ti-10V-4.5Fe-1.5Al**,** a β- titanium alloy.

Ti-10V-4.5Fe-1.5Al

Low cost beta (LCB) alloys are being developed to possess high strength and low modulus and show potential applications as springs and fasteners in aerospace and automobile industries, and armor components. Ti-10V-4.5Fe-1.5Al alloy is a modified version of Ti–6.8Mo–4.5Fe–1.5Al in which, the Mo content is replaced by V on an equi-molybdenum basis [147]. The chemical composition of the Ti-10V-4.5Fe-1.5Al alloy used in the study is given in Table 2.7. The alloy exhibits lower cost which is comparable to pure titanium [148]. The alloy is fast gaining importance for automotive applications such as rear suspension springs for racing cars as well as some commercial cars and also being used in oil well down hole service, sporting equipment and surgical implants [148].

Table 2.7: Chemical composition of Ti–10V–4.5Fe–1.5Al alloy (wt.%) [146]

Element	Ti	V	Fe	Al	O	N	P
Wt (%)	Bal.	9.68	4.4	4.45	0.1	0.18	0.03

Bhattacharjee et al. [148] studied the mechanical properties and deformation behavior of Ti–6.8Mo–4.5Fe–1.5Al and Ti-10V-4.5Fe-1.5Al alloy in solution treated and aged conditions. Other studies include hot deformation characteristics of Ti-10V-4.5Fe-1.5Al [149, 150]. Luo et al. [151] studied the effect of strains on the processing maps. It was observed that the processing maps are significantly affected with strains. The Mo equivalent value of the alloy calculated based on the chemical composition is found to be ~18%. The β-transus temperature (BTT) of the alloy is reported as 1050 ± 10 K. Viswanath et al. [146] have studied for the first time the effect of microstructural changes occurring in Ti-10V-4.5Fe-1.5Al alloy with heat treatment temperature on various ultrasonic parameters. Study demonstrated quantitative correlation between various ultrasonic parameters and the volume fraction of α/β phases in Ti-10V-4.5Fe-1.5Al alloy specimens heat treated at various temperatures. Elastic randomization of the alloy was observed with the alpha phase precipitation and led to decrease in shear

anisotropy and ultrasonic scattering. The decrease in the ultrasonic attenuation with the precipitation of α-phase is attributed to the decrease in ultrasonic scattering and β-phase volume fraction with higher damping characteristics.

2.7. MOTIVATION

The review of literature reveals the establishment of application of AFAM in determining modulus and damping properties of various materials. AFAM has shown its importance not only in determining the modulus but also to identify the subsurface structures. Damping consideration has revealed many significant application of AFAM and made it more powerful in studying the dissipation properties at scales which were not possible earlier. A lot of development has undergone in CR-AFM techniques and even towards multifrequency techniques to understand the elastic and damping properties of materials with good accuracy and speed.

It is clear however that, there is no systematic study performed on the elastic properties of stiff materials (> 80 GPa) like polycrystalline/multiphase metallic structural alloys at micro/nano scales. The knowledge of the elastic properties of phases/precipitates embedded in these structural alloys has high technological importance. Very few studies are reported on the elastic properties of individual phases in multiphase structural alloys. The study of the elastic properties of the individual phases in these structural alloys would help to understand many deformation mechanisms like crack nucleation and propagation and help in developing materials with much more promising properties and life span. Further, it will also provide elastic properties of individual phases embedded in the matrix which are not available for most of the phases/precipitates.

The resolution of the AFM based techniques come from the tip radius. The problem of tip wear during AFAM measurements is obvious and need to be addressed. It is clear from the literature

that the indentation modulus values obtained in different crystallographic orientations are similar to the isotropic indentation modulus of the polycrystalline sample. Hence, AFAM measurements can be carried out in any grain without much variation in the final modulus values. However, more data on various precipitates in different structural alloys is required. The recent development of the cantilever dynamics model considering damping can be utilized in understanding the damping behavior of the individual phases in the multiphase structural alloys.

2.8. OBJECTIVE

The primary objective of this thesis work is to employ AFAM for quantitative mapping of elastic and damping properties of individual phases/precipitates present in different multiphase structural alloys at submicron/nanoscale with the spatial resolution of 50 nm. To achieve this, the following works have been carried out:

- ✓ Develop an approach for simultaneous acquisition of contact resonance frequencies and thus eliminate the problem of tip wear
- ✓ Understand the effect of various parameters used in AFAM studies to obtain the reliable quantitative values for elastic properties of multiphase materials with improved sensitivity
- ✓ Study the elastic and damping properties of individual phases/precipitates in multiphase structural alloys using AFAM
- ✓ Study the elastic properties of individual precipitates present in a polycrystalline and a directionally solidified nickel base superalloys.
- ✓ Study the elastic and damping properties of individual phases present in titanium base alloys heat treated at different temperatures and durations by applying a suitable cantilever dynamics model including damping
- ✓ Correlation of the data obtained from the AFAM with the data obtained using ultrasonic velocity measurements carried out on bulk samples.

3 EXPERIMENTAL SETUP

3.1. INTRODUCTION

This chapter deals with the experimental setup of AFAM used in the present study. Cantilevers used for the studies are presented. Software developed for acquisition of data from AFAM and processing of data using LabVIEW are also described. Sample preparation procedures for the materials used in the study are discussed.

3.2. AFAM EXPERIMENTAL SETUP

The principle of AFAM is discussed in detail in Chapter 2. Schematic representation of the AFAM setup is shown in Figure 2.8. An NTEGRA AFAM system supplied by M/s. NT-MDT. Co., Zelogonard, Russia was used in the present study. Photographs of the experimental setup is shown in Figure 3.1 (a). NTEGRA system is equipped with a SMENA head (shown in Figure 3.1 (b)) which consists of laser, cantilever and its deflection detection systems. The laser is a class 2R type with the maximum output less than 1 mW and have wavelength of 650 nm. A photodiode with four quadrants is placed inside the head. The signals from the photodiode are sensed by the controller, which is equipped with a lock in amplifier. The processed data by the controller will be then sent to the computer for further processing and analysis. A software named NOVA© is used for performing various operations required to acquire data from the AFAM system. AFAM is equipped with a broad band (5MHz) ultrasonic transducer with the center frequency of 2.25 MHz. Honey was used to couple the sample to the transducer for effective transmittance of ultrasonic energy from the transducer to the sample. The cantilever is actuated by exciting the ultrasonic waves through bottom of the sample using external ultrasonic transducer (setup is shown

in Figure 3.1 (c)). Typically, piezoactuation involves a single frequency (sine wave) excitation from a function generator. Commonly, two kinds of scanning are possible in AFM, i.e., scan by sample or scan by probe. The system used in the present study is of the latter type. As AFAM is one of the modes of AFM, the detection principle of AFAM is same as in AFM. Figure 3.1 (d) shows the cantilevers placed in a cantilever box.

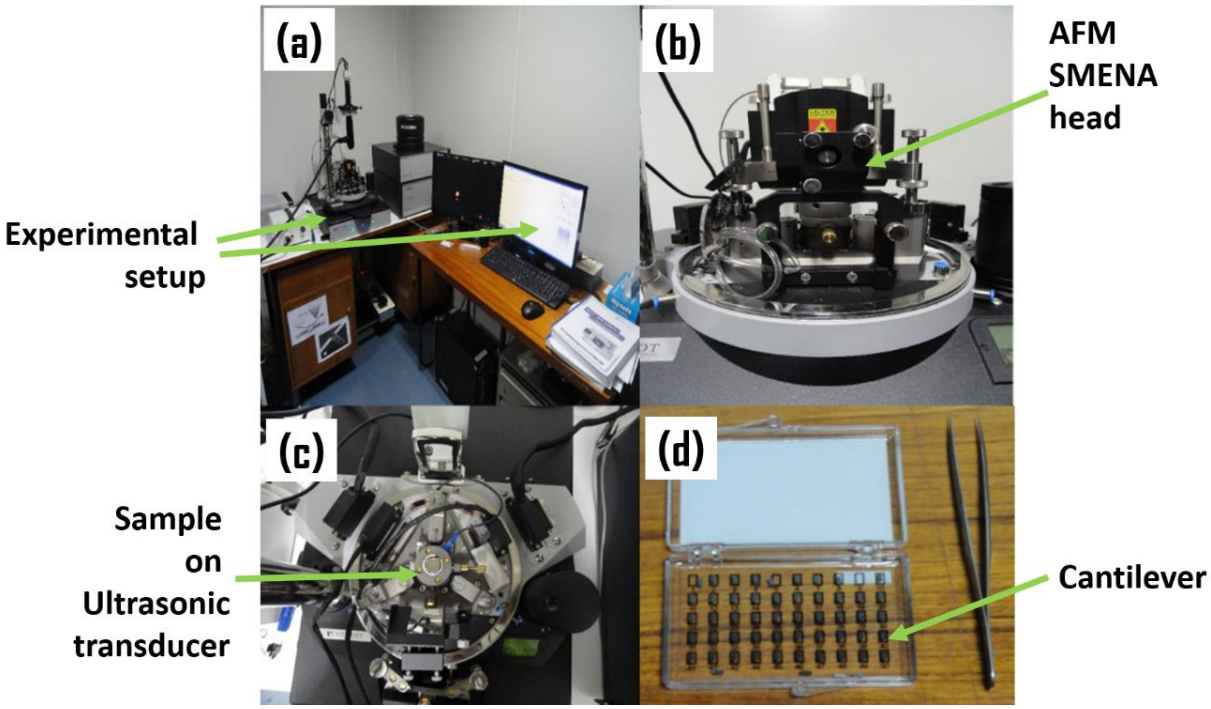

Figure 3.1: Photograph of AFAM setup showing (a) experimental setup, (b) AFM SMENA head, (c) sample stage with ultrasonic transducer and (d) cantilever box

3.2.1. NOVA© software

NOVA© control program is intended to operate instruments manufactured by NT-MDT. It can perform various tasks such as adjusting the optical systems (aiming), control the approach mechanism, acquire and process the frequency responses, process data obtained from the instrument, obtain Force–Distance curves, perform lithography operations, perform various advanced AFM operations (such as MFM, KPFM etc.), control over electromagnetic operations etc. Figure 3.2 shows the screenshot of the NOVA© software. NOVA© also provides possibility of writing own scripts for performing specific tasks using NOVA power script.

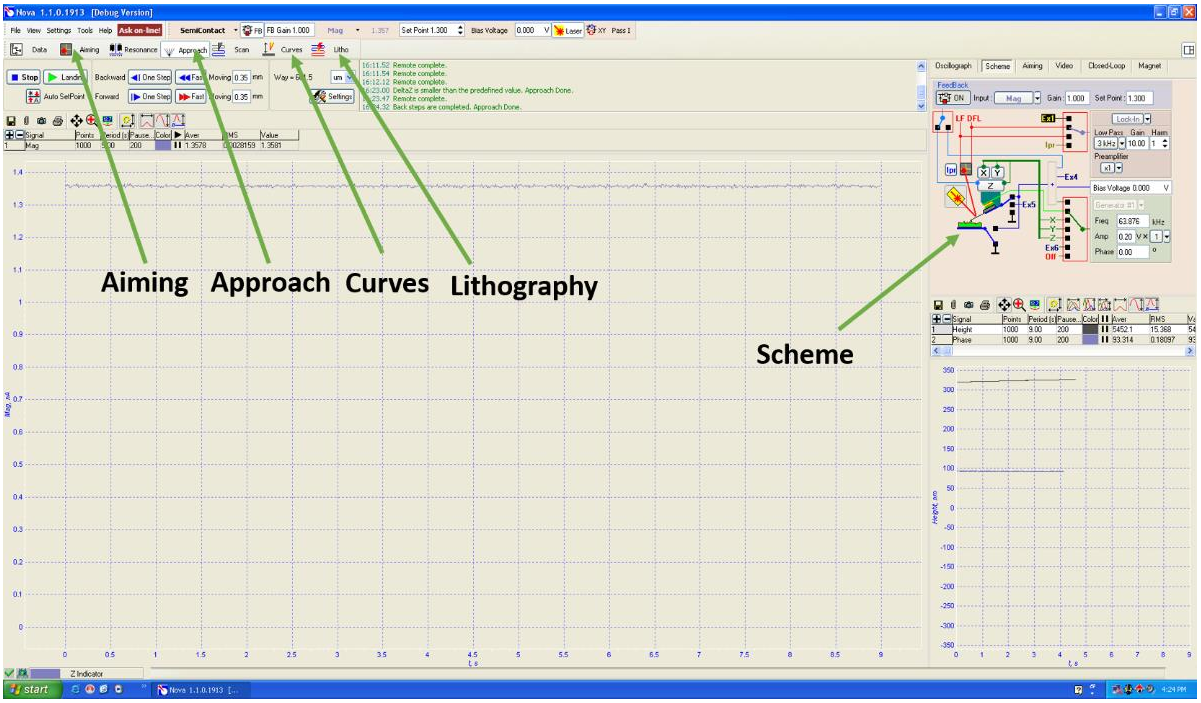

Figure 3.2: Screenshot of NOVA software

3.2.2. Cantilevers used in the present study

It is well known that long cantilevers are used for AFAM studies because of their ability to obtain clear contact resonance spectra (CRS) free from interference of other modes. Even, the strong adhesion forces at the contact between the sample and tip can overcome by using long and stiff cantilevers. Table 3.1 shows the different cantilevers used in the present study and their properties.

Table 3.1: Provides the details of the cantilevers used in this thesis for the study of elastic properties of various materials.

S. No:	Cantilever type	Free resonance frequency range (kHz)			Spring constant (N/m)
		1st mode	2nd mode	3rd mode	
1.	ACL[a], NCL[b], TAP[c]	145 – 180	900 – 1150	2300 – 2600	15 – 40

a- App nano, b- nanosensors, c- Budget Sensors

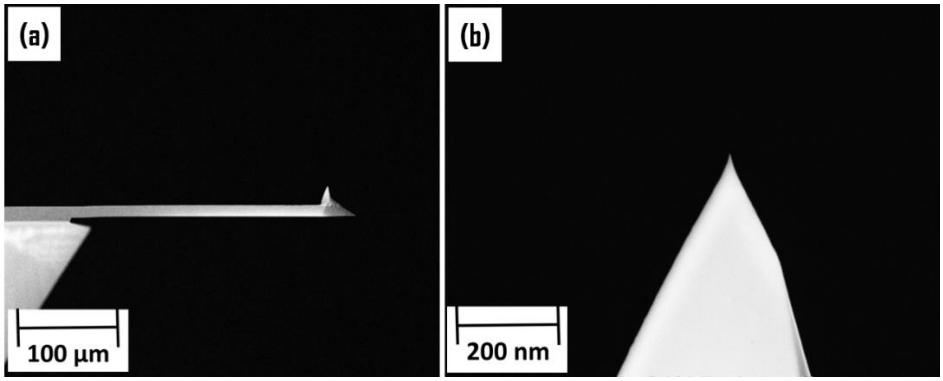

Figure 3.3: SEM images of the (a) cantilever and its (b) tip

All the cantilevers used in the present study were having lengths of 225 microns and widths between 30 – 40 microns. The tip radius mentioned for all the cantilever was > 6 nm as per the data sheets provided by the vendor. SEM images of the cantilever along with the tip are shown in Figure 3.3.

3.3. SOFTWARE DEVELOPMENT FOR DATA ACQUISITION

Specific software were developed in NOVA© power script which is based on Visual Basic (VB) script, a third generation event driven programming language. Scripts were developed for two types of measurements:

a) Point measurements

b) Grid measurements

Complete details of the scripts developed are given in the following sections. For further understanding of the various measurements carried out using AFAM, there is a need to define some of the terms:

Magnitude (Mag): It is the magnitude signal of the cantilever before landing

Deflection (DFL): It is the deflection signal of the cantilever

Setpoint (SP): It is actually a measure of force that is applied by the tip on to the sample surface and maintained by the feedback loop during measurement. It is actually a deflection signal of the cantilever in contact mode.

SP for semi contact AFM topography imaging is approximately equal to the Mag / 2 where Mag is the magnitude of the cantilever vibration before landing.

SP for contact AFM or AFAM studies: DFL + x (x varies with the type of cantilever: 0.1 - 5)

Feedback: The deflection of the cantilever is maintained by Feedback. Feedback maintains constancy in the force between the tip and sample. Feedback aids to obtain images with uniform forces when performing contact based AFM studies.

Feedback loop: It consists of tube scanner which will monitor the height of the tip, the cantilever and the optical lever. For a good AFM system, a very well-constructed feedback loop is vital.

3.3.1. Software developed for single point measurements in NOVA© Power scripts

As mentioned previously the setpoint is nothing, but the applied load on to the sample by the tip at which the measuremnets are made. Scripts were written to obtain CRS against a load (setpoint) range. Software was developed to acquire multiple CRS simultaneously against load. The importance of simultaneous acquisition of two CRS is discussed in detail in the following sections. Software obtains CRS for both increasing and decreasing load. The software includes option for choosing various parameters like number of data points required in each spectrum, frequency range and load range. Figure 3.4 shows the input dialogue box of the software.

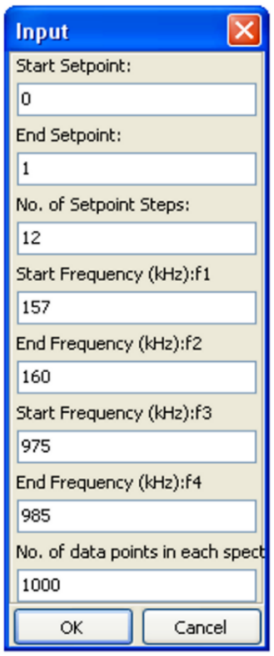

Figure 3.4: Input dialogue box for obtaining setpoint vs CRF

3.3.2. Software developed for grid measurements in NOVA© Power scripts

Software were developed to obtain CRS for a specified grid points in order to produce a CRF map. In conventional AFAM measurements, only one CRF is obtained for one full grid but here the program acquires data simultaneously for two CRFs. Each spectrum has 200 data points, for two CRS are simultaneously obtained so there are a total of 400 data points at each point. So, the total number of data points after acquiring for one full grid would be about 40,00,000 data points for a 100 x 100 grid size. Waiting time of 30 milli second (ms) was provided to acquire data for each CRF and a waiting time of about 100 ms was provided for storing the data for each line. The software includes option for choosing various parameters like number of data points in each spectrum, frequency range (for 1st CRF and 2nd CRF), grid size and step size in angstroms (Å). Figure 3.5 shows the input dialogue box for obtaining CRF map with various parameters.

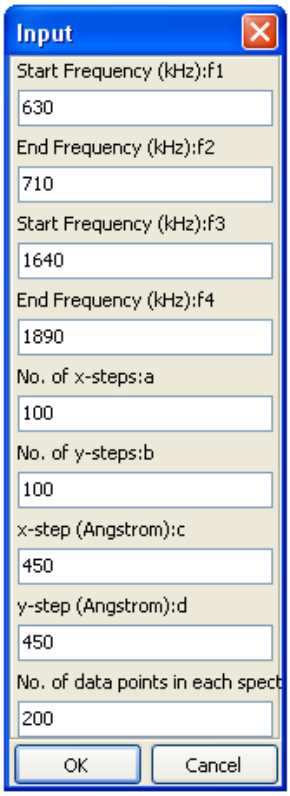

Figure 3.5: Input dialogue box for obtaining CRF map

3.4. SOFTWARE DEVELOPMENT FOR DATA ANALYSIS

3.4.1. Software development for point measurements in LabVIEW

Specific software were developed in LabVIEW (Laboratory Virtual Instrument Engineering Workbench), a graphical programming language, for analyzing the CRS obtained using the scripts developed in NOVA©.

3.4.1.1. Setpoint vs CRFs

This software is developed to analyze the data acquired using NOVA© mentioned in section 3.3.1. Figure 3.6 shows the front panel of the developed software. The data file obtained from the NOVA© contains information of CRF against increasing and decreasing load. The Setpoint values can be converted to load values by using Force-Distance curves. When a force

curve is obtained for a certain specified setpoint value (for e.g. 1- maximum load in the measurement) then the slope in the contact side will provide us the change in deflection value per change in value for applied current. This value of deflection can then be multiplied with the spring constant to obtain the applied load values.

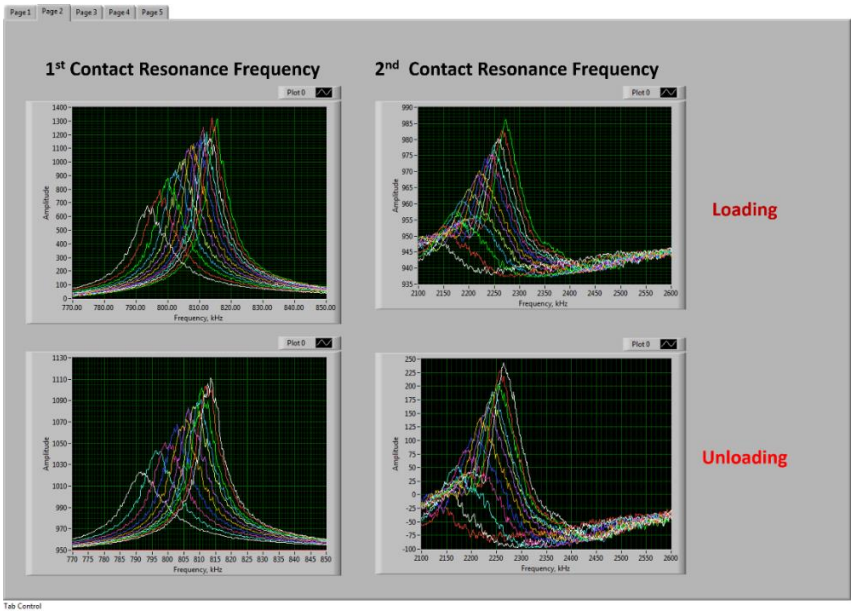

Figure 3.6: Front panel of the software developed for analyzing load dependence on contact resonance spectra

3.4.1.2. Deriving contact stiffness from contact resonance frequency

The characteristic equation required to convert these CRFs to k^* is discussed in AFAM theory section in Chapter 2. The free resonances and the CRF values are the inputs to this program. As discussed earlier, we need two CRFs to compute the k^*. Another way to compute the k^* is by knowing the free fitting parameter (L_1/L) using SEM. Here, in the thesis work, we used the first method. By plotting k^* as a function of the tip position (L_1/L) for the two modes, one obtains two curves, the cross-point of which yields a unique value of k^* for the two measured modes. The unique value from the two curves is taken as k^*. Front panel of the software can be seen in Figure 3.7.

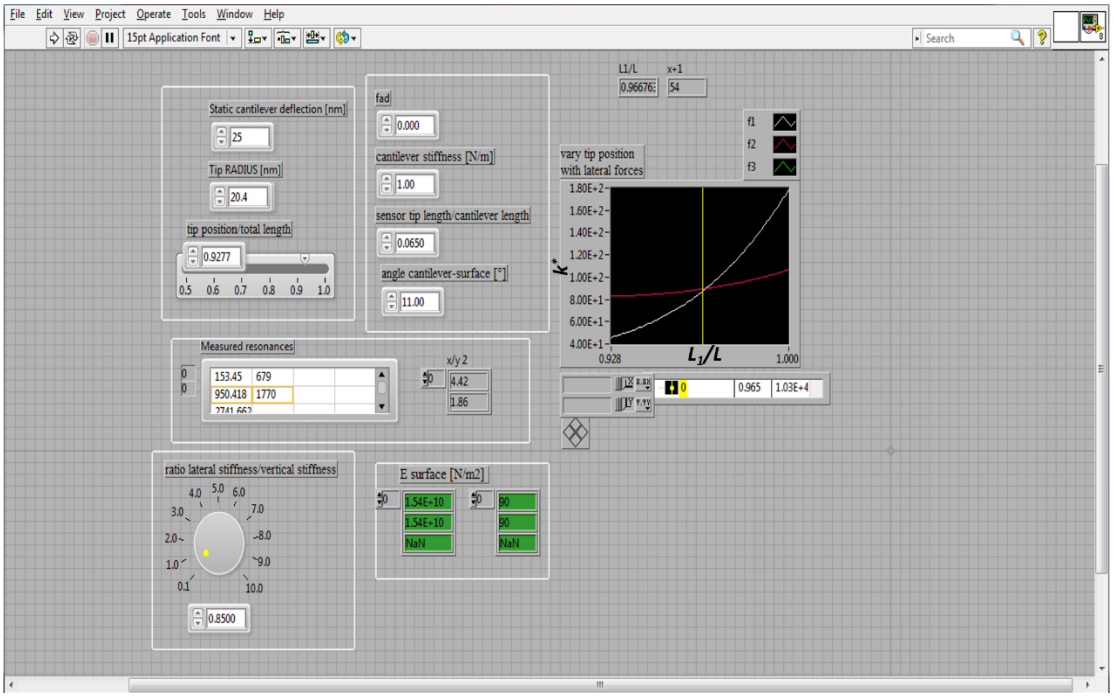

Figure 3.7: Front panel of the program for obtaining contact stiffness (k^*) from the CRFs

3.4.1.3. Setpoint vs damping

As mentioned in chapter 2, there are two important parameters to be decoded from the CRS: frequency shift and their widths. Frequency shifts provide information of stiffness at contact (k^*/k_c) and their widths provide the details of the contact damping (E''/E'). Hence, software was developed for simultaneous acquisition of stiffness and damping against increase in load. In general, the stiffness increases and the damping decreases with increase in load. The (E''/E') value obtained at high loads where there is no much decrease further would be the real internal friction value from the material. Figure 3.8 shows the front panel of the software developed for the simultaneous acquisition of stiffness and damping.

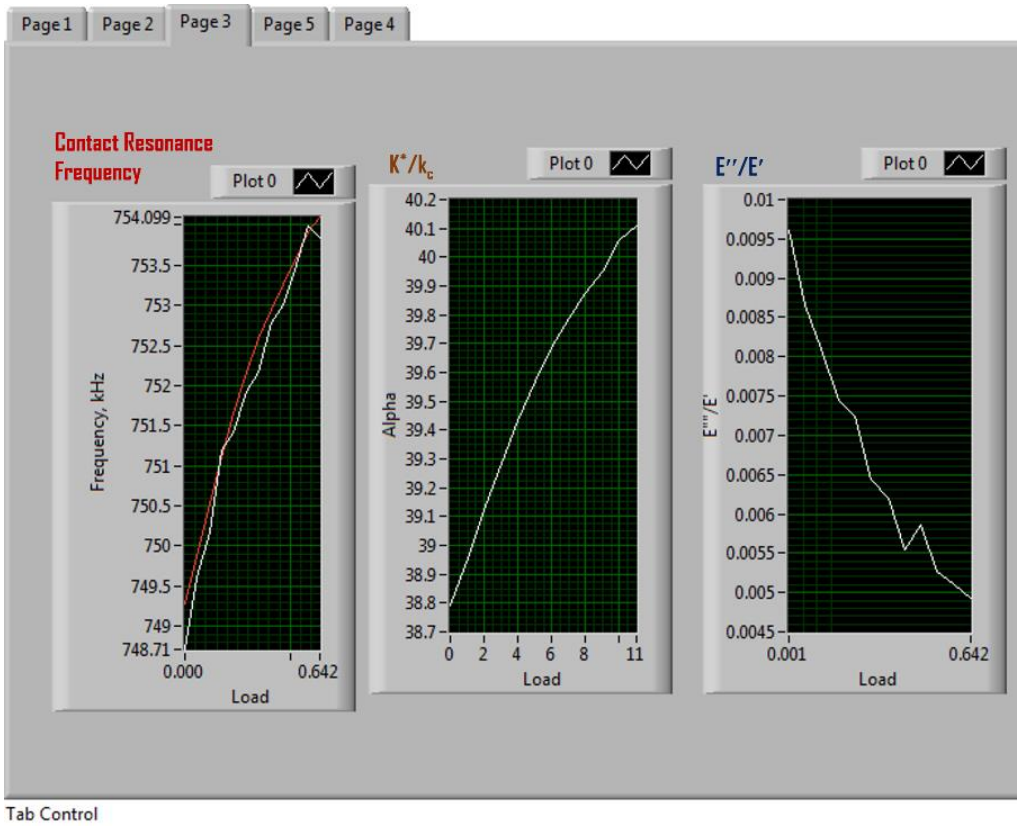

Figure 3.8: Front panel of the software for load vs damping.

3.4.2. Software developed for grid measurements in LabVIEW

3.4.2.1. Mapping of indentation modulus

A brief theory of AFAM and the calculation of indentation modulus using suitable models has already been discussed in Chapter 2. Discussion on the CDMs and their importance have also been discussed in sections 2.6.2.1 and 2.6.2.2. Software were developed both considering damping and neglecting damping. Section 3.4.1.1 discussed about the software developed for performing point measurements and also derivation of the contact stiffness from the CRFs. Figure 3.9 shows the flowchart of conventional AFAM system and the new methodology developed for obtaining indentation modulus of samples in this thesis.

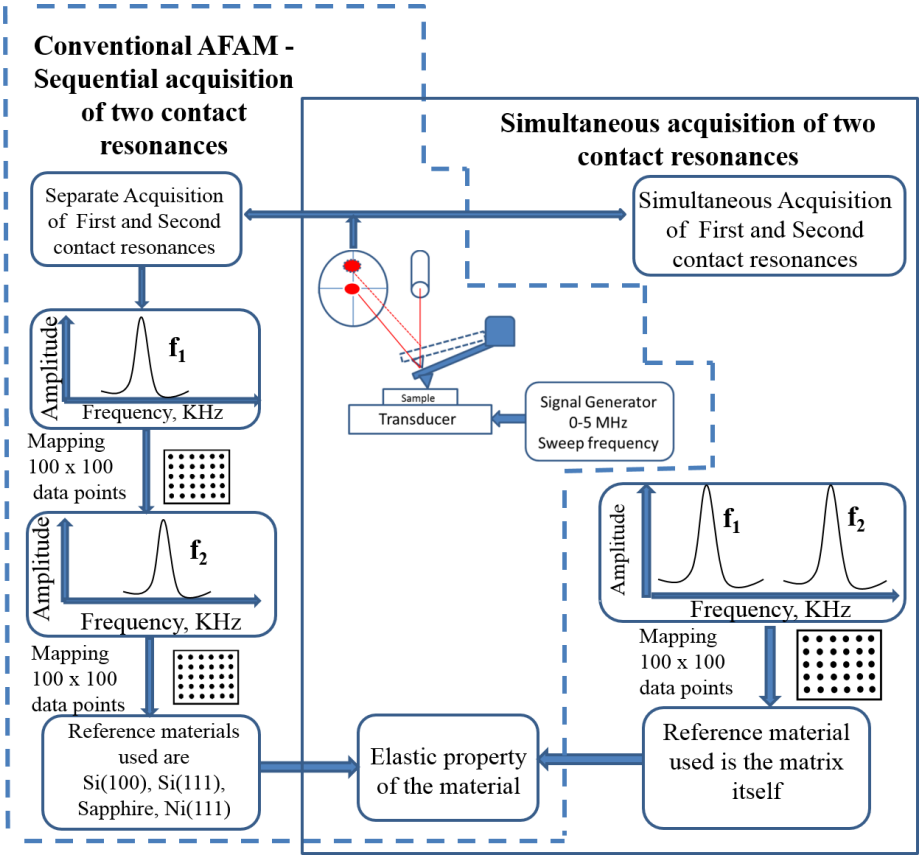

Figure 3.9: Conventional AFAM flow chart, where two contact resonances are acquired sequentially one after the other, and the new methodology of simultaneous acquisition of two contact resonances.

In the conventional AFAM measurements, the first and second CRFs are acquired at all grid points sequentially and then measurement is carried out on a reference. The underlying assumption is that both the CRFs are obtained at the same load and with the same tip condition. However, more often than not, this is not found to be true. This problem can be solved by simultaneous acquisition of two CRFs and selecting the matrix in each scan line as a reference [15]. The described methodology also eliminates repeated switching between an unknown sample and a reference for quantitative measurement of the indentation modulus.

The data obtained from the AFAM system contains two resonance frequencies at each pixel. Figure 3.10 shows the CRF maps along with their spectra generated for a specified 100 x 100 grid

data points. In Figure 3.10, a variation in the CRFs values along the map is observed. Sudden change in tip radius at 'E' led to a sudden increase in CRF values.

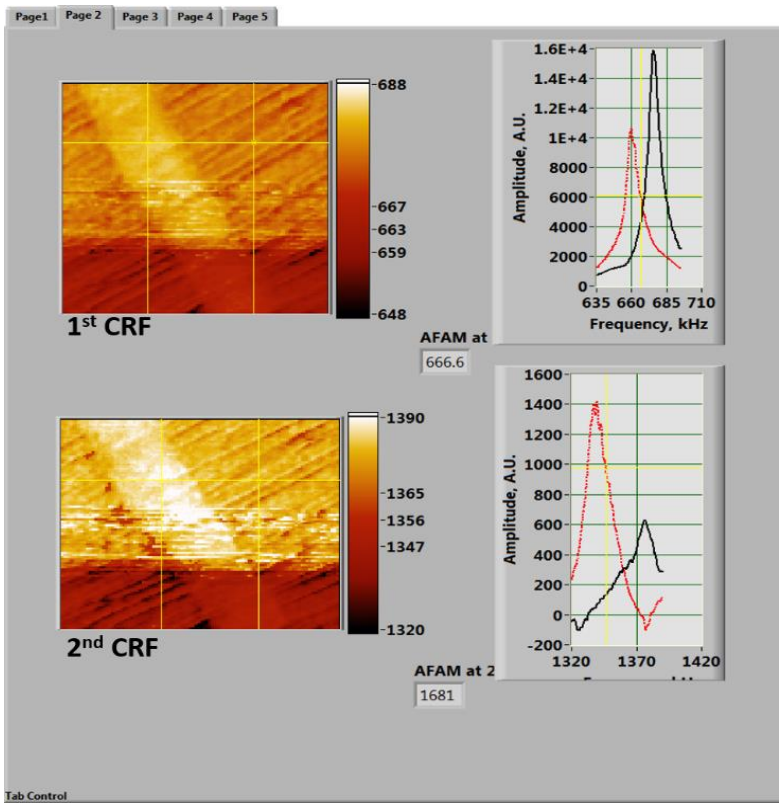

Figure 3.10: Front panel of the software developed for generating contact resonance frequency map

From these CRF maps, the k^* map can be generated, by using the software shown in Figure 3.7 as a sub VI into the software shown in Figure 3.11. Reference can be selected from the k^* map either selecting set of data points in a line or specific set of data points along a scan line (yellow box marked in k^* map as shown in Figure 3.11) can be used as reference to circumvent the problem associated with the change in tip radius, as shown in the indentation modulus map. The software developed for Modulus mapping needs the following inputs:

- File containing the CRS obtained using NOVA power script for grid measurements
- Free resonance frequency values (1st and 2nd CRFs)
- Mode numbers

- Matrix indentation modulus
- Selection of data points for reference

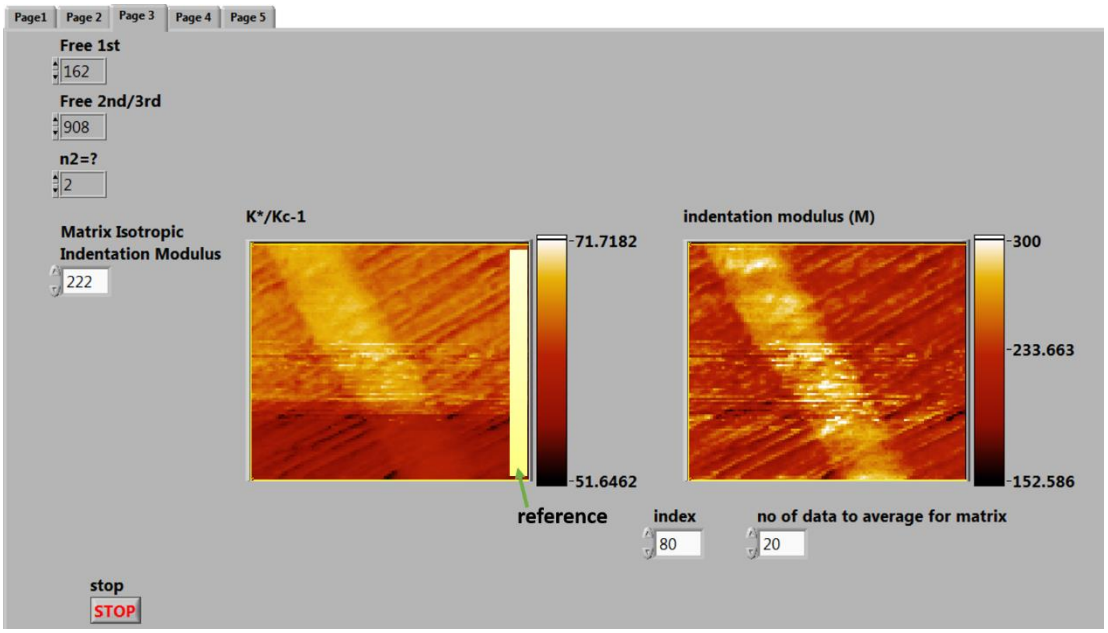

Figure 3.11: Front Panel of the software developed for generating indentation modulus map from the CRS

3.4.2.2. Mapping of stiffness and damping

As mentioned earlier, the CRS obtained from the AFAM system contains information of sample elasticity as well as the damping. CDM considering damping is already discussed in detail in Chapter 2. The obtained resonance curves are fitted with suitable non-linear fitting models mentioned in section 2.6.2.2. The best fit parameters from the non-linear fitting models are then used to calculate the complex quantities in the wave vector and later with suitable substitutions and analysis, the damping map can be obtained. The front panel of the software developed for simultaneous mapping of stiffness and damping is shown in Figure 3.12.

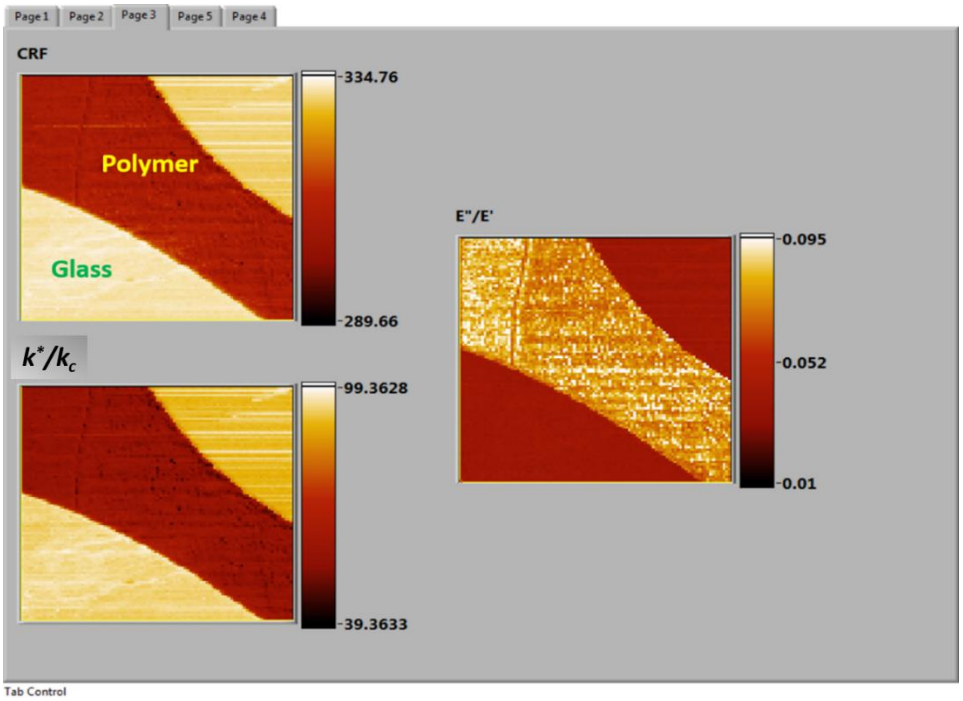

Figure 3.12: Front panel of the software developed for generating simultaneous maps of contact stiffness (alpha) and damping (E″/E′)

3.5. SPECIMEN PREPARATION FOR AFAM STUDIES

The details of the specimens studied in this thesis are given in Table 3.2.

Table 3.2: Details of the specimens used for the study in this thesis

S. No:	Material	Heat treatment details	Phases/Precipitates studied
1.	Polycrystalline Nickel base superalloy – Alloy 625	service exposed at 873 K for 60,000 h + 1123 K for 10 h, 200 h and 500 h aging	γ , δ and Carbides
2.	Directionally solidified nickel base superalloy – CM 247A supercast alloy	Double aged condition (1503 K/2 hrs. + 1533 K/2 hrs)/ + Aging at 1143 K/20 hrs + 1353 K	γ, γ′ and Carbides
3.	Ti-6Al-4V – (α + β) Titanium alloy	923, 1123 and 1223 for 1 h	α, α′and β
4.	Ti-10V-4.5Fe-1.5Al – β- Titanium alloy	823 K for 172 h, 923 K and 1000 K for 1 h	α and β

AFAM being a contact method encounters problem during experiments on samples with poor surface finish. A poor surface finish is always detrimental as it wears the tip and will alter the values obtained for modulus and damping. So, care should be taken for the preparation of the sample. All the samples used for the study in this thesis were first polished up to 1000 grit size SiC emery paper using an automatic polishing machine. Then diamond suspensions of 6, 3, 1 and 0.25 micron were used systematically to obtain a decent mirror polish. In order to remove the debris from the preceding polish, the samples were cleaned thoroughly after each and every polish. Polishing time was about 300 to 1000 seconds at every stage. To obtain, fine mirror finish and to maintain surface roughness below 5 nm, colloidal silica polishing (a combination of mechanical and chemical polishing) was used. It also helps to produce strain free surfaces after polishing. Colloidal silica contains typical particle sizes of < 70 nm which can maintain a surface roughness < 5 nm depending on the polishing time. Durations of 1000 to 4500 seconds for colloidal silica polishing was used depending on the material.

3.6. ULTRASONIC VELOCITY MEASUREMENTS

The modulus and damping data obtained by AFAM was correlated using the ultrasonic velocity measurements carried out on bulk samples. The details of the experimental setup used for ultrasonic measurements are given elsewhere [146, 152]. A 200 MHz broad-band ultrasonic pulser-receiver (M/s. Panametrics, USA) was interfaced with a personal computer having a PCI based 500 Ms/s digitizer card. Ultrasonic longitudinal and shear wave velocities were measured using 15 MHz and 5 MHz transducers, respectively. A LabVIEW-based software has been used to analyze the received ultrasonic signals to calculate the ultrasonic velocity and attenuation in the heat-treated specimens [146, 152]. The schematic of the experimental setup for ultrasonic measurement is shown in Figure 3.13.

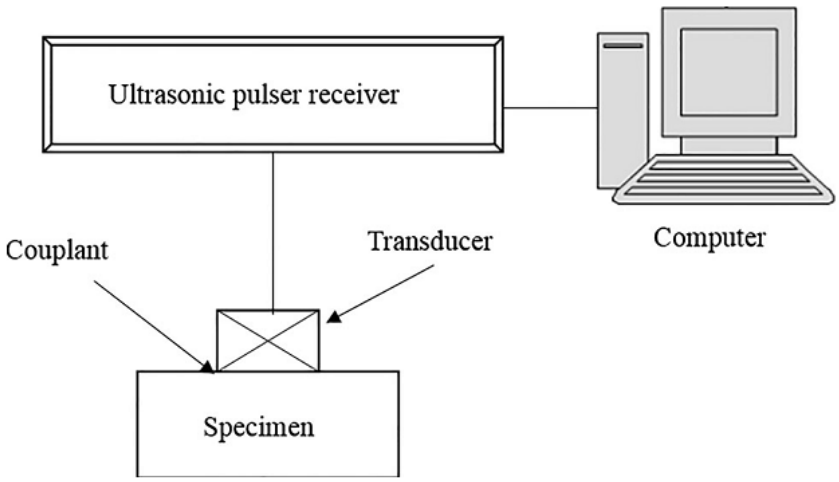

Figure 3.13: Schematic of the experimental setup for ultrasonic velocity and attenuation measurements

3.7. SUMMARY

The chapter discussed experimental setup and software developed for data acquisition and analysis. A new methodology for data acquisition and analysis was developed with which the problem of change in tip condition can be circumvented. Software were developed for simultaneous mapping of stiffness and damping properties in a material. Specimen details and sample preparation procedures were discoursed.

EFFECT OF VARIOUS PARAMETERS ON AFAM MEASUREMENTS

4

4.1. INTRODUCTION

The sensitivity and accuracy in the measurement of elastic and damping properties depends on several experimental parameters. This chapter studies in detail the effect of these parameters such as load, cantilever stiffness, angle, free fitting parameter (L_1/L), modulus of tip and choice of resonance mode on measurement of elastic and damping properties of the sample using AFAM.

4.2. THE LOAD EFFECT

Being a contact based AFM technique, AFAM measurements are influenced to a large extent, due to the load applied by the tip. To obtain the undistorted resonance curves throughout the scan one has to set a value of load that can provide good linear curves and also sense the shift in the contact resonance frequency (CRF) due to change in the local elasticity. To actually sense the response of the system to local elasticity, there is a need to understand the relation between the load and frequency and thus with the contact stiffness. The CRF increases with the load and the relation is governed by the tip geometry. Effect of applied load on CRFs, stiffness and damping are studied. Results obtained on a reference sample, fused silica are discussed in following sections.

4.2.1. Effect of load on frequency

Repetitive measurements were performed on fused silica to understand the effect of load on the frequency. Figure 4.1 shows the first and second contact resonance spectra (CRS) obtained on fused silica sample. The data was obtained using a intermediate stiff cantilever with spring constant ~ 17 N/m. The first and the second free resonance frequencies for the cantilever were

149.5 kHz and 933.5 kHz, respectively. Each spectrum contained thousand data points. The CRS were acquired at six different loads, in the range of 150 – 1000 nN with a step of ~160 nN. With increase in the load, the frequency is found to increase, depicted with the red arrows in Figures 4.1 (a) and (b).

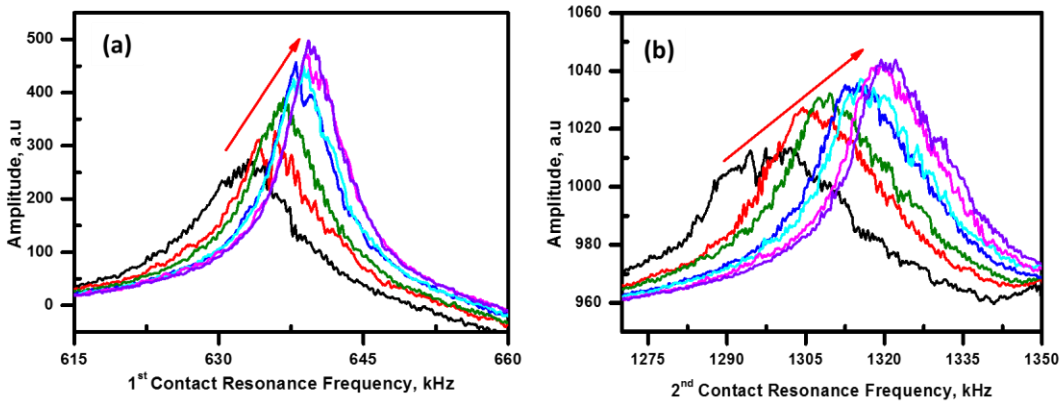

Figure 4.1: (a) 1st and (b) 2nd contact resonance spectra obtained on fused silica sample. Arrows (in red) represent increase in CRFs with increasing load

When the tip is sharper i.e. having small tip radius, the shift in the CRF is more. Smaller the radius of the tip better the resolution [94]. The theory behind the frequency shift is presented in detail in [153].

4.2.2. Effect of load on Contact Stiffness (k^*)

Contact stiffness (k^*) is defined as the ratio of change in force to the change in tip sample distance [12]. Interaction of the force of the cantilever on to the surface would give us the stiffness related to the sample, which then, can be used to derive indentation modulus using suitable contact mechanics models [12]. First part in the calculation of elastic properties is, finding a suitable cantilever dynamics model (CDM) which can be used to determine k^* from the obtained CRF values. The CRFs obtained against load (from Figure 4.1) has been used to obtain contact stiffness values using CDM given in equation (2.37). Due to increased stiffness at the contact, the contact

stiffness has been observed to increase always with increase in load. k^* exhibited a power law relation with load and is shown in equation (4.1) [118].

$$k^* \propto P^n \tag{4.1}$$

n, ranges from 0 (flat tip) to 0.33 (spherical tip). Hertz contact model with spherical tip condition is used in the thesis for calculating reduced modulus from k^* values obtained from CRFs using CDM. For high loads the tip gets damaged and gets blunt. Hence, an optimum load of about ~1000 nN was used for the studies in this thesis.

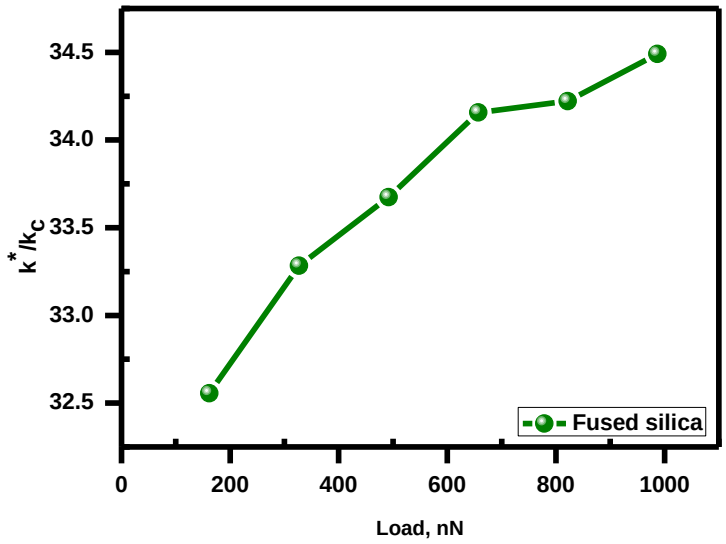

Figure 4.2: k^*/k_c vs load for fused silica sample

4.2.3. Effect of load on damping (E"/E')

The CR spectra shown in Figure 4.1 (a) have been used to calculate damping in the material fused silica, using equations (2.37, 2.43 - 2.45). It can be seen that the damping decreases with increase in load and becomes constant after a particular load (~ 800 nN). The constant value of damping at high loads provides the internal friction of material [24]. The decrease in the damping with increasing load is mostly attributed to micro slip of the cantilever at the contact [22]. Caron et al. [24] have observed that a background damping in the material related to the global ultrasonic absorption is obtained at higher loads only. An optimum value of load can be selected, at which

no noticeable wear of the tip and no slipping in the tip–sample contact will be observed and, hence, uniform measurements throughout the scan can also be assured. Figure 4.3 shows the plot of damping against load. Based on the results, a load of about 1000 nN was used for the measurements of elastic and damping properties in titanium alloys.

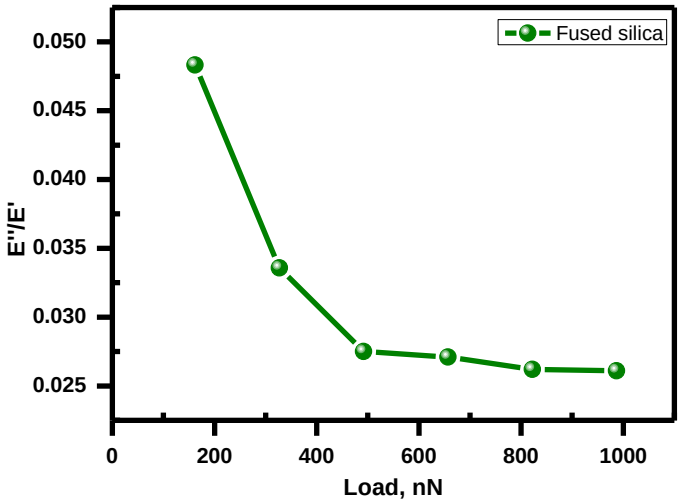

Figure 4.3: E″/E′ vs load for fused silica sample

4.3. EFFECT OF FREE FITTING PARAMETER (L_1/L)

In the previous chapters, the theory of AFAM is well explained and the need of two contact resonances have also been discoursed. By plotting k^* as a function of the tip position, r (L_1/L) for the two modes, one obtains two curves, the cross-point of which yields a unique value of k^* of the system. The other way to get the value of r is to measure using a SEM, which is time taking and may not be so accurate. Even, care must be taken during the transport of such tiny cantilevers between SEM and AFM.

Study was carried out to understand the effect of this parameter 'r' on the indentation modulus values obtained by AFAM. Data was obtained on three different materials and have been verified thoroughly by using different r values to check the effect on the reduced modulus ratio between the precipitate and matrix. The study was carried out on a composite material (Glass fiber

reinforced plastic (GFRP)), on alloy 625 with a delta precipitate and on a titanium alloy (Ti-6Al-4V) having α and β phases. It was found that the effect is very minimal in the case of harder materials (modulus > 200 GPa) and more on softer materials such as composites.

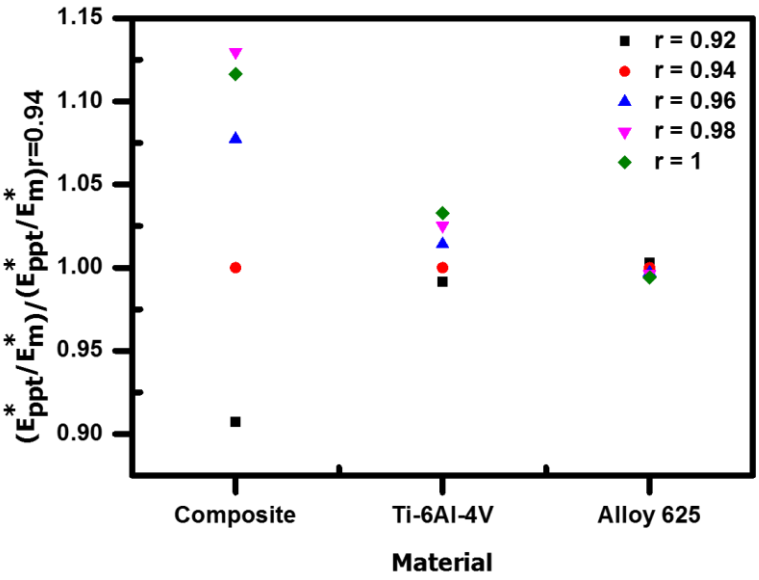

Figure 4.4: Effect of r (=L_1/L) on the relative change in reduced modulus for different materials

It is clear from Figure 4.4 that, change in the value of *r* has very less effect in the case of stiff materials (alloy 625). For variation of ±0.02 in r, errors of 2.3 % and 0.3 % have been observed for alloy 625 and titanium alloys, respectively. However, in the case of GFRP, an error of about 17.5 % was observed. This is attributed to similar variations in k^* with *r* for stiff materials with slight difference in elastic properties as shown in Figure 4.5 (a) for α and β phases in titanium alloys. The k^* variation with *r* is very much different for glass and epoxy (Figure 4.5 (b)), leading to more error as observed in Figure 4.4. based on these results, a constant value of r (= 0.94) has been used for measuremnets of elastic properties in titanium alloys, where only one CRF is used as discussed in following sections.

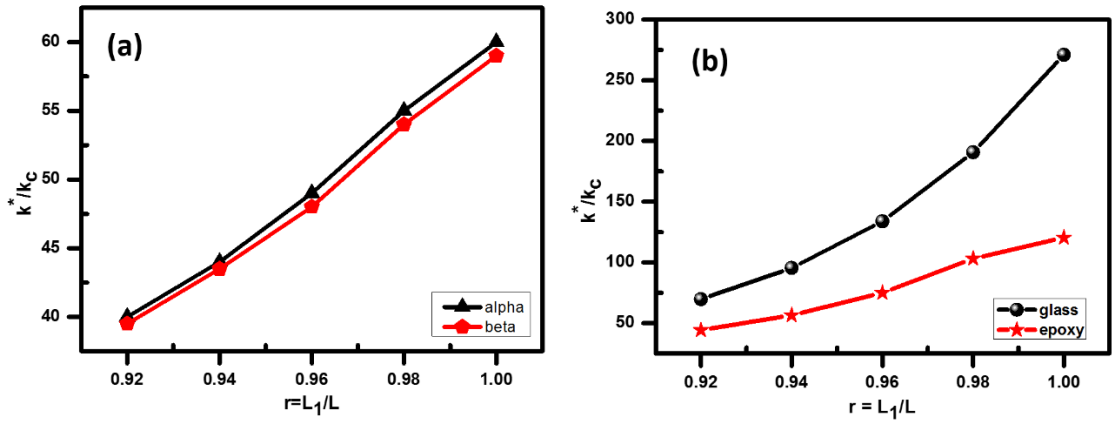

Figure 4.5: Variation in k^*/k_c with different r values obtained for (a) α and β phases in titanium alloys and (b) matrix and reinforcement in glass fiber reinforced plastic

4.4. ANGLE EFFECT

In AFM, the cantilever is always kept at an angle to avoid contact between the another part of cantilever chip or chip holder and sample surface before the tip and to avoid interference of the laser spot with the sample and cantilever, due to the fact that, the laser spot is larger than the width of the cantilever [154]. The angle mentioned by most of the manufactures is in the range of 10-15 deg. Due to the realization that, angle may vary slightly due to non-parallel surfaces, the effect of the value of the angle in contact stiffness calculations have been studied. Study was carried out on a composite material (GFRP), on alloy 625 with a delta precipitate and on a titanium alloy having α and β phases.

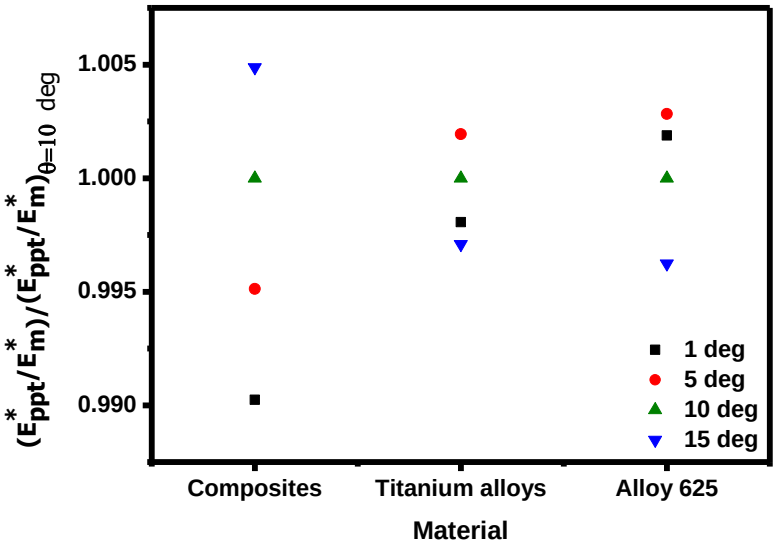

Figure 4.6: Variation in the ratio of reduced modulus with respect to θ = 10 deg against different materials for a range of cantilever angle values

Figure 4.6 shows a plot of relative modulus against materials for different angles. For all the calculations, *r* of 0.94 was used. It is observed that, by changing angle values in the range of 1-15 deg in equation (2.37), the relative modulus values remained the same. Variation of less than 1.5 % has been found for all the values of angles studied on three different materials with varied stiffness. As it is well known, that the cantilever is found to be at 10-15 deg using an approximate of 12 deg would be optimum for all the elastic property calculations using AFAM and hence used in all the measurements presented in this thesis.

4.5. TIP MODULUS EFFECT

Choice of the tip is very important in studying the elastic properties. Harder tips wear less and can be used for prolonged measurements. Diamond tips are better than silicon tips but lack in tip size (typically >50 nm), whereas the silicon tip radius are below 10 nm. Figure 4.7 (a) shows the variation of E^* values for a range of *M* values and (b) shows the sensitivity plotted for the data in (a). The green dotted line in the figure points out the *M* value of the silicon tip i.e. 165 GPa. Plot was obtained using the equation (2.52). Two main classes of materials (nickel base superalloys

and titanium alloys) were used for study in this thesis work. The range of M values for both the materials are indicated in Figure 4.7. For the case of titanium alloys, sensitivity will be better when using silicon tip and slightly reduces when working on nickel base superalloys which bear modulus values > 200 GPa. Sensitivity is found to drop with increase in *M* values.

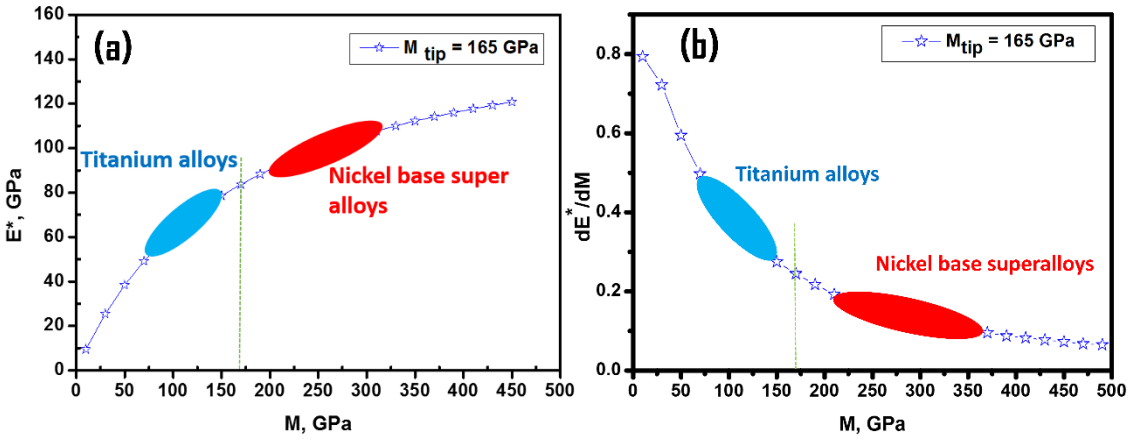

Figure 4.7: Variation in (a) E^* and (b) dE^*/dM with indentation modulus for Si (100) tip. The dotted line (green) in the figure represents the modulus of the tip used for AFAM studies

4.6. SPRING CONSTANT EFFECT

Cantilevers are produced with varied spring constants. The variation in spring constant, helps in studying various type of materials with varied stiffness. Soft cantilever, in general has better control on load as compared to stiff cantilevers. Soft cantilever provide better resolution when studying soft materials and intermediate stiff and stiff cantilevers can be used for stiff materials. Dispersion curves generated for two modes for the three types of cantilevers are shown in Figure 4.8 (a). Mode sensitivities for the three cantilevers are compared in Figure 4.8 (b and c).

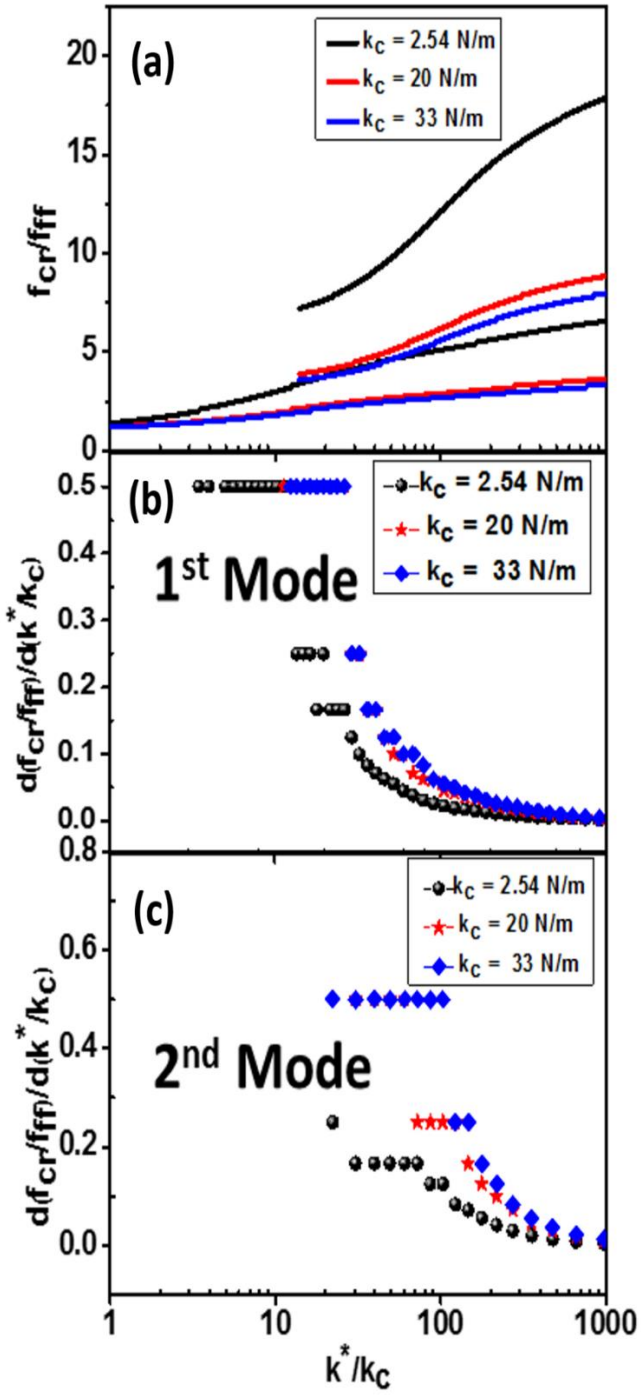

Figure 4.8: (a) Dispersion curves plotted for soft (k_c=2.54 N/m), intermediate stiff (k_c = 20 N/m) and stiff (k_c = 33 N/m) cantilever. Sensitivity of (b) 1st and (c) 2nd modes for the three types of cantilevers

It is clear from Figure 4.8 that, when studying softer materials (low k^*/k_c) with softer cantilevers the 1st mode is sensitive and as k^*/k_c values increase the 2nd or higher modes become more

sensitive. When studying materials with high k^*/k_c, stiff cantilevers may be used. Hence, in the present study, measurements are performed with cantilever's possessing stiffness values in the range of 20 – 33 N/m. As the sensitivity decreases with increasing k*/Kc, best sensitivity in modulus measurements can be achieved at low loads using stiff cantilevers with sharp tips.

4.7. CHOICE OF APPROPRIATE RESONANCE MODE

In AFAM studies, as mentioned in section 2.6.2.1, two CRFs are used to calculate the stiffness at the contact and thus the elastic property. By plotting k^* as a function of the tip position (L_1/L) for the two modes, one obtains two curves, the cross-point of which yields the unique value of k^* of the system using both the modes [12]. In this thesis, two main classes of multiphase structural alloys were studied: nickel based superalloys and titanium base alloys. The nickel base superalloys exhibit M values in the range of 200-350 GPa and titanium base alloys exhibit M values in the range of 70-145 GPa. Using load of about ~ 1200 nN and radius of the tip 40 nm and substituting them in to the equation (2.50), we get range of k^*/k_c values for nickel base superalloys and titanium base alloys as 70-100 and 35-60, respectively. Figure 4.9 shows the dispersion curve obtained for a stiff cantilever. The obtained k^*/k_c values for both the multiphase structural alloys are marked in Figure 4.9. It is clear from the figure that, the second mode exhibited better sensitivity than the first mode in case of nickel base superalloys. The second mode mostly exhibited clear spectra with no interferences with other spurious peaks or modes in case of nickel base superalloys. Hence, two modes (first and second) can be used for study. However, in case of titanium alloys, both modes (first and second) exhibited similar sensitivity. Here, the second mode mostly exhibited interference with spurious distorted peaks. Since damping measurements were also carried out for titanium base alloys, only the first mode was used for calculations as it would be difficult to fit the distorted second mode.

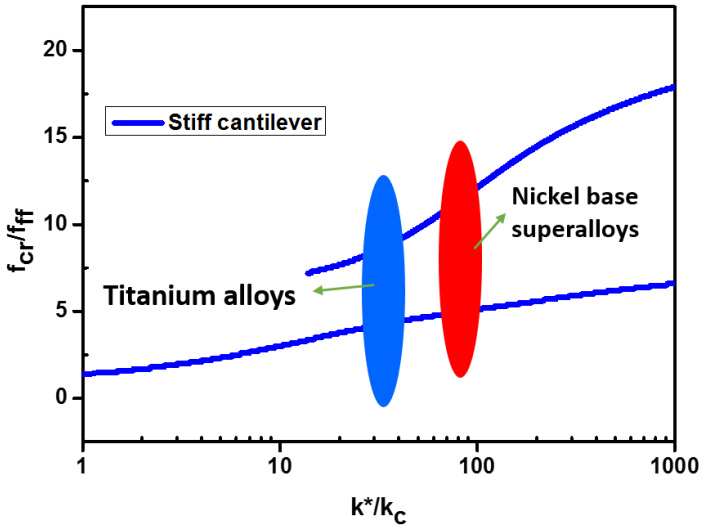

Figure 4.9: Dispersion curves plotted for a stiff cantilever (k_c ~ 33 N/m). Materials used for the study in this thesis are marked on the dispersion curve to show the different sensitive areas in case of two modes

4.8. CONCLUSIONS

The influence of various parameters affecting AFAM nanomechanical property measurements were understood in the present chapter. The results indicate that:

1. There is a power law relation between k^* and load applied on to the cantilever.
2. With decreasing load, an exponential increase in damping is observed resulting due to micro slip. The flat portion obtained in the damping (i.e. internal friction) at high loads would be the real damping of the material.
3. Sharper the tip, better the resolution in frequency and k^*.
4. Materials having higher modulus than the tip would suffer from poor resolution.
5. Two CRFs should be used while studying stiff samples due to the higher sensitivity of the second mode, whereas the 1st CRF would be enough while working with intermediate stiff or compliance materials because of similar sensitivities of the two modes and also the second mode may exhibit spurious peaks.

6. Based on the results obtained in the present chapter, the first and second CRFs are used in the thesis for obtaining indentation modulus in stiff materials i.e. nickel base super alloys using stiff cantilevers (k_c~30 N/m). However, for titanium alloys, only the first CRF of an intermediate stiff cantilever (k_c ~20 N/m) was used.

MAPPING OF ELASTIC PROPERTIES IN NICKEL BASE SUPERALLOYS USING ATOMIC FORCE ACOUSTIC MICROSCOPY

5

5.1. INTRODUCTION

Nickel base superalloys find wide spread applications in critical components such as aircraft and power-generation turbines, rocket engines, and other challenging environments, including nuclear power and chemical processing plants due to their outstanding properties like high-temperature strength, toughness, and resistance to degradation in corrosive or oxidizing environments [123]. Two types of nickel base alloys are widely used, polycrystalline superalloys [155] and directionally solidified superalloys [131]. Polycrystalline superalloys have applications from intermediate temperatures to high temperatures, whereas, directionally solidified superalloys are meant for high temperature applications, where creep is of utmost concern. Jena et al. [156] have studied the role of alloying elements in the design of nickel base superalloys and have also given clear classifications of various alloying elements included in forming intermetallics, carbides, nitrides, surface stabilizers and solid solution formers. Nickel base superalloys exhibit complex microstructures [157]. The strength of these alloys are mostly derived from the coherent γ' (Ni_3 (Al, Ti) based $L1_2$ structure) precipitates, in exception with alloy types which are strengthened by γ'' precipitates (Ni_3(Nb, Mo, Al) based DO_{22} structure) [29, 157]. The metastable γ'' phase transforms to orthorhombic δ phase (Ni_3 (Nb, Mo)) having a DO_a structure upon prolonged aging [126, 158]. Further, various types of carbides are also observed in different nickel

base superalloys. A polycrystalline superalloy, alloy 625 and a directionally solidified super alloy, CM 247A are studied in this thesis. Alloy 625 was initially designed as a solid solution hardening alloy, however it has been observed that, when the alloy is subjected to aging treatment in the range of 823 – 1023 K, precipitation of intermetallic phases and carbides occur [126]. When alloy 625 is subjected to precipitation hardening treatment in the temperature range of 823 – 923 K, strengthening of the alloy is from γ′′ metastable phase. The γ′′ (Ni_3 (Nb, Mo, Al)) metastable phase is the main strengthening phase and is finer in size. This metastable phase can transform into δ phase, an orthorhombic phase, upon prolonged aging. Higher precipitation of this δ phase leads to increase in the yield strength and lowers the ductility [126]. The precipitation of δ-phase significantly influences the mechanical properties of nickel base superalloys, such as alloys 625 and 718 [122, 126, 127, 159]. Kumar et al. [159] have studied the influence of the precipitation of various intermetallic phases, including the δ-precipitate, on elastic and mechanical properties of alloy 625. Carbides in the alloy 625 precipitates in temperature range of 1033 – 1253 K [160]. Size (diameter/breadth) of various precipitates present in alloy 625 are in the range of 10 – 2000 nm.

CM 247A is an aeronautical grade advanced nickel base cast super alloy equivalent to CM 247 LC. CM 247A alloy was developed by M/s. Mishra Dhatu Nigam Limited, Hyderabad, India in remelt stock form with R&D inputs from Defense Metallurgical Research Laboratory, Hyderabad, India [129, 161]. The alloy was developed keeping in view its high temperature strength capabilities, which is one of the principal requirements for aero-engine hot end applications, such as turbine blades and vanes and automotive turbocharger rotors. The strength of this alloy is derived from a large amount of γ′ phase, which occurs coherently with the γ matrix. There are many studies reported for various morphological types (spheres, cubes, aligned cubes, plates, short plates, a doublet of short plates, an octet of cubes, large plates, rafts etc.) of the γ′ phase in CM

247A [129, 162, 163]. Studies were also reported on size, distribution and volume fraction of the γ′ phase and carbides precipitating at grain boundaries and their relation with mechanical properties at high temperatures [129, 162]. To obtain good mechanical strength, the alloy in solution treated and double aged condition to increase the volume fraction of γ′ phase and to increase the size of carbides at grain boundaries [162, 163]. Size (diameter/breadth) range of the various precipitates/phase in alloy CM 247A are in the range of 500 – 3000 nm.

Knowledge of the elastic properties of the phases/precipitates is very important for understanding the deformation behavior, crack nucleation and propagation, dislocation activity and interaction with grain boundaries and also even helps in understanding the bulk elastic properties of the structural alloys. Various first principle calculations/experimental studies have been reported for determination of elastic properties of various types of precipitates either prepared as single crystals or polycrystalline bars. Dai et al. [164] and Yong et al. [165] have theoretically calculated the elastic properties of δ-phase based on the first-principle studies. They reported the values of Young's modulus and Poisson's ratio for Ni_3Nb with DO_a structure to be in the range of 250-270 GPa and 0.33-0.35, respectively. Summary of characteristics and properties of various types of carbides obtained by experimental or first principle calculations can be found in ref [166]. Xie et al. [167] provided a simple and promising method for studying the properties of $Cr_{23}C_6$ carbides which possess complex structures. It was observed that with replacing two or three Cr atoms with Fe/Mo atoms the modulus can significantly increase from 250 to 330 GPa. Li et al. [168] calculated the E and ν values for $Cr_{23}C_6$ as 372 GPa and 0.28 using first principle calculations. Wang et al. [169] studied the elastic properties of γ′ (Ni_3Al) crystals using DFT calculations and reported E as 235 GPa and ν as 0.28. Fatmi et al. [170] used two types of approximations (Generalized gradient approximation (GGA) and Liner Density Approximation (LDA)) in the first principle calculations to obtain the modulus of γ′ (Ni_3Al). The reported E for

γ′ (Ni_3Al) is in the range of 197 – 233 GPa and ν value is 0.32. Wang et al. [171] performed nanoindentation studies on Ni_3Al crystals grown in (001), (110) and (111) orientations. The modulus of crystals grown in (001) orientation was found to be 17 % smaller than the other two orientations. Jun et al. [172] have reported the Young's modulus values for NbC as 470 - 480 GPa and of TaC as 490 - 537 GPa. The studies on polycrystalline bars made of NbC and TaC were carried out using sonic resonance method. Torre et al. [173] studied the elastic properties of TaC using ultrasonic velocity measurements and Density Functional Theory (DFT) calculations and reported the Young's modulus (E) and Poisson's ratio (ν) value as 550 GPa and 0.21, respectively. Bartlett et al. [174] reported the E and ν value of TaC as 477 GPa and 0.15, respectively. Opeka et al. [175] studied the mechanical properties of HfC billets with varied carbon percentages. Elastic moduli of the billets were calculated using ultrasonic velocity measurements as well as from the ring tensile and 3-point flexural tests. E values calculated from these tests were in the range of 270 - 430 GPa. Other reported E values for carbides, of Hf, Ti and Mo are in the range 350-510 GPa [166], of Ti, 186 – 461 GPa [176] and of Mo as 535 GPa [166], respectively. The large variation in the modulus values for the various precipitates are due to measurements carried out on varied purity, varied stoichiometry and porosity. Even though various studies are reported on the elastic properties of phases present in nickel base superalloys, only a few studies are reported on experimental measurement of elastic properties on precipitates embedded in nickel base superalloys. Atomic force acoustic microscopy (AFAM) allows measurement of elastic properties on a sample surface with a spatial resolution of about 100 nm. Hence, in the present study AFAM is used for measurement of elastic properties of individual precipitates in nickel base superalloys.

Even though a lot of studies have been reported on elastic properties of various materials, very scarce data is available on elastic properties of precipitates present in structural alloys which are highly technologically important. The lateral resolution of the obtained elasticity data from AFAM is proportional to the tip radius [8]. Sharper tips give better resolution and detection. In general,

precipitates of size smaller than hundred nanometers cannot be imaged using AFAM. Hence, in the present study, mapping of elasticity is performed on the precipitates with size more than 100 nm, viz., δ and carbide phases in alloy 625 and γ′ and carbides present in CM 247A alloy. All these precipitates have been reported to have orientation relationship with the matrix such that the close packed planes/directions for the precipitates are parallel to that of the matrix. The γ′ and carbides are reported to have cube-cube relationship ($\{001\}_{carbide} \parallel \{001\}_{matrix}$; $\langle 100\rangle_{\text{carbide}} \parallel [100]_{\text{matrix}}$), whereas δ exhibits $\{111\}_{\gamma} \parallel (010)_{\delta}; \langle 1\bar{1}0\rangle_{\gamma} \parallel [100]_{\delta}$. The (010) orientation is the close packed plane and [100] is the close packed direction in δ precipitates.

5.2. EXPERIMENTAL DETAILS

Intermediate stiff cantilevers with a spring constant, k_c, of about 24 N/m and the first free resonance frequency, f_0 of about 148 kHz were used in the investigation. In the conventional AFAM measurements, the first and second CRFs are acquired separately and then measurement is carried out on a reference. The underlying assumption is that both the CRFs are obtained at the same load and with the same tip condition. However, more often than not, this is not found to be true. In order to circumvent the problem associated with the tip wear, a new approach was developed by simultaneous acquisition of two CRFs and selecting the matrix in each scan line as a reference. The described methodology also eliminates repeated switching between an unknown sample and a reference for quantitative measurement of the indentation modulus. A schematic of the methodology is depicted in Figure 1. Each CR spectrum consisting of 200 data points leading to a resolution of 0.2 kHz was obtained at each point. The scan step size of about 50 nm was used for all the superalloy samples. Statistical analysis was carried out to obtain their indentation modulus. The mean indentation modulus values with the standard deviation as scatter band are reported in the present study.

Service exposed (873 K, 60,000 h) alloy 625 samples [126, 159] were post service heat treated at 1123 K to dissolve the intermetallic precipitates (Ni_2(Cr, Mo) and γ'') [126], without dissolving the grain boundary carbides precipitated during service exposure. Post service heat treatment at 1123 K for 10 h, 200 h and 500 h were used in the present investigation. A directionally solidified superalloy (CM 247A) sample in double aged microstructural condition [129] was also taken for the investigation. The nominal chemical composition of the two alloys are given in Tables 2.5 and 2.6.

All the samples were of size ~ 10 x 10 × 5 mm^3. Sample surfaces were prepared using conventional metallographic technique up to 0.25 μm diamond polishing. To obtain, fine mirror finish and to maintain surface roughness below 5 nm, colloidal silica polishing (a combination of mechanical and chemical polishing) was used. The surface topographies of the specimens were obtained in AFM tapping mode to select areas with sufficient flatness for acquiring the contact-resonance spectra. In the as polished condition, the grain boundaries and precipitates were visible in the AFM image due to a slight topographic difference (<10 nm) for the precipitates and the matrix.

Precipitates present in both the alloys were identified and confirmed using scanning electron microscopy (SEM) and Energy-dispersive X-ray spectroscopy (EDX). A Zeiss SUPRA 55 Gemini field emission gun (FEG) SEM was used at an accelerating voltage of 20 kV, an aperture of 60 μm and a working distance of 12 mm.

5.3. RESULTS AND DISCUSSIONS

5.3.1. Simulatenous measuremnet of two contact resonance spectra

In the conventional AFAM based measurements, the two modes of contact resonances are obtained in a sequential manner, explained in chapter 3. As shown in Figure 3.9, the contact

resonance of one mode is obtained on the sample at the planned grid points and subsequently the second mode of contact resonance is measured at those locations. In such a mode of operation, if the tip condition changes during a scan, the two contact resonances are not obtained with the same tip condition and hence the basic assumption for satisfying equation (2.51) is not valid. This can be taken care by acquiring the two contact resonances simultaneously. However, the difference in the two modes of frequencies is usually very high (>900 kHz for a cantilever with 1st free resonance frequency as 160 kHz) and the band-width (useful range) of resonance is quite small (<50 kHz). Hence, the acquisition time increases significantly if the whole range including the first and the second contact resonances is selected for simultaneous acquisition with sufficient resolution. Recently, Kopycinska et al. [177] has successfully demonstrated the dual resonance excitation by modifying the electronics and performed point measurements on different reference samples like fused silica (FS) and organosilicate glass (OSG). Another point to be considered, is that the second contact resonance mostly gets distorted or splits as the tip get blunts [94]. Optimum load is required to study the elastic properties with reduction in tip wear. With lower loads, a spherical contact can be visualized and hence better resolution in the image. For all the samples, an optimum load was used to acquire the data. It is well known from literature, that different orientations of the precipitate possess different elastic properties [11, 16].

Specific script was developed for acquisition of two contact resonances simultaneously by providing suitable range of frequencies for the two modes of resonances. The methodology adopted in our measurement is described schematically in Figure 5.1 showing the simultaneous acquisition of two contact resonances and using the matrix as the reference. The developed methodology ensures the acquisition of both the resonances with high resolution in the same tip condition thus fulfilling the basic assumption in Equation (2.51). Further, as the frequency range for the measurements is selected separately for the two modes, time taken for the acquisition is

also minimal. Even if the tip changes during a scan, both the contact resonances are obtained with the same tip condition and hence a unique value of k^* is obtained, as shown in Figure 5.1.

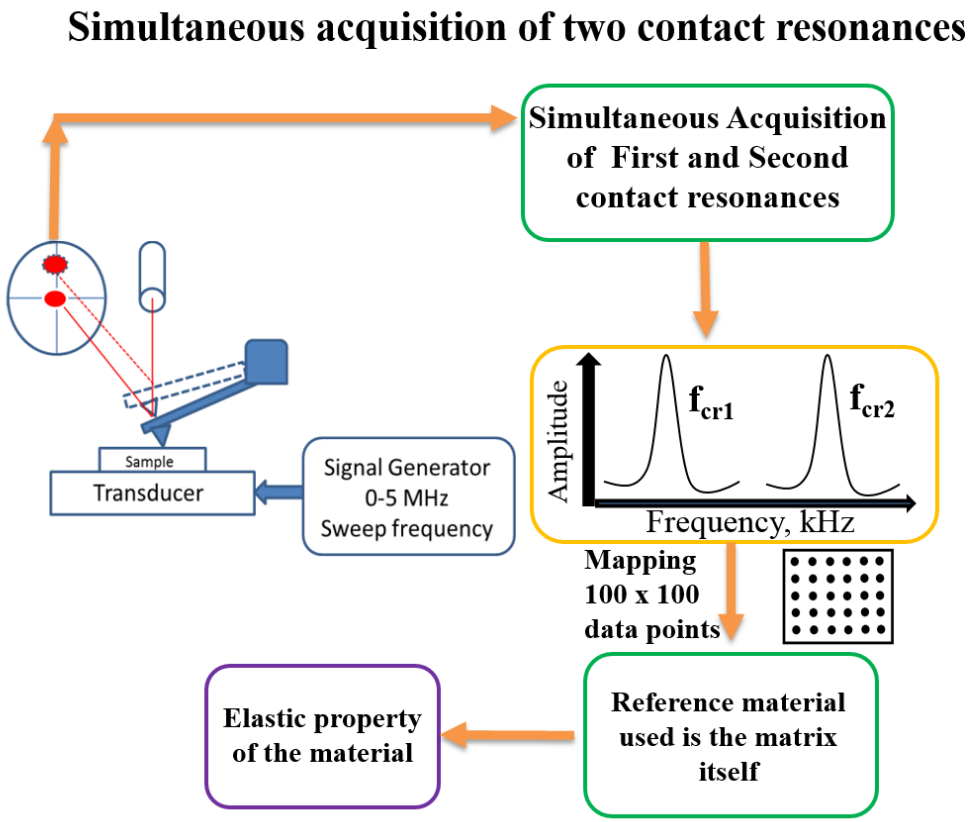

Figure 5.1: AFAM flow chart showing the new methodology of simultaneous acquisition of two contact resonances.

In one of the recent studies [15], it has been demonstrated that the orientation dependent anisotropic indentation modulus is similar to the isotropic indentation modulus measured using ultrasonic velocity measurements in the bulk sample. Hence, the isotropic indentation modulus of the matrix as obtained by ultrasonic measurements is used in Equation (2.51). In the present study, we propose to use the average of a few values of the k^* in every scan line to calculate the E^* of a precipitate using Equation (2.51). By doing so, every scan line is normalized for any change in the tip condition. Any change in the tip shape can be sensed in the measurement and can be

circumvented in the final modulus map. This is clearly demonstrated by a measurement on δ precipitate in alloy 625, where the tip changed during the scan.

In the as polished condition, the grain boundaries and precipitates were visible in the AFM tapping mode image owing to a slight topographic difference (< 10nm) for the precipitates and the matrix (Figure 5.2 (a)). The topography of the δ precipitate selected for AFAM study is shown in Figure 5.2 (b). Care was taken to select the area with few topographic variations.

Figures 5.2 (c) and (d) show the frequency maps of the first and the second contact resonances, respectively. The contact resonance frequencies were lower at the start of the scan as compared to the values towards the end of the scan. A sudden increase in resonance frequency values is observed at point E, indicating increase in the tip contact area (/tip radius). Figure 5.2 (e) and (f) shows typical first contact resonance curves for the matrix and the precipitate before and after the change in the tip condition. It can be clearly seen that the δ-precipitate exhibits higher contact resonance as compared to the matrix. This indicates higher indentation modulus of the δ-precipitate as compared to the matrix. Beyond the scan line E, i.e. after the increase in the tip radius also, the δ-precipitate exhibited higher contact resonance as compared to the matrix for the same scan line (Figure 5.2 (f)). As both the contact resonances are obtained simultaneously in the present approach, the tip conditions are same for both the resonances for any given location. Hence, the unique values of k^* were determined.

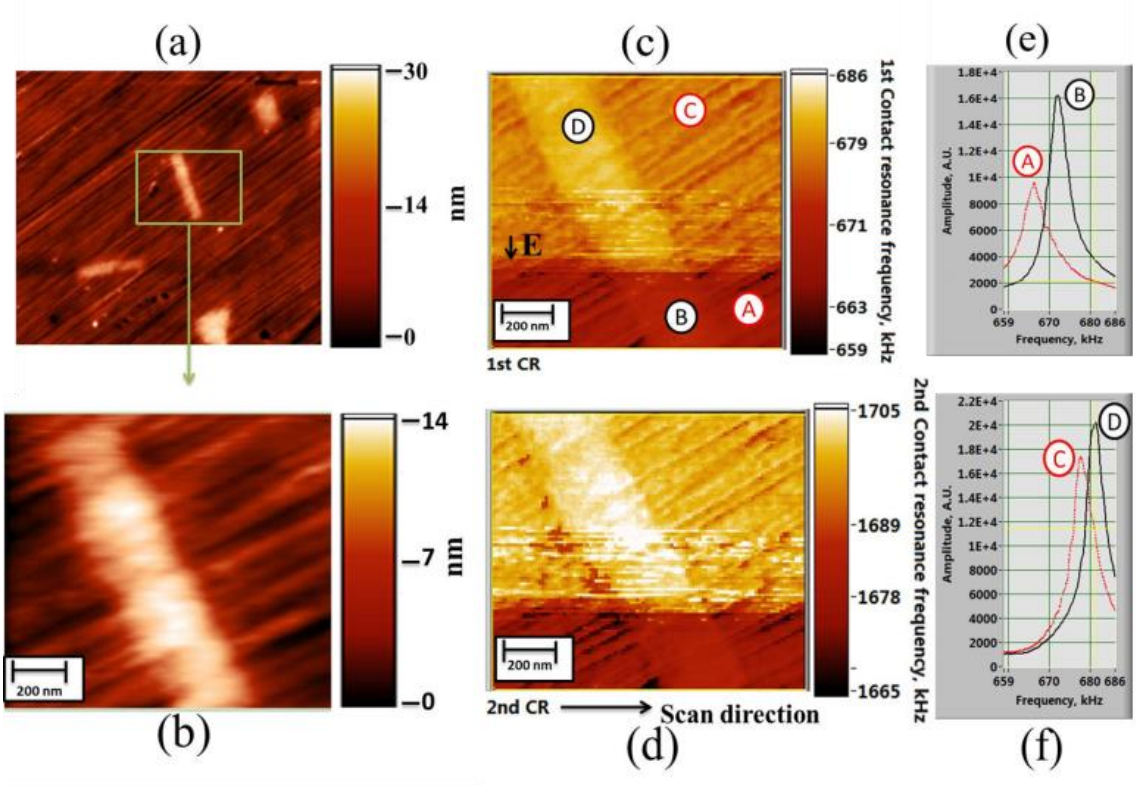

Figure 5.2: AFM tapping mode image showing topography of δ-precipitates (a); topography of the δ-precipitate selected for mapping of elastic properties (b); first (c) and second (d) contact resonance maps; first contact resonance spectra of the matrix (A and C) and the δ-precipitate (B and D) before (e) and after (f) the tip change at location E.

The effect of the increased tip radius is clearly seen in the k^* image also (Figure 5.3 (a)). As described earlier, in order to get the E^* map, the matrix modulus is used as a reference. The average of the k^* values in the last 20 data points in every scan line, as shown in Figure 5.3 (a) shown as dashed lines is used as reference for calculating the E^* values for that line. By using the reference of matrix in each line, the effect of any change in tip condition or load variation from one scan line to another is eliminated. This can be clearly seen in Figure 5.3, where the E^* map shows a uniform value for the precipitate, before and after the change in the tip condition. This demonstrates the efficacy of the methodology developed in the present study. The same methodology is used for measurement of indentation modulus of different phases present in the nickel and titanium base alloys studied in the present thesis.

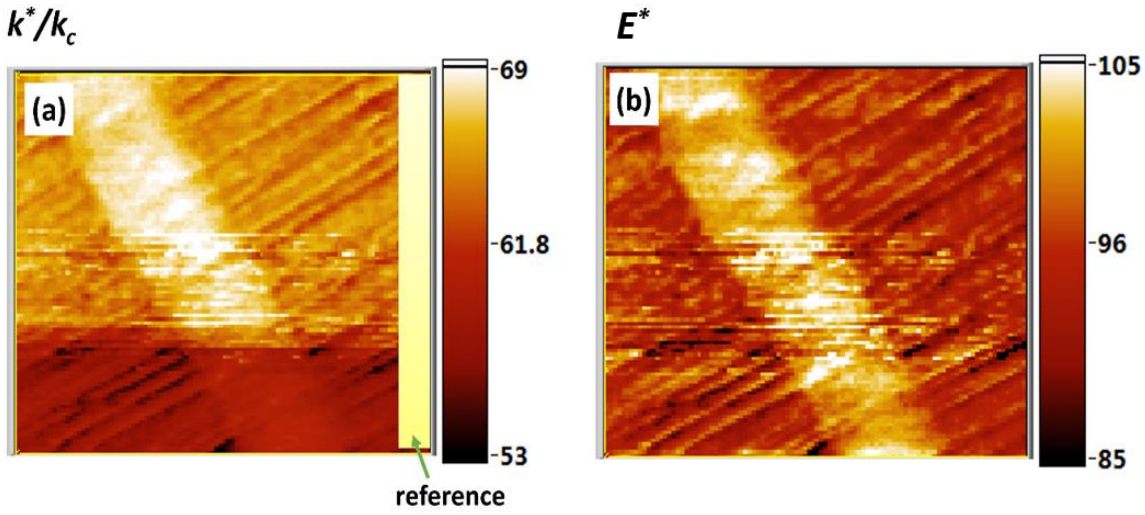

Figure 5.3: (a) k^*/k_c map, the data towards the right side of the dotted line was taken as reference and (b) E^* map of the δ-precipitate

5.3.2. Elasticity mapping in alloy 625

Figures 5.4 (a – c) show the topography maps obtained on alloy 625 samples heat treated at 1123 K for 10 h, 200 h and 500 h, respectively. Grain boundaries were found to be decorated with carbides in all the samples. These carbides were earlier identified to be of $M_{23}C_6$ type using transmission electron microscopy (TEM) [126]. The $M_{23}C_6$ carbides were reported to have orientation relationship as follows [178]: $\{001\}_{carbide} \parallel \{001\}_{matrix}$; $<100>_{carbide} \parallel <100>_{matrix.}$ In addition to carbides, needle like precipitates were found at grain boundaries as well as within the grains in specimens heat treated at 200 h and 500 h.

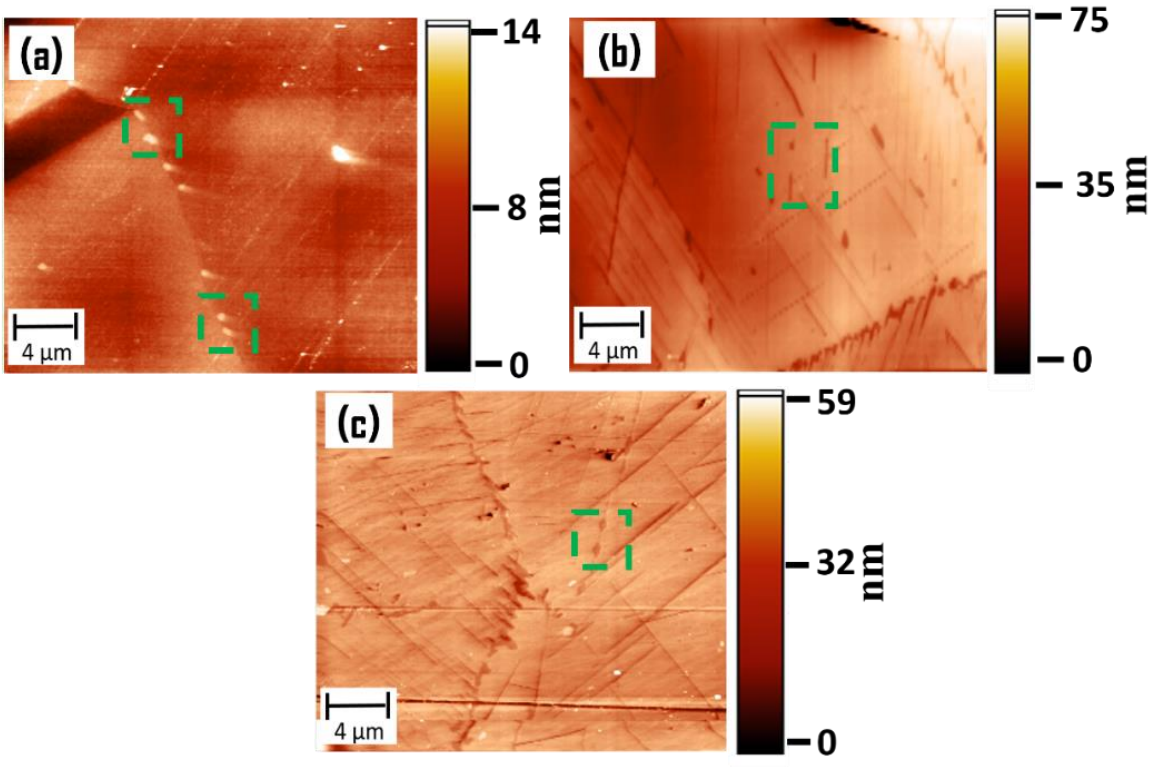

Figure 5.4: AFM topographies of alloy 625 samples service exposed at 873 K for 60000 h followed by post service heat treatment at (a) 1123 K + 10 h, (b) 1123 K+ 200 h and (c) 1123 K + 500 h (Green boxes in the above figures represent areas selected for AFAM studies)

In order to identify the precipitates, SEM and EDX maps were obtained on alloy 625 sample, heat treated at 1123 K for 200 h. Figure 5.5 (a) shows the secondary electron (SE) image of alloy 625 in which two kinds of precipitates can be visualized: precipitates with high aspect ratio (needle like) and the precipitates with low aspect ratio. To find the elemental compositions of the precipitates, EDX map was obtained as shown in Figure 5.5 (b to e). From EDX maps, it is observed that the elongated precipitates were rich in Nb and Mo, and slight reduction in Ni content as compared to the matrix is observed in the precipitates. Based on the chemical analysis, these elongated precipitates are identified as Ni_3(Nb, Mo) i.e. δ precipitates. The round/low aspect ratio precipitates are found to be rich in Mo, Nb and C and large reduction in Ni content is observed for these precipitates. These precipitates are identified as MC type carbides rich in (Mo and Nb). The

low aspect ratio precipitates of $M_{23}C_6$ and elongated precipitates of δ were also observed along the grain boundaries.

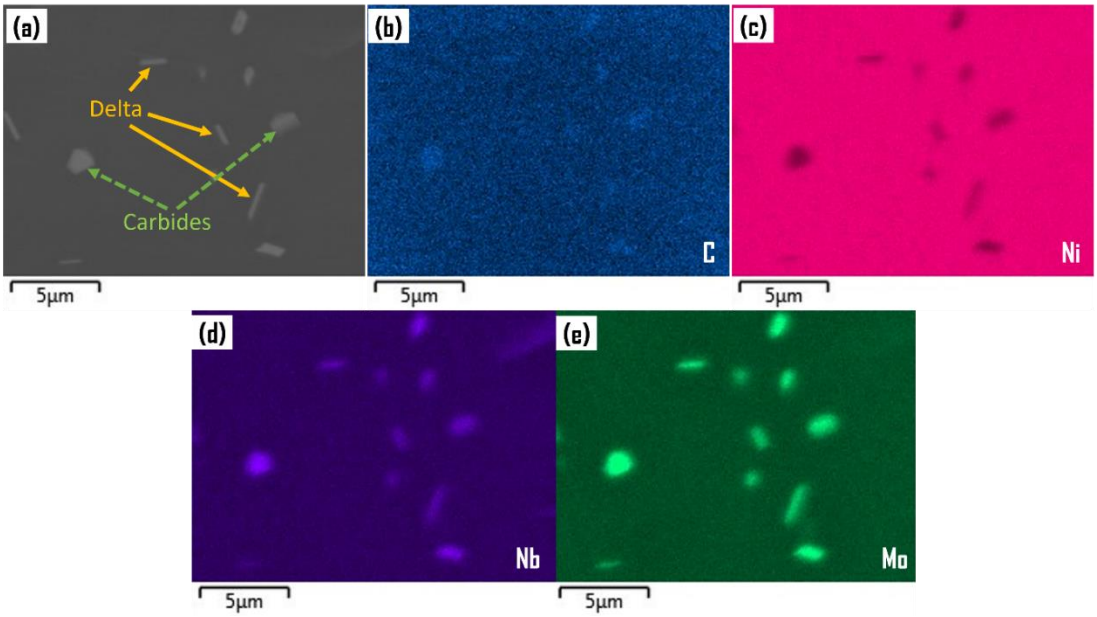

Figure 5.5: (a) SEM micrograph and EDX maps corresponding to (b) C, (c) Ni, (d) Nb and (e) Mo obtained on alloy 625 sample heat treated at 1123 K for 200 h. Precipitates with high and low aspect ratios are marked in (a)

Typical AFM topography of alloy 625 sample heat treated at 1123 K for 200 h and the corresponding first CRF map are shown in Figures 5.6 (a and b), respectively. Figure 5.6 (a) is a topography image and (b) is the corresponding CRF map of that particular area. Plane corrections are applied in AFM topography image to visualize small topography variations. The shadows in (a) are due to artefacts generated due to plane corrections. The precipitates are identified as δ (B) and carbide (C) based on their morphology. CR spectra were obtained with a scan step size of 50 nm. Typical CR spectra for the matrix and the precipitates are shown in Figure 5.6 (c). Carbides exhibited the highest CRF value followed by the δ precipitate and the matrix, respectively. This clearly shows that the carbide has higher stiffness than the δ and the matrix.

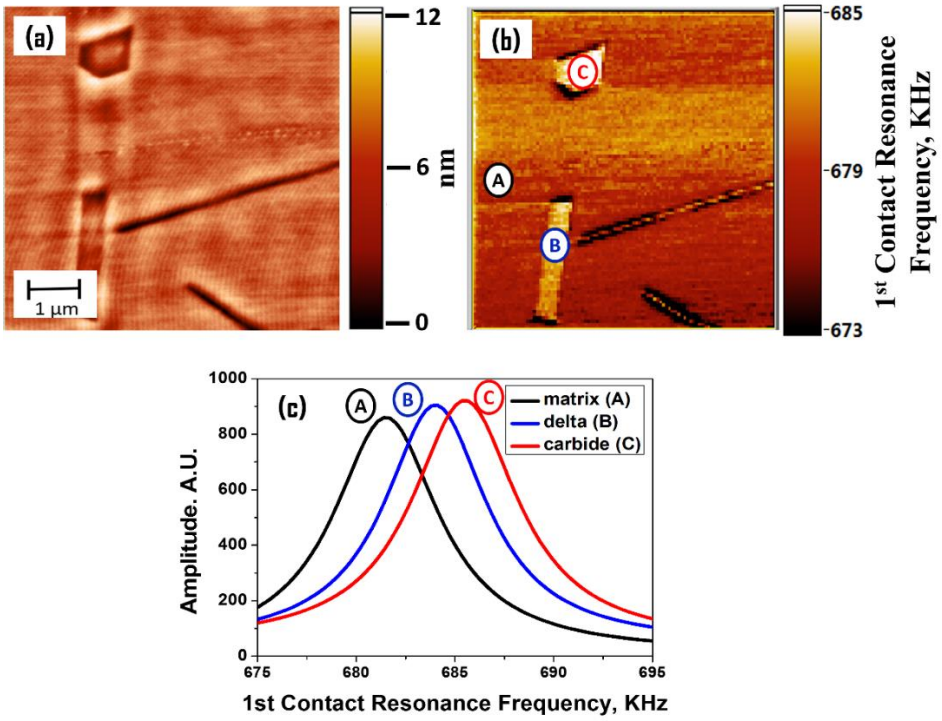

Figure 5.6: (a) AFM topography, (b) 1st CRF map and (c) the typical resonance spectra for various precipitates present in alloy 625 heat treated at 1123 K for 200 h.

The first and second CRF maps were obtained for various samples similar to Figure 5.6 (b). The k^* maps were then obtained from these CRF maps using equation (2.36). Subsequently, the indentation modulus maps were obtained by using equations (2.47-2.50) and the matrix as reference in every scan line as described in section 5.3.1. The isotropic indentation modulus of the matrix (222 ± 2 GPa) was obtained by the ultrasonic velocity measurements in the solution annealed specimen using the following equation [159]:

$$M_{iso} = \frac{\rho V_L^2 (1+\upsilon)(1-2\upsilon)}{(1-\upsilon)(1+\upsilon^2)} \tag{5.1}$$

and

$$\upsilon = \frac{V_L^2 - 2V_T^2}{V_L^2 - V_T^2} \tag{5.2}$$

where, ρ, V_L, V_T and ν are density, longitudinal wave velocity, shear wave velocity and Poisson's ratio, respectively.

Slight variation in the modulus of the matrix due to depletion of alloying elements upon precipitation is ignored. It is established that isotropic indentation modulus measured in polycrystalline specimens using ultrasonic velocity measurements do not vary much with the anisotropic indentation modulus measured on different crystallographic planes [15]. Further, due to the close packed orientation relationship between the matrix and the precipitates, as discussed earlier, using isotropic indentation modulus of the matrix as a reference would lead to isotropic indentation modulus of the precipitates, irrespective of the grain orientations in which the measurement is carried out.

Figures 5.7 (a & c) show the AFM topography images of the precipitates formed in alloy 625 specimens heat treated at 1123 K for 10 h. Carbides and δ precipitates were found at the grain boundaries and are marked in Figures 5.7 (a and c). It can be seen in Figures 5.7 (b and d) that the indentation modulus of the matrix, δ-precipitate and carbides are in the order of $M_{matrix} < M_{\delta} < M_{carbides}$ and their mean values are 222±2 GPa, 268 ± 12 GPa and 282 ± 18 GPa, respectively. Figures 5.7 (e & f) show the AFM topography and modulus map for the alloy 625 specimen heat treated for 200 h. Volume fraction of δ precipitate increased as compared to the sample heat treated for 10 h. The cross lines visible in the AFM topography (Figure 5.7 (a)) and also in indentation modulus map (Figure 5.7 (b)) depicts for different orientations of δ precipitate in the alloy sample. The indentation modulus calculated are found to be 272 ± 13 GPa and 284 ± 11 GPa for the δ precipitate and carbides, respectively.

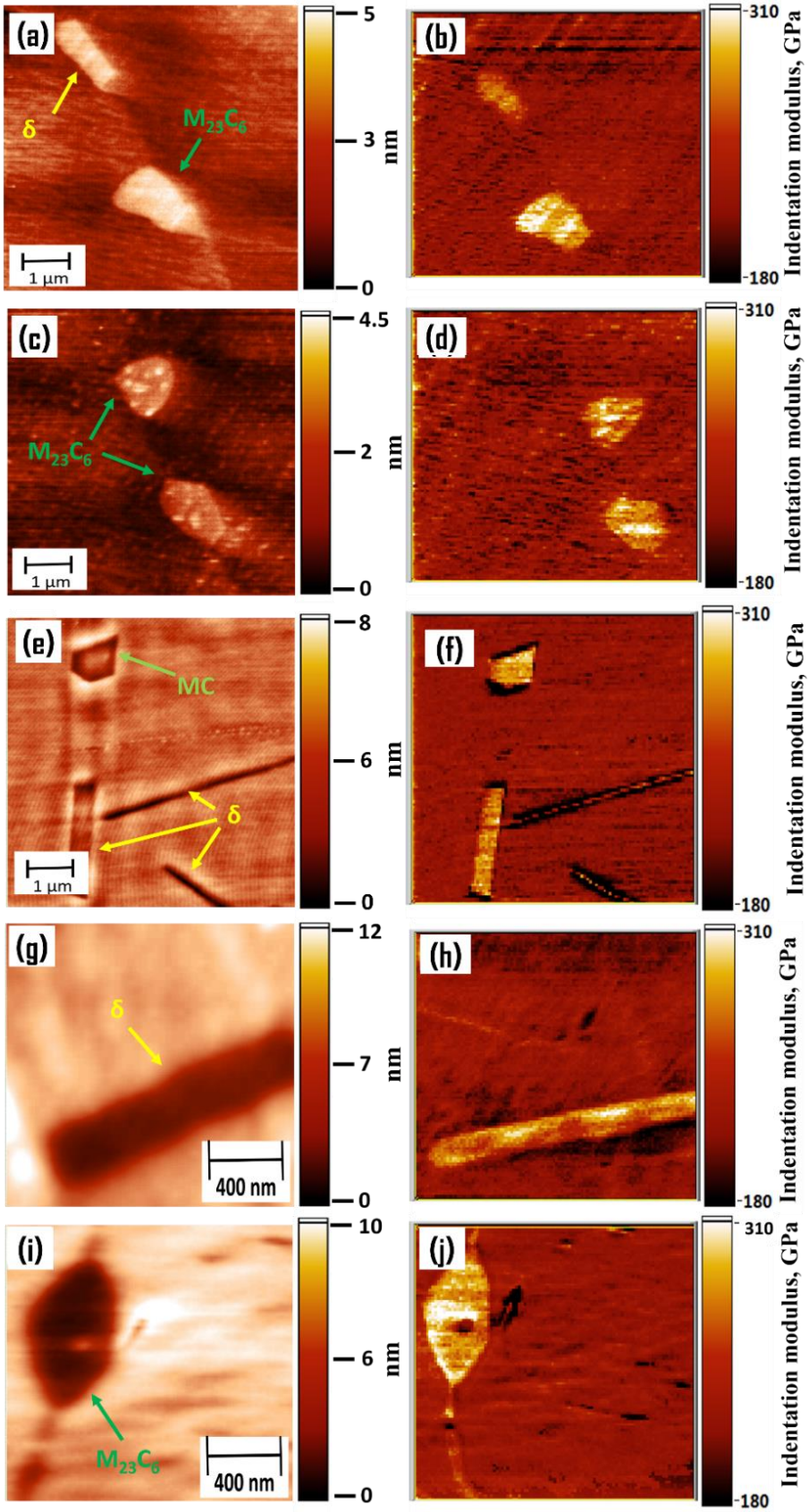

Figure 5.7: (a, c, e, g & i) AFM topographies and (b, d, f, h & j) corresponding modulus maps for an alloy 625 sample post service heat treated at 1123 K for (a to d) 10 h, (e & f) 200 h and (g to j) 500 h, followed by water quenching.

The volume fraction and size of δ precipitates were found to increase further with increased ageing durations beyond 200 h (Figure 5.7 (g)). The Indentation modulus of δ and $M_{23}C_6$ precipitates were found to be 271 ± 17 GPa and 282 ± 14 GPa, respectively. The indentation modulus values of the precipitates obtained in the samples thermally aged at 1123 K for different durations are shown in Table 5.1. Irrespective of the aging time, the δ phase exhibited similar modulus values for all the alloy 625 samples.

The indentation modulus (M) value for the δ-precipitate was found to be 280±15 GPa (Figure 5.3 (b)). Several other measurements on δ-precipitates with different orientations in different grains exhibited the indentation modulus value as 285±25 GPa. This is in close agreement with the calculated values reported [28, 29] for the Ni_3Nb with DO_a structure. Dai et al. [28] and Yong et al. [29] have theoretically calculated the elastic properties of δ-phase based on the first-principle studies. They reported the values of Young's modulus and Poisson's ratio for Ni_3Nb with DO_a structure to be in a range of 250-270 GPa and 0.33-0.35, respectively. To the best of the author's knowledge, the experimental value of elastic properties of δ-phase (Ni_3Nb with DO_a structure) has not been reported so far in literature.

It can be observed from Table 5.1 that the indentation modulus values obtained for δ precipitates are similar in these samples even though the measurements would have been performed in different grain orientations. This confirms that using isotropic indentation modulus of matrix as reference provides isotropic indentation modulus of the precipitates irrespective of the grain orientation in case of closed packed matrix and precipitate orientation relationships. Carbides show higher modulus than δ precipitate in all the alloy 625 samples. The error bar in the modulus data indicates the standard deviation of the *M* values of the pixels corresponding to the precipitate

(carbide or delta). The indentation modulus values of the $M_{23}C_6$ carbides are found to be in good agreement with those reported in literature based on the first principle calculations [164-168].

Table 5.1: Indentation modulus values of different phases in alloy 625 samples subjected to thermal ageing for different durations at 1123 K.

Temperature (K)	Precipitate modulus (GPa)		
	Carbide	**δ**	**matrix (γ) phase used as reference**
1123 + 10 h	284 ± 26	268 ± 12	222 ± 2
1123 + 200 h	284 ± 11	272 ± 13	222 ± 2
1123 + 500 h	282 ± 14	271 ± 17	222 ± 2

5.3.3. Elasticity mapping of CM 247A alloy

AFM topography of the CM 247A alloy is depicted in Figure 5.8 (a). CM 247A microstructure consists of fine cuboids of γ′ phase (shown as cuboids in Figure 5.8 (a)) in the austenitic (γ) matrix, which provides high temperature strength to the alloy by obstructing the movement of dislocations [162]. Less than 2 volume % of carbides are formed in these types of alloys and the morphologies of the carbides are depicted in Figure 5.8 (b). CM 247A superalloy predominantly contains tantalum/titanium rich carbides and can get transformed to stable hafnium/tantalum carbides with thermal processing. The Hf/Ta-rich carbides are found to have a more discrete morphology and are commonly wrapped by the γ' phase [163].

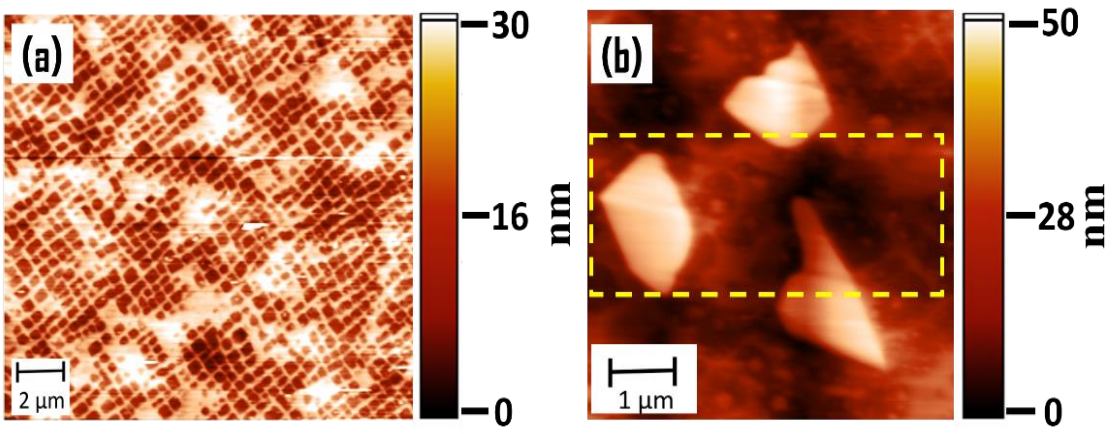

Figure 5.8: AFM topography of CM 247A supercast nickel base super alloy showing (a) γ′ (cuboids) aligned in (100) orientation and (b) carbides in γ matrix

Figure 5.9 shows the SEM and EDX maps obtained on CM 247A supercast alloy. Figure 5.9 (a) shows the SE image of the sample exhibiting fine γ′ phase distributed throughout the sample with carbides of different morphologies. EDX studies confirm that the carbides present in the alloys are of Ta, Hf and Ti rich (as shown in Figure 5.9 (d to f)) which is in agreement with the literature [163]. Nickel was found to be depleted in the carbide regions and is shown in Figure 5.9 (c).

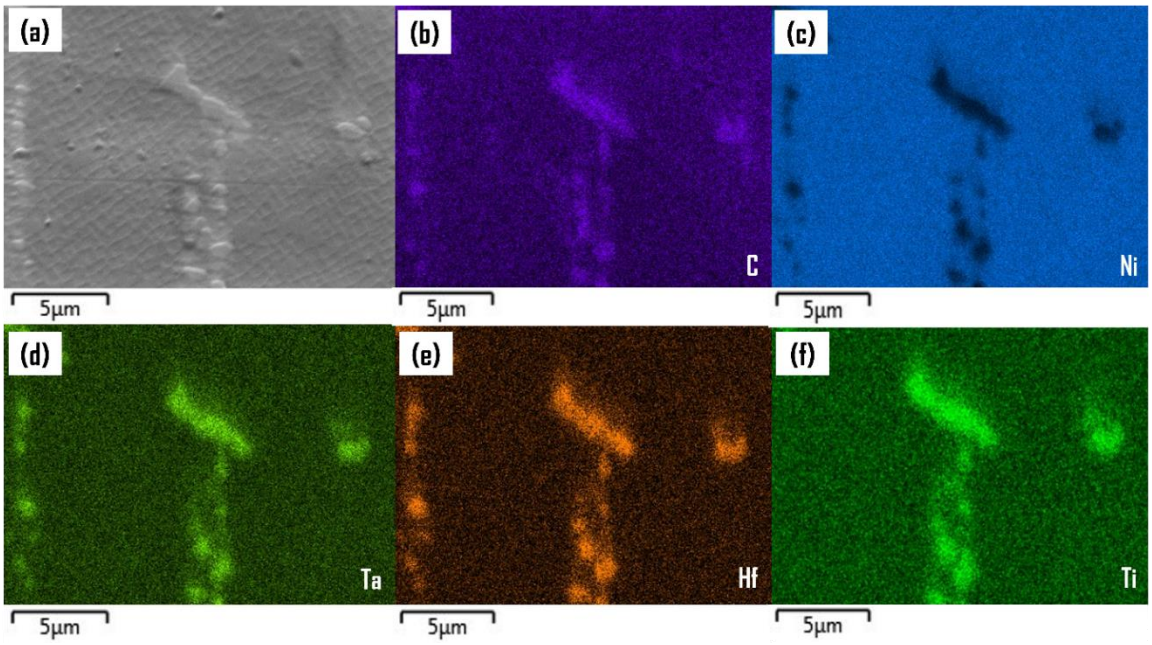

Figure 5.9: (a) SEM micrographs with (b to f) EDX maps corresponding to (b) C, (d) Ta, (e) Hf and (f) Ti obtained on CM 247A supercast alloy sample

Figures 5.10 (a and b) show the AFM topography and corresponding 1st CRF maps obtained on CM 247A alloy with different phases (γ, γ′ and carbides) present in it. The CR spectra obtained on CM 247A corresponding to γ, γ′ and carbides are shown in Figure 5.10 (c). γ′ exhibited slightly higher CRF value (~658.9 kHz), whereas, the carbides exhibited very high CRF values (~664.5 kHz) as compared to the matrix (γ) (~657.1 kHz).

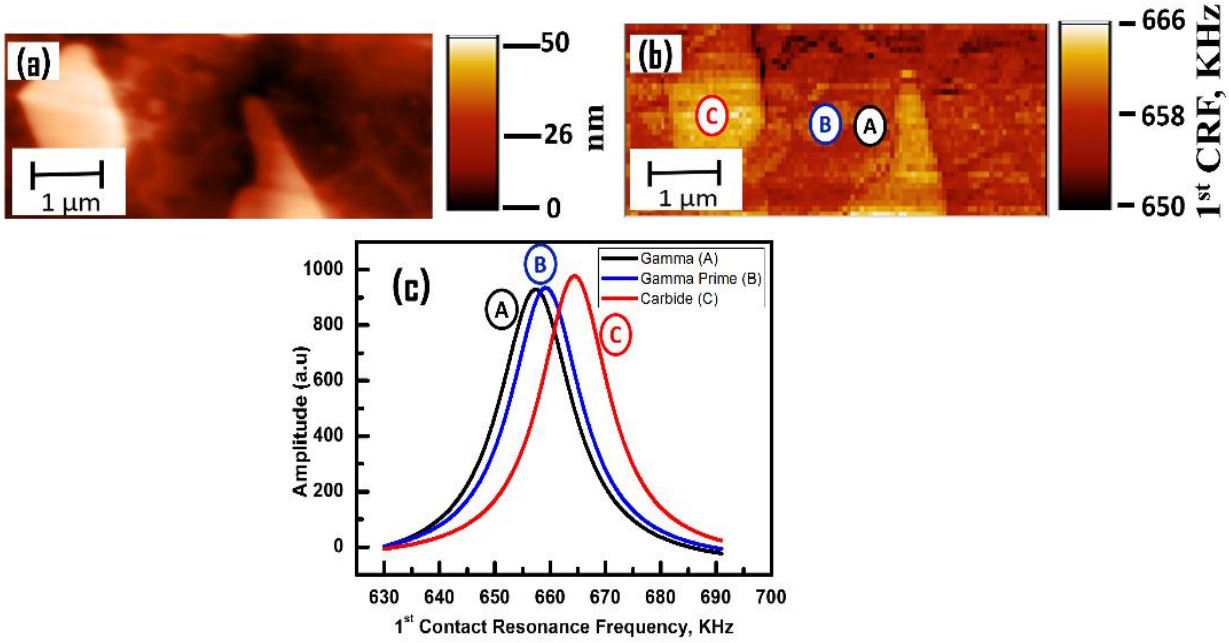

Figure 5.10: (a) AFM topography, (b) 1st CRF map and (c) typical resonance spectra shown for various precipitates present in CM 247A Supercast alloy. γ, γ′and carbides are clearly distinguished in topography, CRF map and quantitatively shown in (c)

In order to derive the indentation modulus map from the contact stiffness map, the indentation modulus of the matrix is required to be known for using as a reference. In case of alloy 625, the isotropic indentation modulus of the matrix (reference) was obtained by the ultrasonic measurements in the solution annealed sample containing only the γ phase. However, in case of alloy CM 247A, it is not possible to obtain sample with only γ phase. Ultrasonic velocity measurements were carried out on alloy CM247A sample containing γ, γ′ and carbides to measure

the elastic properties of the bulk sample with (100) orientation. The obtained longitudinal and shear velocities for CM 247A alloy are V_L = 5365 m/s and $V_{T(avg)}$ = 3872 m/s, respectively. The density was measured as 8.55 g/cc using Archimedes' principle. Poisson's ratio (ν) was calculated to be close to zero using Equation 8. Such a low Poisson's ratio value is attributed to the grain orientation in {100} direction. To compare the values, ultrasonic velocity measurements were also made in a pure nickel single crystal oriented in (100) direction. The obtained longitudinal and shear velocities for nickel single crystal oriented in (100) plane are V_L = 5325 m/s and average shear velocity $V_{T(avg)}$ = 3732 m/s. The values obtained for the single crystal and the directionally solidified superalloy are in close agreement and confirms that the γ phase is oriented in (100) plane. Substituting the ultrasonic velocities measured on (100) plane in Equations 5.1 and 5.2 essentially leads to the value of single crystal elastic constant C_{11} ($=\rho V_L^2$) as $\nu \approx 0$. For the elastic anisotropy of nickel base alloys and Ni_3Al ($2C_{44}/(C_{11}-C_{12}) \approx 3$), the value of C_{11} is close to the isotropic indentation modulus [15]. The isotropic indentation modulus of CM247A is found to be 246 GPa. The volume fractions of the γ and γ′ phases are calculated from Figure 5.8 (a) to be 42 % and 58 %, respectively. Neglecting very low volume fraction of carbides and using rule of mixture, equations (5.3) and (5.4) are obtained, as below:

$$M_{BS} = V_\gamma M_\gamma + V_{\gamma'} M_{\gamma'} \quad (5.3)$$

$$246 = 0.42 M_\gamma + 0.58 M_{\gamma'} \quad (5.4)$$

Here M_{BS}, M_γ and $M_{\gamma'}$ are the indentation modulus of bulk sample, γ phase and γ′ phase, respectively. V_γ and $V_{\gamma'}$ are volume fractions of γ and γ′ phases, respectively.

Using equation (5.4) and the relative indentation modulus values of γ and γ′ obtained from AFAM measurements (equation (2.49)), the calculated indentation modulus values of γ and γ′ are found to be 239 GPa and 251 GPa, respectively. The k^* map (Figure 5.11 (a)) was converted to E^* map by using the indentation modulus value of γ′ in every line as reference. It can be seen in Figure

5.11 that the line-to-line variation in the k^* values is removed and a uniform E^* map is obtained for individual precipitates by using the indentation modulus value of the γ′ as reference in each scan line. Further, even though γ′ exhibited only about 4% higher indentation modulus than the γ matrix, the contrast is visible for all the precipitates in the indentation modulus map (Figure 5.11 (b)). This clearly demonstrates that AFAM can be used to disclose relative elastic property of materials with high spatial resolutions, even for materials with a slight difference in elastic properties.

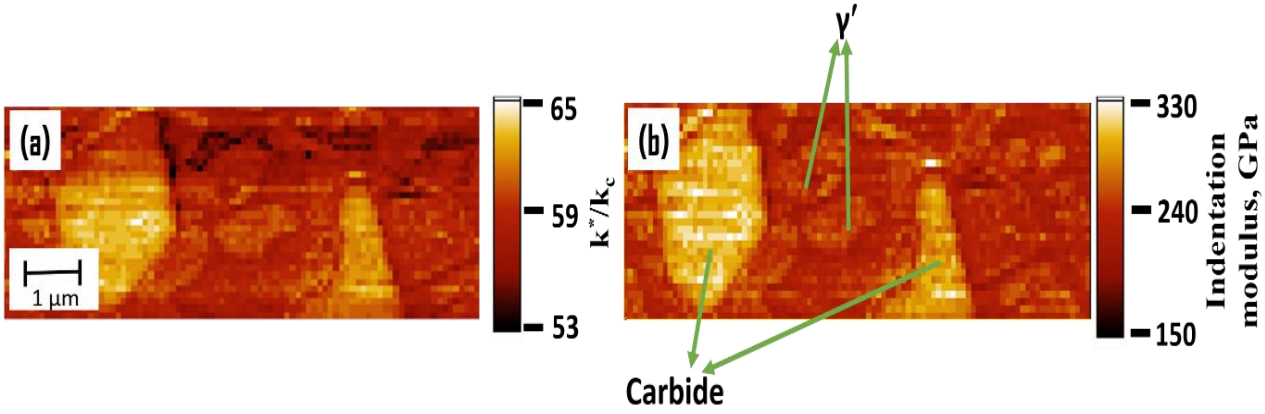

Figure 5.11: (a) Contact stiffness map (the data towards the right side (shown as yellow box) was taken as reference) and (b) indentation modulus map of the carbides present in CM 247A alloy.

The indentation modulus values for the two carbide phases are found to be 310 ± 17 GPa and 295 ± 14 GPa. Average value of these carbides is presented in Table 5.2. The experimental modulus values of γ, γ′ phases and carbides in CM 247A alloy are reported for the first time. The indentation modulus values for γ′ is found to be in good agreement with that reported based on the DFT calculations [171]. However, the values for the carbides are found to be less than that reported for TaC and HfC [174, 175]. This may be attributed to the complex chemistry of the carbides present in the alloy as observed by the EDX studies.

Table 5.2: Indentation modulus the different precipitates present in CM 247A alloy subjected to solutionizing followed by double aging treatment

Material	Precipitate modulus (GPa)		
	Carbide	**γ′**	**γ (matrix phase) used as reference**
CM 247A	304 ± 23	250 ± 10	240± 10

5.4. CONCLUSIONS

The efficacy of the new methodology developed for simultaneous acquisition of two contact resonance frequencies was demonstrated in the present study. For the first time, experimental values of elastic properties of various precipitates are mapped in two different nickel base superalloys using AFAM with the spatial resolution of better than 100 nm. The precipitates/phases present in alloy 625 and CM 247A alloy were identified using electron microscopy coupled with EDX studies. The methodologies for measurement of elastic properties of precipitates in polycrystalline and directionally solidified alloys using the indentation modulus of the matrix in each scan line as reference are described. Carbides in the alloy 625 sample are found to be MC and $M_{23}C_6$ types. In all the alloy 625 samples, these carbides exhibited higher modulus (285-290 GPa) as compared to the δ-precipitates (~270 GPa). In the directionally solidified nickel base superalloy CM247A, Ta/Hf/Ti rich MC type carbides exhibited the highest modulus (~300 GPa) and γ′ exhibited slightly higher indentation modulus (~250 GPa) as compared to the matrix γ (~240 GPa). Even though γ′ exhibited only about 4% higher indentation modulus than the γ matrix, the contrast is visible for all the precipitates in the indentation modulus map. This clearly demonstrates that AFAM can be used to disclose relative elastic property of materials with high spatial resolutions, even for materials with a slight difference in elastic properties.

MAPPING OF ELASTIC AND DAMPING PROPERTIES IN TITANIUM ALLOYS USING ATOMIC FORCE ACOUSTIC MICROSCOPY

6

6.1. INTRODUCTION

Titanium alloys are known for their wide range of applications from spectacle industries to aerospace industries due to their high specific strength and modulus, low density, excellent plasticity and ductility and intermediate temperature strength [134, 135]. Moreover, due to their excellent corrosion resistance and compatibility with human organs, titanium alloys are also widely used for human implants [135]. Depending on the stability of the various phases at room temperature, the titanium alloys are classified into three main groups such as α, α+β and β titanium alloys. Of all the titanium alloys, more than 70 % of the market value is shared by α+β titanium alloys, whereas β-titanium alloys share about 2% [139]. α+β alloys, containing a combination of α and β stabilizers, are heat treatable to various degrees. The β titanium alloys possess BCC structure. They are divided into stable β and metastable β alloys [179]. A metastable β alloy retains BCC structure upon fast quenching, however, it decomposes into β and secondary α upon aging at intermediate temperatures and hence are hardenable. Because of the good formable characteristics of the β-titanium alloys, they have achieved good appreciation in spectacle industries (eg. frames) and also in aerospace industries (eg. springs). The three most important phases such as α, β and α' can be formed in titanium alloys by varying the chemical composition and thermo-mechanical treatment conditions. By having controlled amount of the volume fractions of these phases with

suitable heat treatment, optimum mechanical properties are possible and hence best performance can be achieved.

Unlike other structural alloys, elastic properties of titanium alloys are influenced to a large extent by microstructure and alloying additions. The titanium alloys show a wide variation in the Young's modulus values ranging from 70 to 120 GPa for $\alpha+\beta$ type and it may go to as low as 14 GPa in case of stable β- titanium alloys [136, 180-182]. Various studies have been reported on the elastic properties of bulk titanium alloys using ultrasonic testing [29, 146] and resonance based techniques [183], however only a few studies are reported for measurement of elastic properties of individual phases [14].

In this chapter, the effects of chemical composition and heat treatment on elastic stiffness and damping in a β- titanium alloy and an α+β titanium alloy are studied. The modulus and damping values obtained by AFAM have been compared with that obtained by ultrasonic measurements for different specimens. Further, the influence of relative modulus of the reference and the sample on the error in the modulus measurement has also been brought out.

6.2. EXPERIMENTAL DETIALS

Four specimens each of Ti-10V-4.5Fe-1.5Al and Ti-6Al-4V alloys of dimensions about 25×25×4 mm^3 were solution-annealed at 1173 K and 1323 K (above the β – transus temperature), respectively, for 1 hour followed by water quenching. These solution-annealed specimens were then heat-treated in the $\alpha+\beta$ regime at 823 K, 923 K and 1000 K for Ti-10V-4.5Fe-1.5Al alloy and 923 K, 1123 K and 1223 K for Ti-6Al-4V alloy. The specimens were held at the corresponding temperatures for 1 hour followed by water quenching. The Ti-10V-4.5Fe-1.5Al alloy specimens heat treated (SHT) at 823 K for 1 hour exhibited very fine α phase, which could not be resolved

clearly in AFM. Hence, the specimen was given further heat treatment at the same temperature for 172 hour to increase the size of the α phase without affecting the volume fractions of the phases considerably. All the samples were prepared using conventional metallography upto 0.25 μm diamond polishing followed by 0.05 μm colloidal silica in an automatic polishing machine. The surface roughness was maintained below 3 nm RMS for all the samples.

Intermediate stiff cantilevers with spring constant, k_c, of ~ 22 N/m and the first free resonance frequency f_0 of ~ 148 kHz were used to study Ti-10V-4.5Fe-1.5Al alloy specimens. The measurements on Ti-6Al-4V alloy specimens were performed using cantilevers with a spring constant k_c of about 30 N/m and the first free resonance frequency, f_0 of about 171 KHz. The applied load on to the cantilever during acquisition was ~ 800 nN for the Ti-10V-4.5Fe-1.5Al alloy and ~ 1200 nN for the Ti-6Al-4V alloy specimens to effectively obtain the local internal friction Q^{-1}_{loc} from the sample. Caron et al. [24] have observed that a background damping in the material related to the global ultrasonic absorption is obtained at higher loads only. Hence, a slightly higher value of load was selected at which no noticeable wear of the tip and no slipping in the tip-sample contact was observed and hence uniform measurements throughout the scan were assured.

The surface topography for both the titanium alloy specimens were obtained in AFM tapping mode to select an area with sufficient flatness (less than about 10 nm) for acquiring the contact-resonance spectra, to avoid excessive damage to the tip. An area of about 5×5 μm^2 in all the specimens were selected for the AFAM measurements. A step of 50 nm was chosen and the contact resonance spectrum of the first flexural mode was acquired with a resolution of about 0.1 Hz in the range of 650 – 850 kHz.

The contact-resonance spectra were analyzed using a software specifically developed in LabVIEW to obtain the maps of the indentation modulus and damping. The indentation modulus of the individual phases obtained by AFAM measurements was used to estimate the average modulus of the specimens, using the volume fractions of the phases present in the specimens. The volume fractions of the phases were estimated using JMatPro® [184, 185] simulation software.

6.3. RESULTS AND DISCUSSIONS

Microstructure and AFM topography for Ti-6Al-4V and Ti-10V-4.5Fe-1.5Al alloy are discussed in detail in section 6.3.1. Stiffness and damping measurements carried out on Ti-10V-4.5Fe-1.5Al alloy and Ti-6Al-4V alloy are given in section 6.3.2. Modulus and damping measurements carried out using ultrasonics on bulk samples are also discussed in this section. The error in the values obtained for on local and bulk elastic properties have been understood in this section.

6.3.1. Microstructure and AFM topography studies

The amount of the α and β phases present at different heat treatment temperatures in Ti-10V-4.5Fe-1.5Al alloy and Ti-6Al-4V alloy, as obtained by the JMatPro® simulation, are given in Figure 6.1 and Table 6.1. For Ti-10V-4.5Fe-1.5Al alloy, it is observed that the volume fraction of α-phase decreases with increase in temperature up to 1073 K. It can be seen in Figure 6.1 that in both the alloys, the volume fraction of β phase increases with increase in temperature and hence the β stabilizing elements in β phase decreases as the temperatures increases. The volume fractions of α phase for the β titanium alloy samples heat treated at 823 K, 923 K and 1000 K are 52 %, 26 % and 9%, respectively. The volume fraction of the β phase in Ti-6Al-4V alloy is found to be very low (6.6 %) at 923 K and it increases to 26% and 70.9% at 1123 K and 1223 K, respectively. The JMatPro® simulation predicts the β-transus temperature (BTT) for Ti-10V-4.5Fe-1.5Al alloy and Ti-6Al-4V alloy as 1070 K and 1275 K respectively, which are in good agreement with the earlier reported experimental values [29, 135, 186]. To verify the simulation results, X-Ray Diffraction

(XRD) study was performed on the specimens of the two titanium alloys heat treated at their starting temperatures i.e 823 K for Ti-10V-4.5Fe-1.5Al alloy and 923 K for Ti-6Al-4V. XRD studies on Ti-10V-4.5Fe-1.5Al alloy and Ti-6Al-4V alloys exhibited the presence of 48 % and 6.6 % of β phase in the Ti-10V-4.5Fe-1.5Al alloy SHT at 823 K and Ti-6Al-4V alloy SHT at 923 K followed by water quenching.

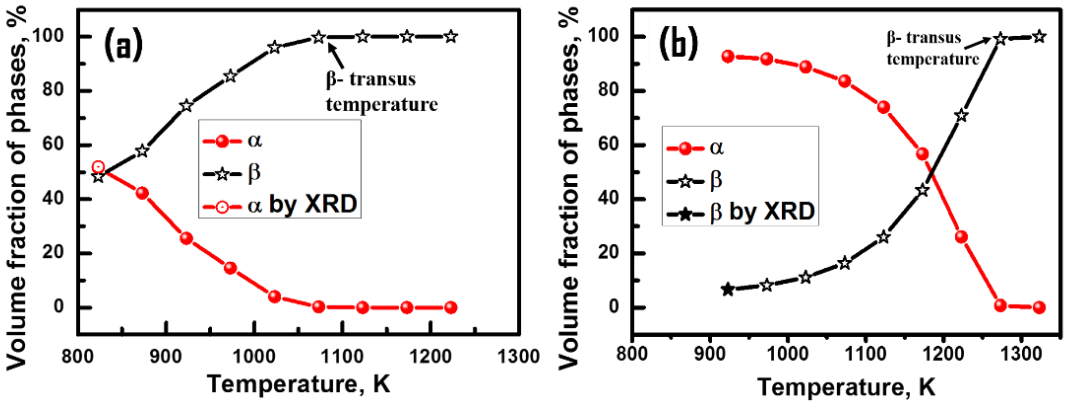

Figure 6.1: Variations in the volume fraction of α and β phases with the heat treatment temperature as obtained by the JMatPro® simulation software and XRD measurement for (a) Ti-10V-4.5Fe-1.5Al alloy and (b) Ti-6Al-4V alloy.

Typical AFM topography images obtained on Ti-10V-4.5Fe-1.5Al alloy SHT at 823 K held for 172 h and , 923 K and 1000 K held for 1 hour followed by water quenching and Ti-6Al-4V alloy specimens heat treated at 923 K, 1123 K and 1223 K for 1 hour are shown in Figure 6.2 (a to f) , respectively. Topographical variation observed for different phases upon mechanical/chemical-mechanical polishing of a sample is attributed to difference in their mechanical/chemical properties. Difference in the crystallographic orientation of the phase can also be a factor for the different topography upon polishing. The topography indicates the presence of two different phases with different heights in Ti-10V-4.5Fe-1.5Al heat treated at 823 K, 923 K and 1000 K and in Ti-6Al-4V specimens heat-treated at 923 K and 1123 K for 1 hour. In Ti-10V-4.5Fe-1.5Al alloy , the matrix exhibits more height (brighter in Figure 6.2 (a to c)) as compared to the precipitate, where as in Ti-6Al-4V alloy, the matrix exhibited less height (darker in Figure 6.2 (d to f)) as

compared to the precipitates. This clearly indicates that the β phase exhibit high topography than the α phase in both the alloys. For the Ti-6Al-4V alloy SHT at 1223 K, the matrix is identified to be α'martensite with HCP structure, which the high temperature β phase in an $\alpha+\beta$ titanium alloy transforms to, upon quenching from temperature above about 1123 K [29, 73]. The presence of retained β along with α'matrix and primary α lath has also been reported earlier in Ti-6Al-4V alloy heat-treated at 1223 K, followed by water quenching [16, 187]. CR spectra was obtained for 100 x 100 data points for a given area marked as yellow boxes in Figure 6.2 (a to f) with step size less than 50 nm.

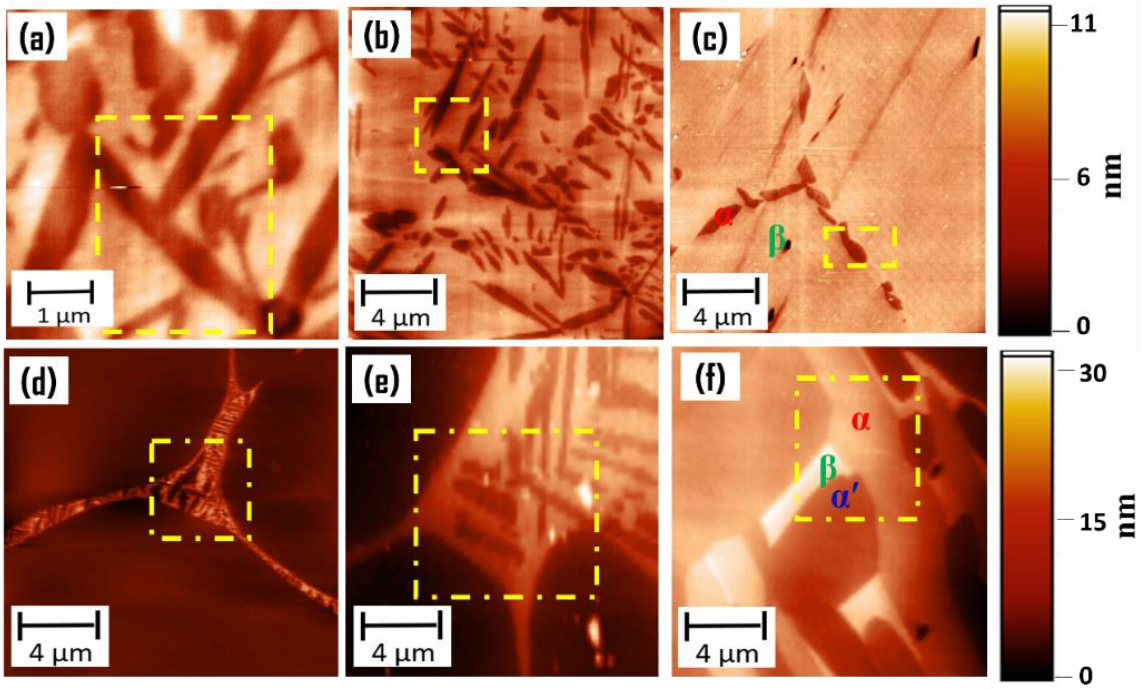

Figure 6.2: (a-c) Topography of Ti-10V-4.5Fe-1.5Al alloy at (a) 823 K for 172 hour, (b) 923 K for 1 hour and (c) 1000 K for 1 hour followed by water quenching and (d-f) topography of Ti-6Al-4V specimen heat treated at (d) 923 K, (e) 1123 K and (f) 1223 K for 1 hour followed by water quenching. Contact resonance spectra are obtained for the regions marked as yellow boxes in Figure 6.2 (a- f)

Electron microscopy studies

In order to identify various phases present in the Ti-6Al-4V specimen heat treated at 1223 K for 1 hour, an electron back-scatter diffraction (EBSD) study was performed using a Zeiss SUPRA 55 Gemini field emission gun (FEG) scanning electron microscope (SEM) at an

accelerating voltage of 20 kV, an aperture of 120 μm, a working distance of 16 mm, a tilt angle of 70 deg and the specimen–detector distance of 178 mm. An indexing algorithm based on eight detected bands was utilized.

In order to unambiguously identify these phases in the SHT at 1123 K for 1hour, SEM and EBSD studies were carried out on this specimen. Figure 6.3 (a) shows the topography image obtained using a Forward Scattering Detector (FSD) in the FEG-SEM. The topography image indicates the presence of three different phases viz., the matrix with the low topography, a lath-like phase with intermediate height and a bright phase at the boundary. The EBSD analysis indicates that both the matrix and the lath like phase with intermediate height are of HCP structure, whereas, the phase at the boundary is of BCC structure. This can clearly be seen in the composite image shown in Figure 6.3 (b), which consists of an inverse pole figure map along with the band contrast for the HCP phases and the BCC phase is shown in red. The matrix is identified as α' martensite with HCP structure, which the high temperature β phase in an α+β titanium alloy transforms to, upon quenching from temperature above about 1123 K [29]. The presence of untransformed β along with α' matrix and α lath has also been reported by Pederson [187] in Ti-6Al-4V alloy heat-treated at 1223 K and followed by water quenching. With the help of the EBSD analysis, it becomes clear that the matrix in Figure 6.2 (f) is α' martensite and the two phases with intermediate and high topography are the α and β phases, respectively.

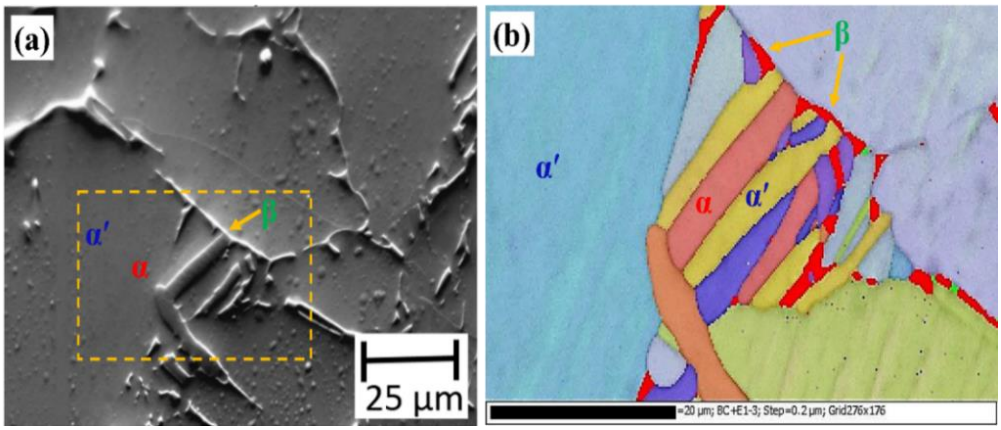

Figure 6.3: (a) Topography image and (b) a EBSD composite image showing typical microstructure in a Ti-6Al-4V specimen heat treated at 1223 K for one hour followed by water quenching. The topography image is obtained by a forward scattering detector in a FEG-SEM. The composite image consists of inverse pole figure maps along with band contrast for the HCP (*α* and *α′*) phases and the BCC (*β*) phase is shown in red.

6.3.2. Stiffness and damping studies in titanium alloys

Figure 6.4 (a) shows the 1st CRF map for the Ti-10V-4.5Fe-1.5Al *β* - titanium alloy SHT at 1000 K. The *α* phase shows, higher CRF than the *β* phase and is also quantitatively shown in Figure 6.4 (b). The observed 1st CRF values for the *β* and *α* phases are found to be 725 kHz and 732 kHz, respectively.

A map of the peak frequency in the first CR spectra for the Ti-6Al-4V alloy SHT at 1223 K is shown in Figure 6.4 (c). The presence of three phases with different contact-resonance frequencies can be clearly seen in Figure 4 (c). Figure 4d shows the typical CR spectra for the three phases. The *α′* matrix phase exhibits an intermediate value of the CRF as 774.4 kHz, whereas, the *α* lath and the retained *β* exhibit the highest and the lowest CRF values of 777.6 and 770.4 kHz, respectively. This indicates that the *α*-phase has the highest modulus followed by *α′* and *β* phases, respectively. The absolute CRF values for the two alloys cannot be compared in Figure 6.4 as it depends on the tip condition and the cantilever stiffness which are not the same for both the cases.

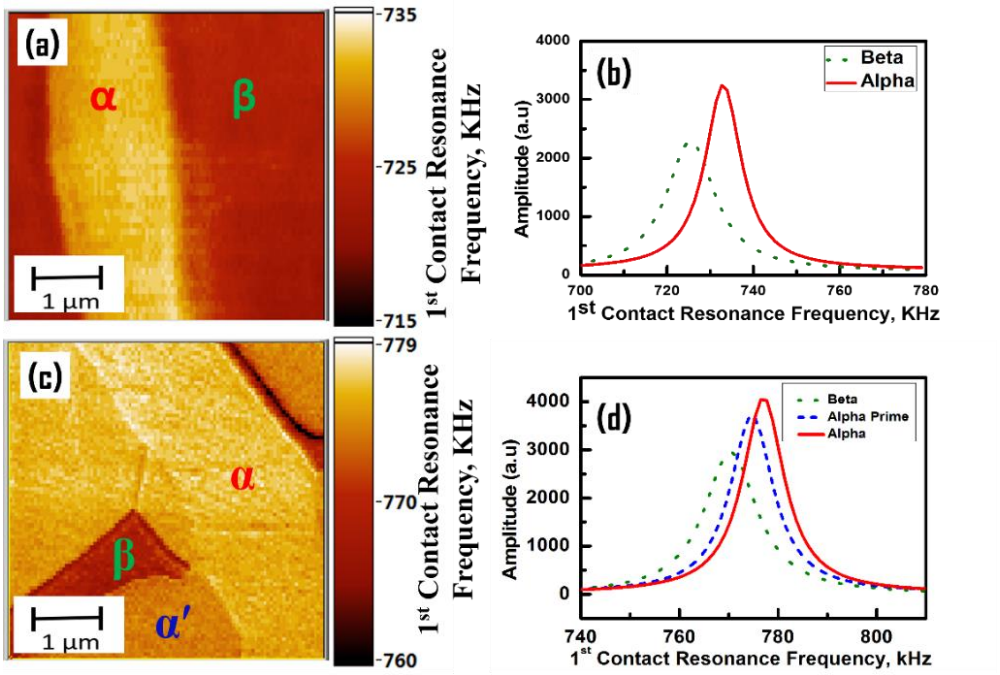

Figure 6.4: (a and c) First CRF map for a Ti-10V-4.5Fe-1.5Al β - titanium alloy and Ti-6Al-4V specimen heat-treated at 1223 K for 1 h followed by water quenching and (b and d) the typical resonance spectra for the two different phases identified as α and β in (a) and three different phases identified as α, β, and α' in (e) respectively.

The higher modulus for α phase as compared to the β phase is in agreement with the values reported based on ultrasonic velocity measurements on bulk Ti-10V-4.5Fe-1.5Al alloy and Ti-6Al-4V SHT at different temperatures [29, 146]. Tables 6.1 and 6.2 summarizes the elastic properties and ultrasonic attenuation values obtained in the bulk Ti-10V-4.5Fe-1.5Al β - titanium alloy SHT in the range of 823 K to 1173 K and Ti-6Al-4V alloy SHT in the range of 923 K to 1323 K. The modulus was found to be the highest in the Ti-10V-4.5Fe-1.5Al alloy SHT at 823 K and Ti-6Al-4V alloy SHT at 923 K having the maximum volume fractions of the α phase for the heat treatment temperatures studied in the two alloys. The attenuation was found to be highest in Ti-10V-4.5Fe-1.5Al alloy and Ti-6Al-4V alloy upon heat treatment at 1173 K and 1123K, respectively, where the amount of metastable β phase was maximum. Ti-10V-4.5Fe-1.5Al alloy SHT at 1173 K consists of a single microstructure (i.e. β phase). Similarly, the Ti-6Al-4V SHT at 1323 K is comprised of a single phase, α' martensite microstructure. Hence, ultrasonic

measurements on these two samples have been used to obtain isotropic indentation modulus of the β phase in Ti-10V-4.5Fe-1.5Al alloy and α' phase in Ti-6Al-4V alloy. Kumar et al. [15] reported that the isotropic indentation modulus obtained with the bulk measurements does not vary much with the anisotropic modulus measured on different crystallographic planes. Using a similar approach, the isotropic indentation modulus of the β and α' phases are used as reference for obtaining the indentation modulus of the other phases in the present study. The *M* value for the β phase in Ti-10V-4.5Fe-1.5Al alloy SHT at 1173 K as determined by the ultrasonic velocity measurements is 98.5 GPa [146] and *M* value for the α' phase in Ti-6Al-4V alloy SHT at 1323 K is 127.8 GPa [29].

Table 6.1: Elastic modulus obtained by ultrasonic velocity measurements in β-titanium alloy (Ti-10V-4.5Fe-1.5Al) bulk samples heat-treated at different temperatures. The volume fractions of various phases are obtained using JMatPro® simulation software.

Temperature [K]	Volume fraction (%) obtained from JMatPro® simulation		Ultrasonic measurements on bulk sample (BS) [146]			
	α	β	E_{BS} [GPa]	Ultrasonic attenuation [dB/mm]	Poisson's ratio (ν)	M_{BS} [GPa]
823	52	48	113	0.23	0.335	132.7
923	26	74	100	0.49	0.350	130
1000	9	91	87.5	0.68	0.36	128.8
1173	0	100	85	0.68	0.371	98.5 (ref)

Table 6.2: Elastic modulus obtained by ultrasonic velocity measurements in α+β titanium alloy (Ti-6Al-4V) bulk samples heat- treated at different temperatures. (*): The volume fraction of the retained β-phase given is approximate, based on the AFM and SEM microstructure. The volume fraction of the α' phase is calculated based on the difference in the volume fraction of the β-phase estimated by the JMatPro® and the volume fraction of the retained β-phase.

Temperature [K]	Volume fraction (%) obtained from JMatPro® simulation			Ultrasonic measurements on bulk sample (BS) [29]			
	α	β	α'	E_{BS} [GPa]	Ultrasonic attenuation [dB/mm]	Poissons ratio ν	M_{BS} [GPa]
923	93.3	6.6	0	115.7	0.36	0.321	132.7
1123	74	26	0	111.5	0.42	0.326	130
1223	29	5*	66*	114	0.36	0.323	128.8
1323	0	0	100	114.5	0.38	0.323	127.8 (ref)

6.3.2.1. Stiffness and damping mapping in Ti-10V-4.5Fe-1.5Al alloy

In order to calculate the modulus of the α and β phases, the modulus value of the solution annealed (SA) sample (i.e. 1173 K) was taken as the reference. The Young's modulus (E) value for the SA sample was 85 GPa calculated from ultrasonic velocities. Using Poisson's ratio (ν) for β phase as 0.37, we get M_β as 98.5 GPa. Figures 5 (a to f) displays the modulus and damping maps in Ti-10V-4.5Fe-1.5Al alloy SHT at 1000 K, 923 K and 823 K, respectively.

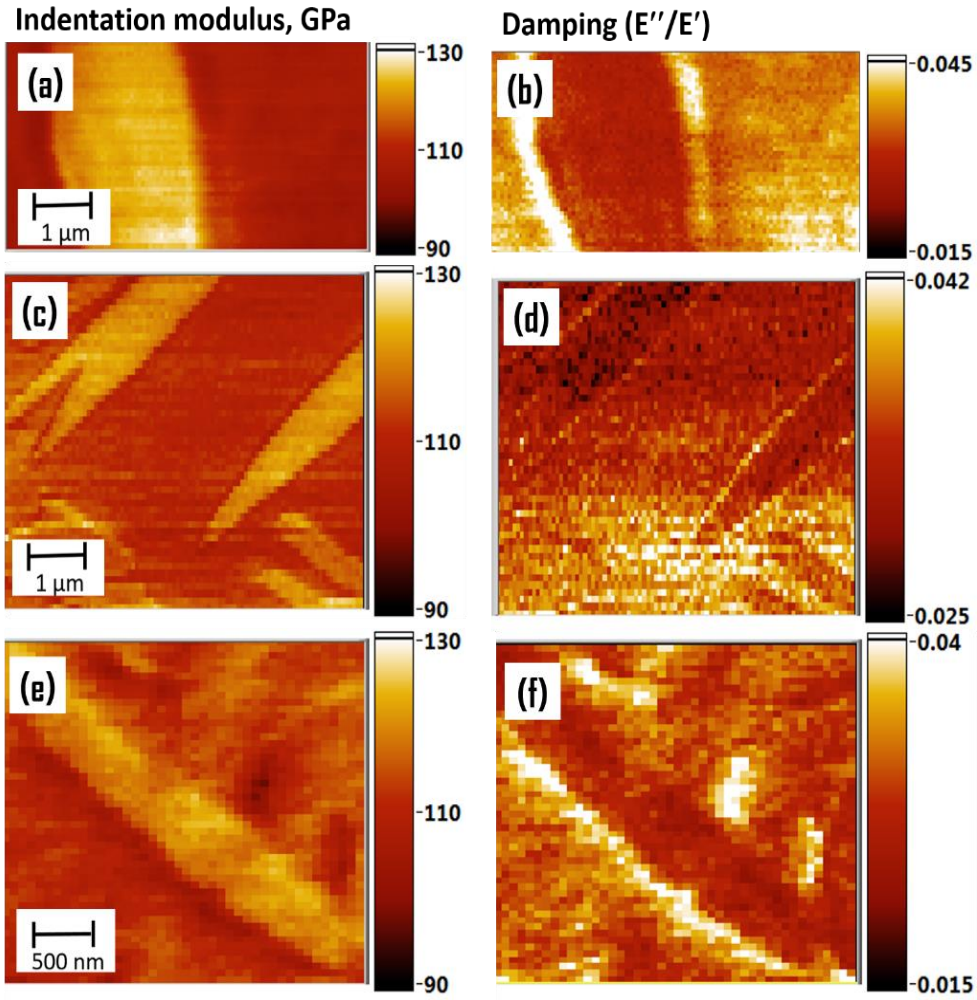

Figure 6.5: Indentation modulus and local damping maps of the Ti-10V-4.5Fe-1.5Al *β*-titanium alloy specimens heat-treated at (a & b) 1000 K for 1 hour, (c and d) 923 K for 1 hour, and (e and f) 823 K for 172 hour, followed by water quenching, respectively.

The obtained M_β value (98.5 GPa) was used as the reference to obtain the M_α in the sample heat treated at 1000 K. Due to the fact that the M_α doesn't vary much with compositional variations [29, 135], M_α calculated for the SHT at 1000 K (i.e. 121 GPa) was used as the reference to calculate M_β for the SHT at 923 K and 823 K. Statistical analysis was carried out to find the average values for $M_{\alpha,\beta}$ from the AFAM data. The average modulus values obtained for the two phases are given in Table 6.3 for the specimens heat treated at different temperatures. For all the heat treated samples, *β* phase exhibited lower modulus as compared to the *α* phase, which is clearly visualized in Figure 6.5 (a, c and e). The ratio of the modulus for the two phases was found to be similar for all the heat treated samples.

The damping maps shown in Figures 6.5 (b, d and f) were obtained using equations (2.37, 2.43-2.45). In Fig 5 (b), it is clear that there is an amplitude drop associated with increase in width of the resonance curve for β phase, attributing to the higher damping. In all the heat treated samples of Ti-10V-4.5Fe-1.5Al alloy, β exhibited higher damping than the α phase.

Table 6.3: AFAM measurements obtained for the individual phases present in Ti-10V-4.5Fe-1.5Al alloy SHT at different temperatures. The Poisson's ratios are ν_α = 0.34 and ν_β = 0.37.

Temperature [K]	AFAM measurements						
	M_α [GPa]	M_β [GPa]	E_α [GPa]	E_β [GPa]	E_{BS} [GPa]	$(E''/E')_\alpha$	$(E''/E')_\beta$
823	121	113	107	98	103	0.029	0.04
923	121	111	107	96	99	0.03	0.033
1000	121	98.5	107	85	87	0.029	0.037

6.3.2.2. Stiffness and damping mapping in Ti-6Al-4V alloy

After obtaining the k_r map for Ti-6Al-4V alloy SHT at 1223 K, using the CRF data shown in Figure 6.4 (c) and equations (2.37, 2.43-2.44), a small area in the α' region was selected as the reference to obtain the indentation modulus map, as shown in Figure 6.6 (a). Statistical analysis was carried out on the data of Figure 6.6 (a) to obtain the average (mode) values of M for α (M_α) and β (M_β) phases in the SHT at 1223 K, which are found to be 133.5 GPa and 117 GPa, respectively. The three phases are labeled in the figure for better understanding. The M_α obtained for the 1223 K sample is used as the reference to get the average M_β in the other two SHT at 1123 K and 923 K.

Figure 6.6 (c) shows the modulus map for the SHT at 1123 K. Using the M_α obtained for the SHT at 1223 K as a reference in the SHT at 1123 K, the average value for M_β is obtained as 118.7 GPa. Figure 6.6 (e) shows the modulus map for the SHT at 923 K. The average value for M_β is obtained

as 120 GPa. The average modulus values obtained for different phases are given in Table 6.4, for the specimens heat treated at different temperatures. It is clearly understood from Table 6.4, that the relative difference in modulus values calculated using AFAM for the two phases is similar for all the heat treatment temperatures, similar to that observed in Ti-10V-4.5Fe-1.5Al alloy. Similar relative modulus values for the α and β phases in different samples indicates that the effect of the crystallographic orientation on AFAM measurements is very less as the measurements are performed in grains oriented randomly. This could be attributed to the orientation relationship between the two phases i.e., if the measurement is carried out in a plane parallel to the close packed planes, both the phases would show the highest modulus and in other directions both will show lower modulus.

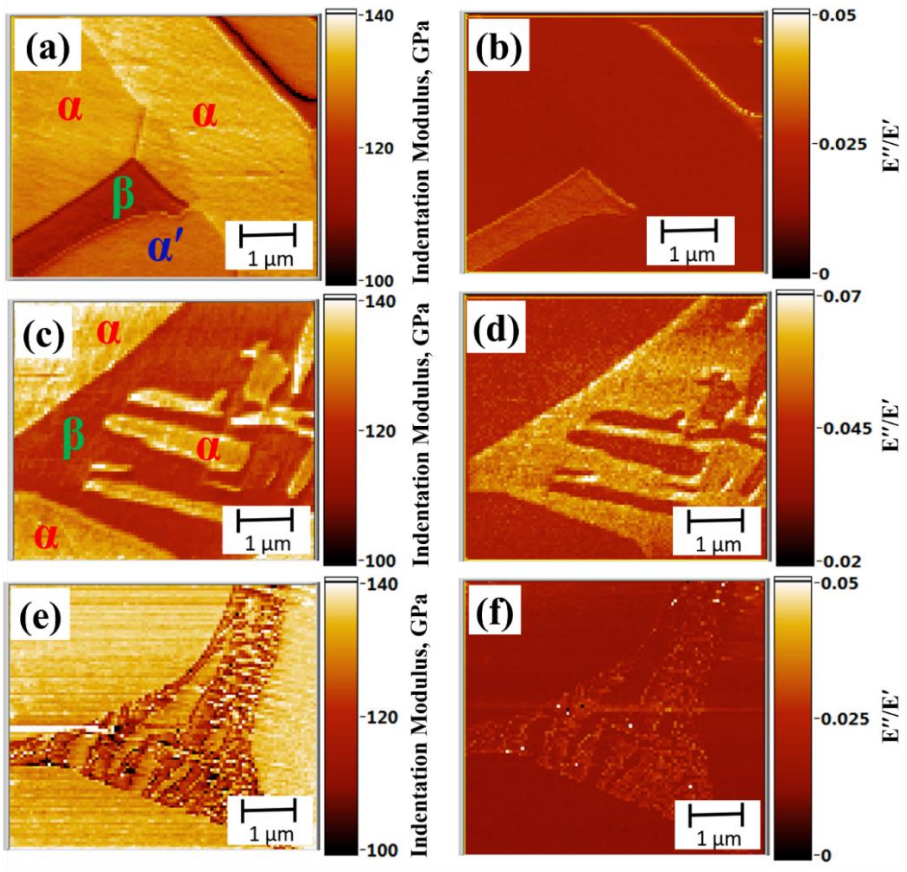

Figure 6.6: Modulus and damping maps of the Ti-6Al-4V specimens heat treated at (a and b) 1223 K, (c and d) 1123 K, and (e and f) 923 K for 1 hour, followed by water quenching, respectively.

Figures 6.6 (b, d and f) show the damping maps for specimens heat treated at 923 K, 1123 K and 1223 K. For all the three heat treated samples, the β-phase exhibited the highest damping followed by α' and α. The obtained results for damping are in line with the ultrasonic attenuation measurements carried out on bulk Ti-6Al-4V samples heat-treated at 923 K, 1123 K and 1223 K, as shown in Table 6.2 [29]. The SHT at 1123 K having the highest amount of metastable β-phase had exhibited the maximum attenuation. Even though the absolute values of the damping are not the same for the phases in the three specimens, the relative damping values for α and β phases are similar in all the three samples. The absolute values of damping in the two alloys can be compared only after having a clear idea about the parameters (tip shape, type of cantilever, load, and interaction of the tip against the surface for the applied load), which may affect the quantitative value of damping. From the obtained results, however, it is clear that for both the alloys β phase exhibited higher damping than α phase.

Table 6.4: AFAM measurements obtained for the individual phases present in Ti-6Al-4V alloy SHT at different temperatures. The Poisson's ratios are ν_α = 0.32 and ν_β = 0.33.

Temperature [K]	AFAM measurements						
	M_α [GPa]	M_β [GPa]	E_α [GPa]	E_β [GPa]	E_{BS} [GPa]	$(E''/E')_\alpha$	$(E''/E')_\beta$
923	133.5	120	119.7	106.9	119.1	0.013	0.028
1123	133.5	118.7	119.7	105.7	116.2	0.044	0.056
1223	133.5	117	119.7	104.2	115.4	0.019	0.028

Determining modulus of bulk samples using AFAM measurements

The Young's modulus (E) of the individual phases can be approximated by using *M* values for the respective phases and equation (6.1). Indentation modulus (M) values of the individual phases measured using AFAM for both the alloys heat treated at different temperatures can be

converted to E values using $M = \frac{E}{1-\vartheta^2}$, where E is Young's modulus and ϑ is Poisson's ratio. The Poisson's ratio values used for the calculations for the α and β phases in Ti-10V-4.5Fe-1.5Al and Ti-6Al-4V alloys are ν_α = 0.34 and 0.32 and for ν_β = 0.37 and 0.33, respectively. Combining all these values with the volume fractions of the individual phases, the average modulus of the samples can be calculated using rule of mixtures [16, 188]:

$$E_{BS} = E_\alpha V_\alpha + E_\beta V_\beta + E_{\alpha'} V_{\alpha'} \quad (6.1)$$

where, V_α, V_β and $V_{\alpha'}$ are the volume fractions of α, β and 6α' phases in the sample and E_{BS} is the average Young's modulus of the bulk sample. Equation 6.1 can be used to calculate the modulus values for bulk Ti-10V-4.5Fe-1.5Al and Ti-6Al-4V alloys. Tables 6.3 and 6.4 summarizes the bulk elastic properties obtained using AFAM in Ti-10V-4.5Fe-1.5Al and Ti-6Al-4V alloys heat treated at different temperatures.

6.3.2.3. Error analysis in AFAM measurements

Table 6.5 compares the % error in the modulus values of the bulk samples obtained by AFAM as compared to that by ultrasonic measurements for Ti-6Al-4V and Ti-10V-4.5Fe-1.5Al alloy samples heat treated at different temperatures. It can be seen in Table 6.5 that all the three specimens of Ti-10V-4.5Fe-1.5Al alloy exhibited negative error, i.e. the modulus obtained by AFAM was found to be less than that obtained by the ultrasonic velocity measurements. On the other hand, it is observed that all the three specimens of Ti-6Al-4V alloy exhibited positive error. Further, the % errors increase with the volume fraction of α phase in Ti-10V-4.5Fe-1.5Al alloy and volume fraction of β phase in Ti-6Al-4V alloy. In Ti-10V-4.5Fe-1.5Al alloy, β phase modulus (85 GPa) was used as the reference to calculate the modulus of the α phase, i.e. the reference had lower modulus than the phase for which modulus is calculated. The negative error for Ti-10V-4.5Fe-1.5Al alloy indicates that the modulus of the α phase measured by AFAM is slightly less than the real value, when a lower modulus phase is used as the reference.

Table 6.5: The percentage error values for Ti-6Al-4V and Ti-10V-4.5Fe-1.5Al β-titanium alloy samples calculated using AFAM and ultrasonic velocity measurements.

Temperature, K	Percentage error (%)	
	Ti-10V-4.5Fe-1.5Al	Ti-6Al-4V
823	- 8.8	-----
923	- 1	2.9
1000	- 0.5	-----
1123	-----	4.2
1223	------	1.2

On the other hand for Ti-6Al-4V, the modulus of α' phase having higher modulus was used as the reference to calculate the value for β phase. This led to a slightly higher modulus of the β phase. In general, the results indicate that when a phase having higher modulus is used as a reference, a slightly higher modulus value is obtained for the phase with lower modulus and vice versa, i.e. the difference in the modulus values obtained by AFAM for a sample and a reference is always less than that obtained by ultrasonic measurements for the two, as shown in equation (6.2):

$$\left|\frac{M_{sample}}{M_{Reference}} - 1\right|_{AFAM} < \left|\frac{M_{sample}}{M_{Reference}} - 1\right|_{Ultrasonic\ mesurements} \quad (6.2)$$

Similar inference can also be made from the results reported by Hurley et al. [85]. They proposed to use dual reference method with the two references having modulus values higher and lower than that of the sample to circumvent this problem. However, problem associated with change of tip conditions are expected when measuring on two different references, in addition to the sample. Since the error is systematic, it should be possible to circumvent this with suitable corrections in the dispersion curve.

6.4. CONCLUSIONS

The study reports, simultaneous mapping of local elastic and damping properties in a β and an $\alpha + \beta$ titanium alloys using AFAM. The β phase exhibited lower modulus and higher damping than α'/α phase in both the titanium alloy samples heat treated at different temperatures. The

average elastic property values calculated using AFAM are in good agreement with the bulk elastic property calculated using ultrasonic velocity measurements. The relative elastic and damping values calculated using AFAM were found to be similar for the α and β phases in specimens heat treated at different temperatures. The study demonstrated that the nanoscale elastic properties measured using AFAM can also be used for obtaining the average elastic properties of the bulk samples with accuracy. The systematic error in the elastic property measurements using single reference has also been brought out. The study also indicates that the crystallographic orientation does not affect the AFAM measurements to a large extent due to orientation relationship between the two phases.

7 SUMMARY AND SUGGESTIONS FOR FUTURE WORK

7.1. SUMMARY

The present study aimed to study the elastic properties of submicron phases/precipitates present in nickel and titanium base alloys using AFAM. Quantitative mapping of elastic properties was carried out on a polycrystalline and a directionally solidified nickel base superalloys. Simultaneous measurements of elasticity and damping was carried out in two types of titanium alloys: an $\alpha+\beta$ and a β titanium alloy. Microstructural characterization of these multiphase structural alloys was carried out by SEM, EDX and AFM. Specific softwares were developed to acquire and analyze the data obtained from AFAM system. Effect of various parameters on measurement of elastic and damping properties using AFAM was studied.

For the first time ever, elastic properties of various precipitates were mapped in polycrystalline (alloy 625) and directionally solidified (CM 247A) nickel base superalloys using AFAM with the spatial resolutions better than 100 nm. Alloy 625 sample service exposed at 873 K for 60,000 h followed by post service heat treatment at 1123 K for 10 h, 200 h and 500 h were taken for study. The precipitates present in both the alloys are identified using EBSD studies. EDX was also carried out to identify the elemental compositions of precipitates. Carbides and δ-precipitates were found in alloy 625. Carbides in the alloy 625 samples were found to be MC and $M_{23}C_6$ types. A new methodology was developed for eliminating the effect of the change in the tip condition during mapping of elastic properties using AFAM. This approach circumvents the problem of the change

in the tip condition by simultaneous acquisition of two resonance frequencies and selecting the matrix in each scan line as a reference. The described methodology also eliminates repeated switching between an unknown sample and a reference sample for quantitative measurement of indentation modulus. In all the alloy 625 samples, carbides exhibited higher modulus (285-290 GPa) as compared to the δ-precipitates (~270 GPa). The relative modulus values for all the precipitates heat treated at different temperatures and times exhibited similar modulus values. It is demonstrated that, due to the close packed orientation relationships of precipitates with the matrix, the modulus of a precipitate measured by the methodology described in this study is not affected by the orientation of individual grain in which the measurement is made.

CM 247A in double aged condition was taken for study. Microstructure of CM 247A consists of γ, γ′ and carbides, of which γ′ possesses 58 % of volume fractions and carbides of 2 %. Using the volume fractions of phases and relative modulus values of the phases obtained by AFAM measurements, the indentation modulus values of individual phases are derived. Reference from each scan line was used to obtain indentation modulus of the carbides. It is demonstrated that even slight variations in the elastic property between two phases can be reliably imaged using AFAM with good resolutions. Ta/Hf/Ti rich MC type carbides exhibited the highest modulus (~300 GPa) and γ′ exhibited slightly higher indentation modulus (~250 GPa) as compared to the matrix γ (~240 GPa).

For the first time ever, simultaneous mapping of local elastic and damping properties in titanium alloys were reported, in which a cantilever dynamics model is used that also considers damping. Two types of titanium alloys, Ti-6Al-4V, an (α+*β*) alloy and Ti-10V-4.5Fe-1.5Al, a *β*- Titanium alloy were studied. The alloys were heat treated at different temperatures to obtain specimens with different volume fractions of various phases. In Ti-6Al-4V, the phases identified were α, α′

and β, whereas only α and β phases were observed in Ti-10V-4.5Fe-1.5Al alloys. β phase exhibited minimum modulus and maximum damping followed by α′ and α phase in the titanium alloy samples heat treated at different temperatures. Using rule of mixtures, the average elastic properties of both the titanium alloys were calculated and correlated with the bulk measurements carried out by ultrasonic velocity measurements. The average elastic property values calculated using AFAM are found to be in good agreement with the bulk elastic property calculated using ultrasonic velocity measurements and the variation is found to be about 5 %. The relative elastic and damping values calculated using AFAM were found to be similar for the phases present in titanium alloys heat treated to different temperatures. A systematic error in the elastic property measurements using single reference has also been brought out. It is observed that the difference in the modulus values obtained by AFAM for a sample and a reference is always slightly less than that obtained by ultrasonic measurements for the two. The study also indicated that, the crystallographic orientation does not affect the AFAM measurements to a large extent due to orientation relationship between the two phases.

7.2. SUGGESTIONS FOR FUTURE WORK

Systematic error observed during the use of single reference can be improved by using modified CDMs. Finite element method (FEM) may be a very good solution. The tip-sample configurations used in FEM analysis, until now neglects damping. Including the damping part would help to understand the various mechanics occurring at the tip sample contact. Understanding of the dependence of damping with load is also required. Reference approach methods may pave a way to determine quantitative values of the real damping in a material.

Even though simultaneous mapping of two contact resonances have been substantiated as a good approach to get rid of the tip wear problem, an approach for getting a good clean Lorentzian linear curve for the higher modes is still unknown. Higher modes provide better resolution for stiff

materials (high k^*/k_c). Studies have to be carried out to understand the physics leading to the splitting of the resonance curves due to which rich knowledge of the elastic properties are mislaid.

Internal friction studies have to be carried out on various materials and even on various reference samples to understand the physical mechanics (energy dissipation) occurring at the contact. The energy dissipation due to tip scratching the surface at nano level must also be considered to view the exact situation of the dissipation mechanism. Better understanding of the internal friction arising at the tip sample contact can open an opportunity to understand the real contact mechanics.

Finally, AFAM can be exploited to understand mechanisms like dislocation activities etc. occurring inside a material to better understand the deformation processes occurring at the nanoscale.

REFERENCES

1. A.Kumar, T.Jayakumar, and B.Raj, *Influence of precipitation of intermetallics on Young's modulus in nickel and zirconium base alloys.* Philos. Mag. Lett., 2006. **86**(9): p. 579–587.
2. Lu, H.W., Xianping, Zhang, Tao, Cheng, Zhijun, Fang, Qianfeng, *Design, fabrication, and properties of high damping metal matrix composites—a review.* Materials, 2009. **2**(3): p. 958-977.
3. Lemons, R.A. and C.F. Quate, *Acoustic microscope—scanning version.* Appl. Phys. Lett., 1974. **24**(4): p. 163-165.
4. Ramanathan, S., J.E. Semmens, and L.W. Kessler. *High-frequency acoustic microscopy studies of buried interfaces in silicon*. in *Electronic Components and Technology Conference, 2006. Proceedings. 56th*. 2006. IEEE.
5. Oliver, W.C. and G.M. Pharr, *An improved technique for determining hardness and elastic modulus using load and displacement sensing indentation experiments.* J. Mater. Res., 1992. **7**(06): p. 1564-1583.
6. Ogi, H., Tian, Jiayong, Tada, Toyokazu, Hirao, Masahiko, *Elastic–stiffness mapping by resonance-ultrasound microscopy with isolated piezoelectric oscillator.* Appl. Phys. Lett., 2003. **83**(3): p. 464-466.
7. Hirao, M. and H. Ogi. *Resonance Ultrasound Microscopy for Imaging Young's Modulus of Solids*. in *IUTAM Symposium on Recent Advances of Acoustic Waves in Solids*. 2010. Springer.
8. Rabe, U., M. Kopycinska-Müller, and S. Hirsekorn, *Atomic Force Acoustic Microscopy*, in *Acoustic Scanning Probe Microscopy*, F. Marinello, D. Passeri, and E. Savio, Editors. 2013, Springer Berlin Heidelberg. p. 123-153.
9. Killgore, J.P., et al., *Viscoelastic property mapping with contact resonance force microscopy.* Langmuir, 2011. **27**(23): p. 13983-7.
10. Yuya, P.A., D.C. Hurley, and J.A. Turner, *Contact-resonance atomic force microscopy for viscoelasticity.* J. Appl. Phys., 2008. **104**(7): p. 074916.
11. Phani, M.K., A. Kumar, and T.Jayakumar, *Elasticity mapping of delta precipitate in alloy 625 using atomic force acoustic microscopy with a new approach to eliminate the influence of tip condition.* Phil. Mag. Lett., 2014. **94**(7): p. 395-403.
12. Rabe, U., *Atomic Force acoustic microscopy*, in *Applied Scanning Probe Methods II*, B.B. P. Avouris, K. von Klitzing, H. Sakaki, R.Wiesendanger, Editor. 2006, Springer: Heidelberg. p. 38-90.
13. Wagner, H., Bedorf, Dennis, Küchemann, Stefan, Schwabe, Moritz, Zhang, Bo, Arnold, Walter, Samwer, Konrad, *Local elastic properties of a metallic glass.* Nat Mater, 2011. **10**(6): p. 439-442.
14. Kumar, A., U. Rabe, and W. Arnold, *Mapping of Elastic Stiffness in an α+ β Titanium Alloy using Atomic Force Acoustic Microscopy.* Japan. J. Appl. Phys., 2008. **47**(7S2): p. 6077.
15. Kumar, A.R., Ute, Hirsekorn, Sigrun, Arnold, Walter, *Elasticity mapping of precipitates in polycrystalline materials using atomic force acoustic microscopy.* Appl. Phys. Lett., 2008. **92**(18): p. 183106.

16. Phani, M.K., Kumar, Anish, Jayakumar, T, Arnold, Walter, Samwer, Konrad, *Mapping of elasticity and damping in an α+ β titanium alloy through atomic force acoustic microscopy.* Beilstein J. Nanotechnol., 2015. **6**(1): p. 767-776.
17. Rabe, U., Amelio, S., Kopycinska, M., Hirsekorn, S., Kempf, M., Göken, M., Arnold, W., *Imaging and measurement of local mechanical material properties by atomic force acoustic microscopy.* Surf. Interface Anal., 2002. **33**(2): p. 65-70.
18. Joachim, L. and A.M. Alekseev, *Atomic Force Acoustic Microscopy On Polymer Materials*, in *Southern Federal University. Technical sciences*2014. p. 47-58.
19. Kos, A.B., J.P. Killgore, and D.C. Hurley, *SPRITE: a modern approach to scanning probe contact resonance imaging.* Meas. Sci. Technol. , 2014. **25**(2): p. 025405.
20. Prasad, M., Kopycinska, Malgorzata, Rabe, Ute, Arnold, Walter, *Measurement of Young's modulus of clay minerals using atomic force acoustic microscopy.* Geophys. Res. Lett., 2002. **29**(8): p. 13-1-13-4.
21. Zhou, X., Fu, Ji, Li, Yingwei, Li, Faxin, *Nanomechanical mapping of glass fiber reinforced polymer composites using atomic force acoustic microscopy.* J. Appl. Polym. Sci., 2014. **131**(2): p. 39800.
22. Caron, A., W. Arnold, and H.-J. Fecht, *On the Contribution of Friction to the Contact Damping in Atomic Force Acoustic Microscopy.* Jpn. J. Appl. Phys., 2010. **49**(12): p. 120204.
23. Wagner, H., , *Measurement of local internal friction in metallic glasses.* Journal of Applied Physics, 2014. **115**(13): p. 134307.
24. Caron, A. and W. Arnold, *Observation of local internal friction and plasticity onset in nanocrystalline nickel by atomic force acoustic microscopy.* Acta Mater., 2009. **57**(15): p. 4353-4363.
25. Wagner, H., Büchsenschütz-Göbeler, M., Luo, Y., Kumar, A., Arnold, W. Samwer, K.,, *Measurement of local internal friction in metallic glasses.* J. Appl. Phys., 2014. **115**(13): p. 134307.
26. Ciccotti, M. and F. Mulargia, *Differences between static and dynamic elastic moduli of a typical seismogenic rock.* Geophys. J. Int., 2004. **157**(1): p. 474-477.
27. Schubert, G., *Treatise on Geophysics*. 2, revised ed. 2015: Elsevier Science.
28. Migliori, A., Sarrao, JL, Visscher, William M, Bell, TM, Lei, Ming, Fisk, Z, Leisure, RG, *Resonant ultrasound spectroscopic techniques for measurement of the elastic moduli of solids.* Physica B: Condensed Matter, 1993. **183**(1): p. 1-24.
29. Kumar, A., *Correlation of Microstructure and Mechanical Properties with Ultrasonic Parameters in Metallic Materials* in *Metallurgical and Materials Engineering*2003, Indian Institute of Technology: Kharagpur, India. p. 42-43.
30. Ogi, H., H. Niho, and M. Hirao, *Internal-friction mapping on solids by resonance ultrasound microscopy.* Appl.Phys.Lett., 2006. **88**(14): p. 141110.
31. Quate, C.F., *The AFM as a tool for surface imaging.* Surf. Sci. , 1994. **299–300**: p. 980-995.
32. Giessibl, F.J., *Advances in atomic force microscopy.* Rev. Mod. Phys., 2003. **75**(3): p. 949-983.
33. Yaxin Song and B. Bhushan, *Atomic force microscopy dynamic modes: modeling and applications.* J. Phys. Condens. Matter, 2008. **20**(22): p. 225012.
34. *Atomic force microscopy*. Available from: http://www.nanoscience.de/nanojoom/index.php/en/methods/afm.html.
35. Baym, G., *Lectures on Quantum Mechanics*. 1969: W. A. Benjamin.
36. Bhushan, B., *Springer Handbook of Nanotechnology*. 2007: Springer Berlin Heidelberg.
37. Cappella, B. and G. Dietler, *Force-distance curves by atomic force microscopy.* Surf. Sci. Rep., 1999. **34**(1–3): p. 1-104.

38. Khatiwada, D. and S.K. Lamichhane, *A Brief overview of AFM force distance spectroscopy*. Himalayan Physics, 2011. **2**(2): p. 80-83.
39. Grierson, D., E. Flater, and R. Carpick, *Accounting for the JKR–DMT transition in adhesion and friction measurements with atomic force microscopy*. J. Adhes. Sci. Technol., 2005. **19**(3-5): p. 291-311.
40. Johnson, K.L., *Contact Mechanics*. 1985: Cambridge University Press.
41. Adams, G., *Contact modeling — forces.* Tribol. Int., 2000. **33**(5-6): p. 431-442.
42. Ricardo Garcia and E.T. Herruzo, *The emergence of multifrequency force microscopy.* Nat. Nanotechnol., 2012. **7**: p. 217-226.
43. Raman, A., Trigueros, S, Cartagena, A, Stevenson, APZ, Susilo, M, Nauman, E, Contera, S Antoranz, *Mapping nanomechanical properties of live cells using multi-harmonic atomic force microscopy.* Nat. Nanotechnol., 2011. **6**(12): p. 809-814.
44. *Measure Both Elastic and Viscous Properties with AFM*
45. Ebeling, D. and S.D. Solares, *Bimodal atomic force microscopy driving the higher eigenmode in frequency-modulation mode: Implementation, advantages, disadvantages and comparison to the open-loop case.* Beilstein J. Nanotechnol., 2013. **4**(1): p. 198-207.
46. Cronin-Golomb, M. and O. Sahin, *High-resolution nanomechanical analysis of suspended electrospun silk fibers with the torsional harmonic atomic force microscope.* Beilstein J. Nanotechnol., 2013. **4**(1): p. 243-248.
47. Dong, M., S. Husale, and O. Sahin, *Determination of protein structural flexibility by microsecond force spectroscopy.* Nat. Mater., 2009. **4**(8): p. 514-517.
48. A. Gannepalli, D.G.Y., A. H. Tsou, R. Proksch, *Mapping nanoscale elasticity and dissipation using dual frequency contact resonance AFM.* Nanotechnology, 2011. **22**(35): p. 355705.
49. Jesse, S.N., M. P. Germinario, L. T. Kalinin, S. V., *Local thermomechanical characterization of phase transitions using band excitation atomic force acoustic microscopy with heated probe.* Appl. Phys. Lett., 2008. **93**(7): p. 073104.
50. Stephen, J., Sergei, V. Kalinin, Roger, Proksch, A. P. Baddorf, B. J. Rodriguez, *The band excitation method in scanning probe microscopy for rapid mapping of energy dissipation on the nanoscale.* Nanotechnology, 2007. **18**(43): p. 435503.
51. Kos, A.B. and D.C. Hurley, *Nanomechanical mapping with resonance tracking scanned probe microscope.* Measurement Science and Technology, 2008. **19**(1): p. 015504.
52. Brian J Rodriguez, C.C., Sergei V Kalinin, Roger Proksch, *Dual-frequency resonance-tracking atomic force microscopy.* Nanotechnology, 2007. **18**(47): p. 475504.
53. Rabe, U. and W. Arnold, *Acoustic microscopy by atomic force microscopy.* Appl. Phys. Lett., 1994. **64**(12): p. 1493-1495.
54. Kos, A.B., J.P. Killgore, and D.C. Hurley, *SPRITE: a modern approach to scanning probe contact resonance imaging.* Measurement Science and Technology, 2014. **25**(2): p. 025405.
55. Kazushi, Y. and N. Shizuka, *Ultrasonic Atomic Force Microscope with Overtone Excitation of Cantilever.* Japan. J. Appl. Phys., 1996. **35**(6S): p. 3787.
56. Dillon, E., K. Kjoller, and C. Prater, *Lorentz contact resonance imaging for atomic force microscopes: probing mechanical and thermal properties on the nanoscale.* Microscopy Today, 2013. **21**(06): p. 18-24.
57. Ferencz, R.S., J. Blümich, B. Herrmann, W., *AFM nanoindentation to determine Young's modulus for different EPDM elastomers.* Poly. Test., 2012. **31**(3): p. 425-432.
58. Meyer, E., Lüthi, R., Howald, L., Güntherodt, H. J., *Friction Force Microscopy*, in *Forces in Scanning Probe Methods*, H.J. Güntherodt, D. Anselmetti, and E. Meyer, Editors. 1995, Springer Netherlands. p. 285-306.
59. Radmacher, M., R.W. Tillmann, and H.E. Gaub, *Imaging viscoelasticity by force modulation with the atomic force microscope.* Biophys. J., 1993. **64**(3): p. 735-742.

60. Li, H.-Q., *Phase Imaging: Beyond Topography.*
61. Hurley, D.C., *Measuring Mechanical Properties on the Nanoscale with Contact Resonance Force Microscopy Methods*, in *Scanning Probe Microscopy of Functional Materials: Nanoscale Imaging and Spectroscopy*, S.V. Kalinin and A. Gruverman, Editors. 2010, Springer.
62. Bhushan Bharat, F.H., *Applied Scanning Probe Methods II*. NanoScience and Technology. 2006, Heidelberg: Springer.
63. Marinello, F., D. Passeri, and E. Savio, *Acoustic Scanning Probe Microscopy*. 2012: Springer Berlin Heidelberg.
64. Hurley, D. and J.A. Turner, *Measurement of Poisson's ratio with contact-resonance atomic force microscopy.* J. Appl. Phys., 2007. **102**(3): p. 033509-033509-8.
65. Kermani, M.R., M. Moallem, and R.V. Patel, *Applied Vibration Suppression Using Piezoelectric Materials*. 2008: Nova Science Publishers.
66. Win-Jin, C., *Sensitivity of vibration modes of atomic force microscope cantilevers in continuous surface contact.* Nanotechnology, 2002. **13**(4): p. 510.
67. Chang, W.-J., T.-H. Fang, and H.-M. Chou, *Effect of interactive damping on sensitivity of vibration modes of rectangular AFM cantilevers.* Phys. Lett. A, 2003. **312**(3–4): p. 158-165.
68. Joseph, A.T. and S.W. Joshua, *Sensitivity of flexural and torsional vibration modes of atomic force microscope cantilevers to surface stiffness variations.* Nanotechnology, 2001. **12**(3): p. 322.
69. Muraoka, M. *Vibrational dynamics of concentrated-mass cantilevers in atomic force acoustic microscopy: Presence of modes with selective enhancement of vertical or lateral tip motion*. in *International Conference on Nanoscience and Technology (ICN&T 2006)*. 2007.
70. F. Marinello, P.S., S. Carmignato, E. Savio, *Critical factors in quantitative Atomic Force Acoustic Microscopy.* CIRP J. Manuf. Sci. Technol., 2010. **3**(1): p. 49-54.
71. Arnold, W., *Acoustical Near-Field Imaging*. Advances in Acoustic Microscopy and High Resolution Imaging: From Principles to Applications, ed. R.G. Maev. 2013: Wiley-VCH Verlag GmbH & Co. .
72. Hurley, D.C., *Measuring Mechanical Properties on the Nanoscale with Contact Resonance Force Microscopy Methods*, in *Scanning Probe Microscopy of Functional Materials*, S.V. Kalinin, Gruverman, Alexei, Editor. 2011, Springer: Springer New York Dordrecht Heidelberg London. p. 100.
73. Kalyan Phani, M., A. Kumar, and T. Jayakumar, *Elasticity mapping of delta precipitate in alloy 625 using atomic force acoustic microscopy with a new approach to eliminate the influence of tip condition.* Phil. Mag. Lett., 2014. **94**(7): p. 395-403.
74. Stan, G. and W. Price, *Quantitative measurements of indentation moduli by atomic force acoustic microscopy using a dual reference method.* Rev. Sci. Instrum. , 2006. **77**(10): p. 103707.
75. Killgore, D.C.H.a.J.P., *Dynamic Contact AFM Methods for Nanomechanical Properties*, in *Scanning Probe Microscopy for Industrial Applications: Nanomechanical Characterization*, D.G. Yablon, Editor. 2013, Wiley: New Jersey. p. 141.
76. A. Striegler, N.K., S. Matys, B. Köhler, and M. Kopycinska-Müller *Nanoscale Characterization of Yeast Cells by Use of Atomic Force Acoustic Microscopy Technique* in *Scanning Probe Microscopy & Optical Tweezers in Life Sciences* 2010: Berlin.
77. Hu, S., C. Su, and W. Arnold, *Imaging of subsurface structures using atomic force acoustic microscopy at GHz frequencies.* J of Appl. Phys., 2011. **109**(8): p. 084324.
78. Rabe, U., K. Janser, and W. Arnold, *Vibrations of free and surface-coupled atomic force microscope cantilevers: Theory and experiment.* Rev. Sci. Instrum., 1996. **67**(9): p. 3281-3293.

79. Carpick, R.W., D. Ogletree, and M. Salmeron, *Lateral stiffness: a new nanomechanical measurement for the determination of shear strengths with friction force microscopy.* Appl. Phys. Lett., 1997. **70**(12): p. 1548-1550.
80. Kester, E., Rabe, U, Presmanes, L, Tailhades, Ph, Arnold, W, *Measurement of mechanical properties of nanoscaled ferrites using atomic force microscopy at ultrasonic frequencies.* Nanostrcut Matter, 1999. **12**(5): p. 779-782.
81. Kester, E., Rabe, U., Presmanes, L., Tailhades, Ph, Arnold, W., *Measurement of Young's modulus of nanocrystalline ferrites with spinel structures by atomic force acoustic microscopy.* J. Phys. Chem. Solids 2000. **61**(8): p. 1275-1284.
82. Rabe, U., Kopycinska, M., Hirsekorn, S., Arnold, W., *Evaluation of the contact resonance frequencies in atomic force microscopy as a method for surface characterisation (invited).* Ultrasonics, 2002. **40**(1–8): p. 49-54.
83. U. Rabe, M.K., S. Hirsekorn, J. Muñoz Saldaña, G. A. Schneider, W. Arnold, *High-resolution characterization of piezoelectric ceramics by ultrasonic scanning force microscopy techniques.* J. Phys. D: Appl. Phys., 2002. **35**(20): p. 2621.
84. Kopycinska, M., Ziebert, Carlos, Schmitt, Heinz, Rabe, Ute, Hirsekorn, Sigrun, Arnold, Walter, *Nanoscale imaging of elastic and piezoelectric properties of nanocrystalline lead calcium titanate.* Surf. Sci., 2003. **532**: p. 450-455.
85. Hurley, D.C., Shen, K., Jennett, N. M., Turner, J. A., *Atomic force acoustic microscopy methods to determine thin-film elastic properties.* J of Appl. Phys., 2003. **94**(4): p. 2347-2354.
86. Caron, A., Rabe, U., Reinstädtler, M., Turner, J. A.. Arnold, W., *Imaging using lateral bending modes of atomic force microscope cantilevers.* Appl. Phys. Lett., 2004. **85**(26): p. 6398-6400.
87. Hurley, D.C. and J.A. Turner, *Humidity effects on the determination of elastic properties by atomic force acoustic microscopy.* J of Appl. Phys., 2004. **95**(5): p. 2403-2407.
88. Hurley, D., Kopycinska-Müller, M, Kos, AB, Geiss, RH, *Nanoscale elastic-property measurements and mapping using atomic force acoustic microscopy methods.* Meas. Sci. Technol., 2005. **16**(11): p. 2167.
89. Hurley, D.C., Kopycinska-Müller, M. Kos, A. B, Geiss, R. H, *Quantitative Elastic-Property Measurements at the Nanoscale with Atomic Force Acoustic Microscopy.* Adv. Eng. Mater., 2005. **7**(8): p. 713-718.
90. Kassavetis, S.N., S. Logothetidis, and G.M. Matenoglou, *Near-surface mechanical properties and surface morphology of hydrogenated amorphous carbon thin films.* Surf. Coat. Technol. , 2006. **200**(22–23): p. 6400-6404.
91. Kopycinska-Müller, M., Geiss, R. H., Müller, J., Hurley, D. C., *Elastic-property measurements of ultrathin films using atomic force acoustic microscopy.* Nanotechnology, 2005. **16**(6): p. 703-709.
92. Passeri, D.R., M. Alippi, A. Bettucci, A. Manno, D. Serra, A. Filippo, E. Lucci, M. Davoli, I., *Atomic force acoustic microscopy characterization of nanostructured selenium–tin thin films.* Superlattices and Microstructures, 2008. **44**(4–5): p. 641-649.
93. Muraoka, M. and S. Komatsu, *Characterization of films with thickness less than 10 nm by sensitivity-enhanced atomic force acoustic microscopy.* Nanoscale Res. Lett., 2011. **6**: p. 1-6.
94. Kopycińska-Müller, M., *On the elastic properties of nanocrystalline materials and the determination of elastic properties on a nanoscale using the atomic force acoustic microscopy technique*, 2005, Universität des Saarlandes: Saarbrücken. p. 131.
95. Zheng, Y., Geer, Robert E., Dovidenko, Katharine, Kopycinska-Müller, Malgorzata, Hurley, Donna C., *Quantitative nanoscale modulus measurements and elastic imaging of SnO2 nanobelts.* Journal of Applied Physics, 2006. **100**(12): p. 124308.

96. Passeri, D.B., A. Germano, M. Rossi, M. Alippi, A. Sessa, V. Fiori, A. Tamburri, E. Terranova, M. L., *Local indentation modulus characterization of diamondlike carbon films by atomic force acoustic microscopy two contact resonance frequencies imaging technique.* Applied Physics Letters, 2006. **88**(12): p. 121910.
97. Preghenella, M., A. Pegoretti, and C. Migliaresi, *Atomic force acoustic microscopy analysis of epoxy–silica nanocomposites.* Polymer Testing, 2006. **25**(4): p. 443-451.
98. Stan, G., Krylyuk, S., Davydov, A. V., Vaudin, M., Bendersky, L. A., Cook, R. F., *Surface effects on the elastic modulus of Te nanowires.* Applied Physics Letters, 2008. **92**(24): p. 241908.
99. Stan, G., Ciobanu, C. V., Thayer, T. P., Wang, G. T., Creighton, J. R., Purushotham, K. P., Bendersky, L. A., Cook, R. F., *Elastic moduli of faceted aluminum nitride nanotubes measured by contact resonance atomic force microscopy.* Nanotechnology, 2009. **20**(3): p. 035706.
100. Shah, S.P., O. Balogun, and J.H. Kim, *Atomic Force Acoustic Microscopy to Measure Nanoscale Mechanical Properties of Cement Pastes.* Transportation Research Record: J. T.R.B, 2010. **2141**(-1): p. 102-108.
101. Mege, F., F. Volpi, and M. Verdier, *Mapping of elastic modulus at sub-micrometer scale with acoustic contact resonance AFM.* Microelectron. Eng., 2010. **87**(3): p. 416-420.
102. Hurley, D.C. and J.A. Turner, *Measurement of Poisson's ratio with contact-resonance atomic force microscopy.* Journal of Applied Physics, 2007. **102**(3): p. 033509.
103. Hurley, D.C., Kopycinska-Müller, M., Langlois, E. D., Kos, A. B., Barbosa, N., *Mapping substrate/film adhesion with contact-resonance-frequency atomic force microscopy.* Applied Physics Letters, 2006. **89**(2): p. 021911.
104. Passeri, D.B., A, Germano, M, Rossi, M, Alippi, A, Orlanducci, S, Terranova, M. L, Ciavarella, M, *Effect of tip geometry on local indentation modulus measurement via atomic force acoustic microscopy technique.* Rev. Sci. Instrum. , 2005. **76**(9): p. 093904.
105. Beltrán, F., Muñoz-Saldaña, J, Torres-Torres, D, Torres-Martínez, R, Schneider, GA, *Atomic force microscopy cantilever simulation by finite element methods for quantitative atomic force acoustic microscopy measurements.* J of Mater. Res., 2006. **21**(12): p. 3072-3079.
106. Beltrán, F.E., Scholz, T, Schneider, GA, Muñoz-Saldaña, J, Rabe, U, Arnold, W. *Finite-element simulation of cantilever vibrations in atomic force acoustic microscopy*. in *Journal of Physics: Conference Series*. 2007. IOP Publishing.
107. Su, W.-T., Li, Bin, Liu, Ding-Quan, Zhang, Feng-Shan, *Low frequency acoustic response of surface cracks by atom force acoustic microscopy.* Surface Review and Letters, 2009. **16**(03): p. 449-453.
108. He Cunfu, Z.G., Wu Bin, Wu Zaiqi, *Subsurface defect of the SiOx film imaged by atomic force acoustic microscopy.* Opt.Laser.Eng., 2010. **48**(11): p. 1108-1112.
109. Killgore, J.P., Kelly, Jennifer Y, Stafford, Christopher M, Fasolka, Michael J, Hurley, Donna C, *Quantitative subsurface contact resonance force microscopy of model polymer nanocomposites.* Nanotechnology, 2011. **22**(17): p. 175706.
110. Yamanaka, K., et al., *Resonance frequency and Q factor mapping by ultrasonic atomic force microscopy.* Appl. Phys. Lett., 2001. **78**(13): p. 1939-1941.
111. Yuya, P.A., D.C. Hurley, and J.A. Turner, *Relationship between Q-factor and sample damping for contact resonance atomic force microscope measurement of viscoelastic properties.* J. Appl. Phys., 2011. **109**(11): p. 113528.
112. Killgore, J., Yablon, DG, Tsou, AH, Gannepalli, A, Yuya, PA, Turner, JA, Proksch, R, Hurley, DC, *Viscoelastic property mapping with contact resonance force microscopy.* Langmuir, 2011. **27**(23): p. 13983-13987.
113. Killgore, J.P. and D.C. Hurley, *Pulsed contact resonance for atomic force microscopy nanomechanical measurements.* Appl. Phys. Lett., 2012. **100**(5): p. 053104.

114. Stan, G., S.W. King, and R.F. Cook, *Nanoscale mapping of contact stiffness and damping by contact resonance atomic force microscopy.* Nanotechnology, 2012. **23**(21): p. 215703.
115. Kobayashi, K., H. Yamada, and K. Matsushige, *Resonance tracking ultrasonic atomic force microscopy.* Surf. Interface Anal., 2002. **33**(2): p. 89-91.
116. Luo, Y., Büchsenschütz-Göbeler, Matthias, Arnold, Walter, Samwer, Konrad, *Local elasticity and mobility of twin boundaries in martensitic films studied by atomic force acoustic microscopy.* New J. Phys., 2014. **16**(1): p. 013034.
117. Stan, G. and S.D. Solares, *Frequency, amplitude, and phase measurements in contact resonance atomic force microscopies.* Beilstein Journal of Nanotechnology, 2014. **5**: p. 278-288.
118. Kopycinska-Müller, M., R.H. Geiss, and D.C. Hurley, *Contact mechanics and tip shape in AFM-based nanomechanical measurements.* Ultramicroscopy, 2006. **106**(6): p. 466-474.
119. Malgorzata Kopycinska-Müller, R.H.G., Paul Rice, and Donna C. Hurley *Influence of Tip Wear on Atomic Force Acoustic Microscopy Experiments*. in *Mater. Res. Soc. Symp. Proc.* . 2004. Materials Research Society.
120. Killgore, J.P., R.H. Geiss, and D.C. Hurley, *Continuous measurement of atomic force microscope tip wear by contact resonance force microscopy.* Small, 2011. **7**(8): p. 1018-22.
121. Eiselstein, H.L. and D.J. Tillack, *The invention and definition of alloy 625*, in *Superalloys 718, 625, 706 and Various Derivatives*, E.A. Loria, Editor. 1995, TMS-AIME: Warrendale (USA). p. 1-14.
122. Sundararaman, M., P. Mukhopadhyay, and S. Banerjee, *Precipitation of the δ-Ni3Nb phase in two nickel base superalloys.* Metall. Mater. Trans. A 1988. **19**(3): p. 453-465.
123. Pollock, T.M. and S. Tin, *Nickel-Based Superalloys for Advanced Turbine Engines: Chemistry, Microstructure and Properties.* J. Propul. Power, 2006. **22**(2): p. 361-374.
124. Palanichamy, P., Mathew, MD, Latha, S, Jayakumar, T, Rao, K Bhanu Sankara, Mannan, SL, Raj, Baldev, *Assessing microstructural changes in alloy 625 using ultrasonic waves and correlation with tensile properties.* Scr. Mater., 2001. **45**(9): p. 1025-1030.
125. Floreen, S., G.E. Fuchs, and W.J. Yang, *The metallurgy of alloy 625.* Superalloys, 1994. **718(625)**: p. 13-37.
126. Shankar, V., K. Bhanu Sankara Rao, and S.L. Mannan, *Microstructure and mechanical properties of Inconel 625 superalloy.* J. Nucl. Mater., 2001. **288**(2–3): p. 222-232.
127. Sundararaman, M.K., Lalit, Prasad, G. Eswara Mukhopadhyay, P. Banerjee, S., *Precipitation of an intermetallic phase with Pt2Mo-type structure in alloy 625.* Metall. Mater. Trans. A 1999. **30**(1): p. 41-52.
128. Chakravartty, J., J. Singh, and M. Sundararaman, *Microstructural and mechanical properties of service exposed Alloy 625 ammonia cracker tube removed after 100 000 h.* Mater. Sci. and Technol., 2012. **28**(6): p. 702-710.
129. Lavakumar, A., Singh, PK, Srivastava, S, Kori, S, Kumar, LA, *Gamma Prime Coarsening Behavior of Nickel Super Alloy Super Cast 247A after Prolonged Thermal Exposures.* J. Mech. Civ. Eng, 2013. **334**: p. 37-42.
130. Harris, K. and J.B. Wahl. *Improved Single Crystal Superalloys, CMSX-4®(SLS)[La+ Y] and CMSX-486®*. in *Superalloys 2004*. 2004. TMS, Warrendale, PA.
131. Lacaze, J. and A. Hazotte, *Directionally Solidified Materials: Nickel-base Superalloys for Gas Turbines.* Texture Microstruct, 1990. **13**(1): p. 1-14.
132. *Superalloys: A Primer and History*. Available from: http://www.tms.org/meetings/specialty/superalloys2000/superalloyshistory.html.
133. Lavakumar Avala, C.V.S.M., Prince Kr singh, Bhargav Chaitanya, Shiva Kumar, Rajib Chakravorty and Eswara Prasad Namburi, *Effect of Microstructure on The Ambient Tensile Deformation Behavior of Nickel Base Superalloy Supercast 247A*, in *International*

Conference on Mining, Mineral Processing and Metallurgical Engineering (ICMMME'2013) 2013: Johannesburg (South Africa).

134. Gouda, M.K., K. Nakamura, and M. A. H. Gepreel, *First-principles study on the effect of alloying elements on the elastic deformation response in β-titanium alloys.* J. Appl. Phys., 2015. **117**(21): p. 214905.
135. Kumar, A., Jayakumar, T, Raj, Baldev, Banerjee, D, *A new methodology for identification of β-transus temperature in α+ β and β titanium alloys using ultrasonic velocity measurement.* Phil. Mag., 2008. **88**(3): p. 327-338.
136. Mohammed, M.T., Z.A. Khan, and A.N. Siddiquee, *Beta Titanium Alloys: The Lowest Elastic Modulus for Biomedical Applications: A Review.* International Journal of Chemical, Nuclear, Materials and Metallurgical Engineering, 2014. **8**(8): p. 772-777.
137. Lütjering, G. and J.C. Williams, *Titanium*. Engineering Materials and Processes. 2013: Springer Berlin Heidelberg. 379.
138. Shi, R., *Variant Selection during Alpha Precipitation in Titanium Alloys A Simulation Study*, 2014, The Ohio State University.
139. Gerhard Welsch, Rodney Boyer, and E.W. Collings, *Materials Properties Handbook: Titanium Alloys*. 1993, U.S.A: ASM International. 1176.
140. Mohammed, M.T., Z.A. Khan, and A.N. Siddiquee, *Beta Titanium Alloys: The Lowest Elastic Modulus for Biomedical Applications: A Review.* International Journal of Chemical, Nuclear, Materials and Metallurgical Engineering **8**(8): p. 772-777.
141. Kumar, A., et al., *A new methodology for identification of β-transus temperature in α+ β and β titanium alloys using ultrasonic velocity measurement.* Philosophical Magazine, 2008. **88**(3): p. 327-338.
142. Donachie, M.J., *Titanium: a technical guide*. 2000: ASM International.
143. Homporova, P., et al. *Dynamic phase evolution in titanium alloy Ti-6Al-4V.* in *The 12th World Conference on Titanium, Beijing, China*. 2011.
144. Hrabe, N., Kircher, R., & Quinn, T. *Effects of processing on microstructure and mechanical properties of Ti–6Al–4V fabricated using electron beam melting (EBM): Orientation and location*. in *15th Solid Freeform Fabrication Symp*. 2004. Austin, TX, USA.
145. Froes, F. and H. Bomberger, *The beta titanium alloys.* JOM, 1985. **37**(7): p. 28-37.
146. Viswanath, A., Kumar, Anish, Jayakumar, T, Rao, B Purnachandra, *Ultrasonic Characterization of Microstructural Changes in Ti-10V-4.5 Fe-1.5 Al β-Titanium Alloy.* Metall. Mater. Trans. A, 2015. **46**(8): p. 3393-3405.
147. Tamirisakandala, S., R.B. Bhat, and B.V. Vedam, *Recent advances in the deformation processing of titanium alloys.* J. Mater. Eng. Perform., 2003. **12**(6): p. 661-673.
148. Bhattacharjee, A.G., P., Gogia, A. K., Bhargava, S., Kamat, S. V., *Room temperature plastic flow behaviour of Ti–6.8Mo–4.5Fe–1.5Al and Ti–10V–4.5Fe–1.5Al: Effect of grain size and strain rate.* Mat. Sci. Eng. A-Struct., 2007. **452–453**: p. 219-227.
149. Feng Bo Han, J.S.L., Hong Chao Kou, Bin Tang, Min Jie Lai, Hui Chang *Constitutive Modeling of Beta Titanium Alloy Ti-10V-4.5Fe-1.5Al during Hot Deformation Process* Adv. Mat. Res., 2012. **510**: p. 729-733.
150. Balasubrahmanyam, V.V. and Y.V.R.K. Prasad, *Deformation behaviour of beta titanium alloy Ti–10V–4.5Fe–1.5Al in hot upset forging.* Mat. Sci. Eng. A-Struct. , 2002. **336**: p. 150-158

151. Luo, J., Li, Miaoquan, Yu, Weixin, Li, Hong, *Effect of the strain on processing maps of titanium alloys in isothermal compression.* Mater. Sci. and Engg. A, 2009. **504**(1–2): p. 90-98.

152. Kumar, A., Jayakumar, T., Raj, Baldev, Ray, K. K., *Characterization of solutionizing behavior in VT14 titanium alloy using ultrasonic velocity and attenuation measurements.* Mater. Sci. and Engg. A, 2003. **360**(1–2): p. 58-64.
153. Marinello, F., Schiavuta, P., Vezzù, S., Patelli, A., Carmignato, S., Savio, E., *Atomic force acoustic microscopy for quantitative nanomechanical characterization.* Wear, 2011. **271**(3–4): p. 534-538.
154. Rosoff, M., *Nano-Surface Chemistry*. 2001: CRC Press.
155. Mitchell, R.J., *Polycrystalline Nickel-Based Superalloys: Processing, Performance, and Application*, in *Encyclopedia of Aerospace Engineering*, R.B.a.W. Shyy, Editor. 2010, John Wiley & Sons, Ltd.
156. Jena, A.K. and M.C. Chaturvedi, *The role of alloying elements in the design of nickel-base superalloys.* J of Mater. Sci., 1984. **19**(10): p. 3121-3139.
157. Kitaguchi, H., *Microstructure-Property Relationship in Advanced Ni-Based Superalloys, Metallurgy - Advances in Materials and Processes*, D.Y. Pardhi, Editor 2012.
158. Hagihara, K., T. Nakano, and Y. Umakoshi, *Effect of Rh and V Additions on Plastic Deformation Behaviour in Ni3Nb Single Crystals with D0a Structure.* Mater. Trans., 2002. **43**(9): p. 2267-2274.
159. Kumar, A., Shankar, Vani, Jayakumar, T, Rao, K Bhanu Sankara, Raj, Baldev, *Correlation of microstructure and mechanical properties with ultrasonic velocity in the Ni-based superalloy Inconel 625.* Phil. Mag. A, 2002. **82**(13): p. 2529-2545.
160. Muzyka, D.R., *The Superalloys*. Science and Technology of Materials, ed. C.T.a.H. Sims, W. C. 1972, New york: Wiley.
161. Avala, L., Bheema, Mamatha, Singh, Prince Kr, Rai, Rabindra Kr, Srivastava, Sanjay, *Measurement of Thermo Physical Properties of Nickel Based Superalloys.* International Journal on Mechanical Engineering and Robotics (IJMER), 2013. **1**: p. 2321-5747.
162. Avala, L., et al., *Measurement of Thermo Physical Properties of Nickel Based Superalloys.* International Journal on Mechanical Engineering and Robotics (IJMER), 2013. **1**(1): p. 2321-5747.
163. Lavakumar Avala, C.V.S.M., Prince Kr singh, Bhargav Chaitanya, Shiva Kumar, *Property Enrichment of Aged Nickel Base Superalloy Supercast 247A.* International Journal on Theoretical and Applied Research in Mechanical Engineering (IJTARME), 2013. **2**(4): p. 2319 -3182.
164. Liu, S.D.a.W., *First-principles study on the structural, mechanical and electronic properties of δ and γ″ phases in Inconel 718.* Computat. Mater. Sci., 2010. **49**: p. 414-418.
165. Cao, Y., Zhu, Jingchuan, Nong, Zhisheng, Yang, Xiawei, Liu, Yong, Lai, Zhonghong, *First-principles studies of the structural, elastic, electronic and thermal properties of Ni 3 Nb.* Comput. Mater. Sci., 2013. **77**: p. 208-213.
166. Pierson, H.O., *Handbook of Refractory Carbides & Nitrides: Properties, Characteristics, Processing and Apps*. Revised ed. 1996: William Andrew. 362.
167. Xie, J.Y.C., N. X. Teng, L. D. Seetharaman, S., *Atomistic study on the site preference and thermodynamic properties for Cr23−xFexC6.* Acta Mater., 2005. **53**(20): p. 5305-5312.
168. Li, Y., Gao, Yimin, Xiao, Bing, Min, Ting, Yang, Ying, Ma, Shengqiang, Yi, Dawei, *The electronic, mechanical properties and theoretical hardness of chromium carbides by first-principles calculations.* J. Alloy. Compd., 2011. **509**(17): p. 5242-5249.
169. Wang, C.X., Junqi, Hu, Xuehui, Chen, Dong, Sun, Haibin, Yu, Benhai, *Elastic and Thermodynamic properties of NiAl and Ni3Al from first-principle calculations.* Int. J. Mod. Phys. B, 2011. **25**(27): p. 3623-3631.
170. Fatmi, M., Ghebouli, MA. Ghebouli, B, Chihi, T, Boucetta, S, Heiba, ZK, *Study of structural, elastic, electronic, optical and thermal properties of Ni3Al.* Rom. J. Phys., 2011. **56**(7-8): p. 935-951.

171. Wang, W. and K. Lu, *Nanoindentation measurement of hardness and modulus anisotropy in Ni 3 Al single crystals.* J. Mater. Res., 2002. **17**(09): p. 2314-2320.
172. Jun, C.K. and P.T.B. Shaffer, *Elastic moduli of niobium carbide and tantalum carbide at high temperature.* J. Less Common Met., 1971. **23**(4): p. 367-373.
173. López-de-la-Torre, L., Winkler, Björn, Schreuer, Jürgen, Knorr, Karsten, Avalos-Borja, Miguel, *Elastic properties of tantalum carbide (TaC).* Solid State Commun., 2005. **134**(4): p. 245-250.
174. Bartlett, R.W. and C.W. Smith, *Elastic Constants of Tantalum Monocarbide, TaC0.90.* J of Appl. Phys., 1967. **38**(13): p. 5428-5429.
175. Opeka, M.M.T., Inna G. Wuchina, Eric J. Zaykoski, James A. Causey, Samuel J., *Mechanical, Thermal, and Oxidation Properties of Refractory Hafnium and zirconium Compounds.* J. Eur. Ceram. Soc., 1999. **19**(13–14): p. 2405-2414.
176. Guemmaz, M., Mosser, A, Ahujab, R, Johansson, B, *Elastic properties of sub-stoichiometric titanium carbides: comparison of FP-LMTO calculations and experimental results.* Solid State Commun., 1999. **110**(6): p. 299-303.
177. Kopycinska-Müller, M., Striegler, A, Schlegel, R, Kuzeyeva, N, Köhler, B, Wolter, K.J, *Dual resonance excitation system for the contact mode of atomic force microscopy.* Rev. Sci. Instrum., 2012. **83**(4): p. 043703.
178. Dong, X., Zhang, Xiaoli, Du, Kui, Zhou, Yizhou, Jin, Tao, Ye, Hengqiang, *Microstructure of Carbides at Grain Boundaries in Nickel Based Superalloys.* J. Mater. Sci. and Technol., 2012. **28**(11): p. 1031-1038.
179. Kolli, R.P., W.J. Joost, and S. Ankem, *Phase Stability and Stress-Induced Transformations in Beta Titanium Alloys.* JOM-J. Min. Met. Mat. S 2015. **67**(6): p. 1273-1280.
180. Ozaki, T., Matsumoto, Hiroaki, Watanabe, Sadao, Hanada, Shuji, *Beta Ti alloys with low Young's modulus.* Mater.T. Jim, 2004. **45**(8): p. 2776-2779.
181. Karre, R., M.K. Niranjan, and S.R. Dey, *First principles theoretical investigations of low Young's modulus beta Ti–Nb and Ti–Nb–Zr alloys compositions for biomedical applications.* Mater. Sci. and Engg. C, 2015. **50**: p. 52-58.
182. Raabe, D., Sander, B., Friák, M., Ma, D., Neugebauer, J., *Theory-guided bottom-up design of β-titanium alloys as biomaterials based on first principles calculations: Theory and experiments.* Acta Mater., 2007. **55**(13): p. 4475-4487.
183. Lee, D.-G., Lee, Sunghak, Lee, Yongtai, *Effect of precipitates on damping capacity and mechanical properties of Ti–6Al–4V alloy.* Mater. Sci. and Engg. A, 2008. **486**(1–2): p. 19-26.
184. Guo Z., S.N., Schillé J.P., Miodownik A.P, *Materials Properties for Process Simulation.* Mater. Sci. Eng. A., 2009. **499**: p. 7-13.
185. Saunders, N., Li, X., Miodownik, A.P., Schille J. P. . *An Integrated Approach to the Calculation of Materials Properties for Ti-Alloys*. in *10th World Conference on Titanium*. 2003. Hamburg, Germany.
186. A. Singh, A. Bhattacharjee, and A. Gogia, *Microstructure and texture of rolled and annealed β titanium alloy Ti–10V–4.5Fe–1.5Al.* Mater. Sci. Eng. A., 1999. **270**(2): p. 225-230.
187. Pederson, R., *Microstructure and Phase transformation of Ti-6Al-4V*, 2002, Lulea University of Technology.
188. Tilley, R.J.D., *Understanding Solids: The Science of Materials*. 2nd ed. 2013: Wiley: Hoboken, NJ, USA.